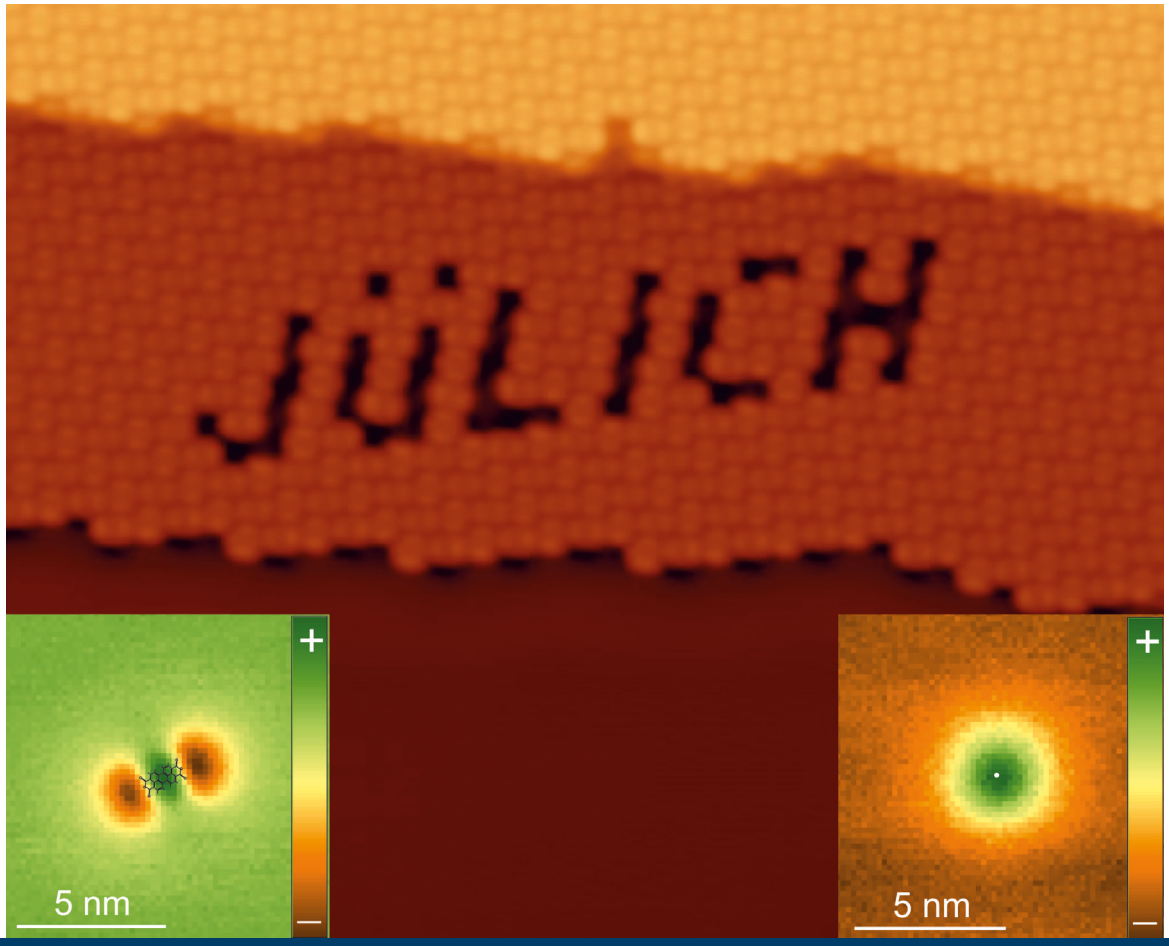

Creating and characterizing a single molecule device for quantitative surface science

Matthew Felix Blishen Green

Schlüsseltechnologien / Key Technologies
Band / Volume 181
ISBN 978-3-95806-352-5

Mitglied der Helmholtz-Gemeinschaft

JÜLICH
Forschungszentrum

Schriften des Forschungszentrums Jülich
Reihe Schlüsseltechnologien / Key Technologies Band / Volume 181

Forschungszentrum Jülich GmbH
Peter Grünberg Institut (PGI)
Functional Nanostructures at Surfaces (PGI-3)

Creating and characterizing a single molecule device for quantitative surface science

Matthew Felix Blishen Green

Schriften des Forschungszentrums Jülich
Reihe Schlüsseltechnologien / Key Technologies Band / Volume 181

ISSN 1866-1807 ISBN 978-3-95806-352-5

Bibliografische Information der Deutschen Nationalbibliothek.
Die Deutsche Nationalbibliothek verzeichnet diese Publikation in der
Deutschen Nationalbibliografie; detaillierte Bibliografische Daten
sind im Internet über http://dnb.d-nb.de abrufbar.

Herausgeber und Vertrieb:	Forschungszentrum Jülich GmbH Zentralbibliothek, Verlag 52425 Jülich Tel.: +49 2461 61-5368 Fax: +49 2461 61-6103 zb-publikation@fz-juelich.de www.fz-juelich.de/zb
Umschlaggestaltung:	Grafische Medien, Forschungszentrum Jülich GmbH
Druck:	Grafische Medien, Forschungszentrum Jülich GmbH
Copyright:	Forschungszentrum Jülich 2018

Schriften des Forschungszentrums Jülich
Reihe Schlüsseltechnologien / Key Technologies, Band / Volume 181

D 82 (Diss., RWTH Aachen University, 2018)

ISSN 1866-1807
ISBN 978-3-95806-352-5

Vollständig frei verfügbar über das Publikationsportal des Forschungszentrums Jülich (JuSER)
unter www.fz-juelich.de/zb/openaccess.

It is fair to state that we are not going to experiment with single particles any more than we will raise dinosaurs in the zoo.

—Erwin Schrödinger

Acknowledgments

There are many people without whom this dissertation would have been impossible to complete. For this reason I would like to thank

- Prof. Dr. Stefan Tautz for the opportunity to perform exciting research at PGI-3. When discussing the nature of our work, he once said 'the molecules will do what they have to do', and this rigour, respect but mostly love of his for physics and science helped me greatly during my time in Jülich. His enthusiasm for an enormous range of topics led to many lively lunchtime conversations, which however after the 23$^{\text{rd}}$ of June 2016 often revolved around one topic in particular.

- Dr. Ruslan Temirov for his excellent scientific supervision. His relentless search for the truth inspired me and he can often be found saying 'there are no miracles', a sentiment which gave me the impetus to look at many problems in a different way. I am very grateful for the countless discussions on science and beyond that we shared and the stimulating working environment he created.

- Dr. Christian Wagner for all his support but also the good times we enjoyed together in the lab. Without his advice and contributions this work would certainly have been less successful.

- Philipp Leinen and Dr. Taner Esat for our fruitful collaboration throughout the years. They were always around for interesting discussions, to help out in the lab or just to kick a football around the office.

- Dr. Norman Fournier for showing me the ropes, not only in the LT-STM/AFM lab but in Cologne-Ehrenfeld too.

- Alexander Grötsch for our collaboration with the motion tracking system and for speaking so much German with me in the lab; this certainly contributed to us not having to speak much English later on!

- All the members of PGI-3/ICS-7 who contributed to the very enjoyable working atmosphere in the institute.

- The many great friends I made while travelling to the research centre with the Rurtalbahn. No matter how delayed the RE1 was, the quality time spent with them provided me with a joyful start and end to the working day.

- My parents and step-parents Jo, Russ, Stuart and Isobel and my sisters Anna and Sasha for everything they do for me. Knowing that they are there for me makes life's challenges seem a little less insurmountable.

- Last but most importantly, my closest companion in life Sonja for her love, patience and support through all the highs and lows of the last several years. In fact, I couldn't imagine it without her.

Contents

Introduction

As the technological needs of today's global society continue to increase, the pressure to develop more powerful, more efficient and above all more compact electronic devices increases simultaneously. In 1965 Moore [1] exhibited a correlation between the number of transistors on an integrated circuit and the number of years following the invention of the integrated circuit in 1958 — the transistor count seemed to be roughly doubling every year. This prediction was modified to doubling every two years, which until several years ago had been fulfilled rather exactly. However the miniaturization limit of the current field effect transistor technology is gradually being reached [2], and a shift in the electronics paradigm will soon be required. There are several promising avenues currently at the focus of research for next-generation information technology; 2D materials, multiferroics and spin- and valleytronics form several examples [3–6]. A further example is the exciting field of molecular-scale electronics, where single molecules forming functional electronic devices is the ultimate goal [7, 8].

Aviram and Ratner's calculation of electronic transport through a single molecule [9] is often heralded as the beginning of modern molecular electronics. Their idea was that a single, polar molecule could act as a rectifier, which converts an alternating current into a direct current. However they were ahead of their time; the lack of appropriate technology prevented their ideas from being built upon in experiment. The advent of scanning tunnelling microscopy (STM) in the early 1980s [10] was the stimulus that molecular-scale electronics needed. Several seminal STM as well as mechanically controllable break junction experiments were the first to demonstrate transport through single molecules [11, 12]. In the years since then, a wide variety of functions have been demonstrated using single molecules, including transistor functionality [13–15] and rectification [16, 17], but also electromechanical amplification [18], switching [19, 20], memristance [21] and directional, mechanical motion [22].

The central challenges, besides economic considerations, that the integration of molecular electronic components into real world applications faces can be summarized into two general categories: control of electronic properties and control of geometrical properties. The understanding of electron transport through molecules is a key point where much research effort has been focused in the last decade [23]. However as Ratner [7] stated, with the estimated number of possible molecular structures at $\sim 10^{60}$ for small organic molecules, there is still much to be discovered in this area. As far as control over the geometry of a molecular system is concerned, bottom-up rather than top-down fabrication processes must be employed in order to allow for the tuning of of the properties of individual molecules. Here there are two main approaches: allowing molecules to arrange themselves into a pre-designed structure, known as self-assembly, or building a structure with the molecules as the 'building blocks'. Both approaches can in principle lead to extended structures defined at the molecular scale, and can even be employed in conjunction as will be displayed in this thesis. Seminal works, where single CO as well as C_{60} molecules were individually positioned on surfaces, demonstrated the feasibility of STM for molecular manipulation [24, 25]. However deterministic control over complex molecules at all stages of the manipulation procedure, vital for molecular-scale construction, has not yet been presented.

In this thesis, the atomically precise, mechanical manipulation of single molecules with the tip of a scanning probe microscope (SPM) is demonstrated. The prerequisites for controlled manipulation are twofold: firstly, the molecule must have a 'handle' by which it can be manipulated, for example a functional group. Secondly, the handle between the microscope tip and the molecule must be sufficiently stable throughout the manipulation, such that the molecule can be controllably taken from its initial state into a final state. The organic semiconductor perylene tetracarboxylic dianhydride (PTCDA), and its sister molecules naphthalene- and tetrylene tetracarboxylic dianhydride (N- and TTCDA), fulfils these two conditions. In this case the functional group is the carbonyl group, found at the four corners of the molecule, which forms a stable mechanical bond to the tip of the SPM. Particular favourable conditions are achieved by depositing the molecules onto an Ag(111) substrate, which is the substrate used for all experiments in this thesis. Chap. 2 demonstrates a single molecule manipulation procedure used to pattern a self-assembled PTCDA layer by

the controlled removal of single molecules. Molecules were individually contacted by the sharp microscope tip at a carboxylic oxygen atom, withdrawn from the layer and re-deposited to the surface in a highly reproducible fashion.

The degree of control exercised during the manipulation procedure was such that the intermediate stage was entirely stable and the molecule remained on the tip, in a well-defined metastable configuration, until deliberately returned to the surface. This made the development of a new microscopy method possible, based on the functionality of a single molecule. The method, dubbed *scanning quantum dot microscopy* (SQDM), uses single electron charging events of the tip-attached molecule, acting as a quantum dot (QD), to map the electrostatic potential present in the microscope junction. The SQDM sensor is therefore an example of a single molecule device. Since the functionality of the device is added to existing capabilities of the SPM, the microscope tip is described as being functionalized. A large advantage of tip functionalization is the spatial localization of the tip section contributing to the detected effect. In SQDM this results in a high spatial resolution in the measured electrostatic potential that is independent of the tip height. The electrostatic potentials, mapped using SQDM, of a single molecule and even a single atom are presented in Chap. 3.

The single electron charging events central to SQDM are a manifestation of the Coulomb blockade, an energy barrier stemming from interelectronic repulsion that prevents more than one electron hopping on or off the QD at any given instant. In order to develop SQDM as a measurement technique, the key parameters affecting this Coulomb blockade realization must be fully understood. An evaluation of the application of the orthodox theory of the Coulomb blockade [26] to our experimental data is presented in Chap. 4. This involves treating the microscope junction as a system of capacitors, from which the electrostatic force acting in the junction can be derived as a function of the charge state of the QD. However we show that the model is insufficient to explain our experimental data. Subsequently an intuitive, experimentally inspired model is developed to further our understanding of the data. Analyzing the energies of the QD's charge states, the key electronic properties of the QD can be expressed in terms of experimentally observable quantities. A comparison of the two approaches provides us with deeper insight into the application

of the models to such a system, especially with respect to QDs with small spatial dimensions.

Finally, a truly quantitative SQDM experiment is showcased in Chap. 5. It is shown that when measuring the surface potential of flat, extended structures, the measurement becomes independent of the structural properties of the tip. This allows for a highly quantitative measurement of the change in surface potential and therefore change in work function due to a surface structure. This is demonstrated for a layer of PTCDA molecules on Ag(111) where the change in work function due to PTCDA adsorption comes out at (145 ± 10) meV. We discuss the unprecedentedly high lateral resolution, a particular advantage of SQDM used for this purpose.

1

Theoretical background and experimental techniques

1.1. Introduction to scanning tunnelling microscopy

The cornerstone of the original scanning probe technique, scanning tunnelling microscopy (STM) [10], is the quantum tunnelling effect. Tunnelling refers to electrons passing through classically forbidden barriers. It is a result of the wave-like description of electrons and comes about when two conducting objects are brought within close proximity of each other. The one-dimensional potential barrier model can be used to intuitively understand the process, a schematic diagram of which is provided in Fig. 1.1. Electrons in the system must satisfy the one-dimensional time-independent Schrödinger equation (TISE):

$$\frac{-\hbar^2}{2m}\frac{\partial^2\Psi}{\partial z^2}(z) + U(z)\Psi(z) = E\Psi(z) \tag{1.1}$$

Ψ is the electronic wave function, which must be continuous. Since we are considering the TISE, Ψ is also referred to as a stationary state. $U(z)$ is a potential that a propagating electron experiences and E is the energy eigenvalue of the particular stationary state that satisfies the equation. If a negative voltage V_b is applied to the sample, electrons are biased to move from the sample to the tip. Eq. 1.1 can be solved for both in- and outside the vacuum barrier between the tip and sample:

$$z < 0 : \Psi_\mathrm{s}(z) = e^{ikz} + Ae^{-ikz} \quad \text{where} \quad k = \sqrt{\frac{2m}{\hbar^2}(E-U)} \tag{1.2a}$$

$$0 < z < z_\mathrm{tip} : \Psi_\mathrm{b}(z) = Be^{-\kappa z} + Ce^{\kappa z} \quad \text{where} \quad \kappa = \sqrt{\frac{2m}{\hbar^2}(U-E)} \tag{1.2b}$$

$$z > z_\mathrm{tip} : \Psi_\mathrm{t}(z) = De^{ikz} \tag{1.2c}$$

Eq. 1.2a shows that the solution when $E > U$ corresponds to freely propagating electrons, travelling in both directions since a certain proportion are reflected from the potential barrier. By demanding continuity at the edges of the potential barrier, Eqs. 1.2(a–c) can be solved for the four unknowns A, B, C, D and the reflection and transmission coefficients can be determined. The coefficient of transmission T depends on the barrier height and width, and if $\kappa z_\mathrm{tip} \gg 1$, then

$$T = \frac{16k^2\kappa^2}{\left(k^2+\kappa^2\right)^2}e^{-2\kappa z_\mathrm{tip}} \tag{1.3}$$

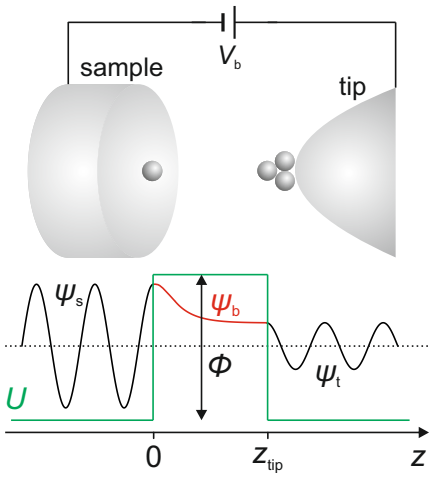

Figure 1.1: Schematic diagram of the quantum tunnelling effect. The Schrödinger equation solution in the electrodes is a plane wave; inside the potential barrier the electron wave function decays exponentially.

We therefore see that the probability of an electron tunnelling through the barrier decreases exponentially with the width of the barrier. An important result for the practical application of STM however is the size of the barrier decay constant κ. The barrier height $U - E$ is related to the work functions of the electrodes. If the two work functions are the same, i.e. $\phi_s = \phi_t = \phi$, then $\kappa = \sqrt{2m\phi/\hbar^2}$. The work function of a metal is typically $\sim$5 eV, which corresponds to $\kappa \simeq 1$ Å^{-1}. This means that per ångström of electrode separation, the probability of an electron tunnelling reduces by approximately one order of magnitude. This result is why the spatial resolution of STM can be so high, and also implies that in fact only the final atom of the tip contributes to the tunnelling current.

Bardeen [27] realized that Fermi's golden rule, the probability of an electron in one quantum state scattering into another, was key to the problem of quantum tunnelling. The tunnelling current within his formalism can be written as such, summing over all initial and final states:

$$I = \frac{4\pi e}{\hbar} \sum_{i,f} f(E_i)[1 - f(E_f + eV_b)]|M_{fi}|^2 \delta(E_i - E_f) \tag{1.4}$$

$f(E)$ is the Fermi-Dirac distribution for fermions, evaluated at both the initial and final state energies. $\delta(E_i - E_f)$ is a delta function of the final state energy E_f for each initial state energy E_i. The sum of delta functions represents the density of states (DOS) at E_f for each E_i. $|M_{fi}|^2$ is the tunnelling matrix element between initial and final states, representing the wave function overlap between tip and sample states with respect to tunnelling. Bardeen showed this could be written as

$$M_{fi} = \frac{\hbar^2}{2m} \int_S (\Psi_i^* \nabla \Psi_f - \Psi_f \nabla \Psi_i^*) \cdot d\mathbf{S} \tag{1.5}$$

The term in brackets is the current density operator, and the integral is performed over an arbitrary surface which lies entirely inside the barrier region. Eq. 1.4 can be expressed in a more intuitive manner by including a low-temperature approximation: in this case the Fermi-Dirac functions in Eq. 1.4 become step functions and the current can be expressed directly in terms of the densities of states in tip and sample, $\rho_{t,s}$:

$$I = \frac{4\pi e}{\hbar} \int_0^{eV_\mathrm{b}} \rho_\mathrm{t}(E' - eV_\mathrm{b}) \rho_\mathrm{s}(E') |M(E')|^2 dE' \tag{1.6}$$

The matrix element is now a function of energy instead of wave function. Note that since the Fermi-Dirac distributions are now step functions, we only integrate over the window of the applied bias voltage. Here it is explicitly seen how the tunnelling current depends on the DOS of tip and sample, plus the energy-dependent matrix element. Eq. 1.6 in fact encapsulates the most important principle of STM: the tunnelling current is a combination of topographic information, since the matrix element modulus decreases exponentially with tip-sample distance, and electronic information, since it is proportional to the DOS of tip and sample. While it is possible to use Eq. 1.6 to calculate the tunnelling current, the detailed electronic structure of the tip is however unknown. Tersoff and Hamann [28] developed on the Bardeen theory and modelled the tip as a single point, localized at a position $\mathbf{r}_t$. By carrying out this approximation at low temperature and low voltage, they showed that the tunnelling matrix element is proportional to the value of the sample wave function Ψ_s at the position of the tip $\mathbf{r}_t$. In other words, the square of the matrix element is equal to the probability of a sample electron being at the position of the tip. From this they constructed a new expression for the tunnelling current:

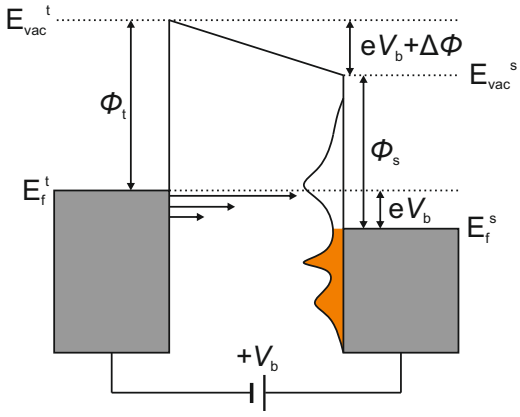

Figure 1.2: Energy diagram of the tunnelling junction. If a positive bias voltage is applied to the sample, the Fermi level or electrochemical potential of the sample is lowered with respect to the tip, and tunnelling can occur from the tip to the sample. In this case, unoccupied electronic states of the sample contribute to the tunnelling current (see text). Note that the vacuum levels are shifted by $eV_\mathrm{b} + \Delta\phi$ with respect to each other, where $\Delta\phi = |\phi_\mathrm{t} - \phi\mathrm{s}|$ represents the contact potential difference between the tip and sample.

$$I = \frac{4\pi e}{\hbar} eV_\mathrm{b} \sum_n |\Psi_n(\mathbf{r}_t)|^2 \delta(E_n - E_\mathrm{F}) \tag{1.7}$$

The sum is in fact equal to the local density of states (LDOS) at the position of the tip. Tersoff and Hamann showed that this expression holds assuming that the tip exhibits spherical symmetry, which is true if for example the tip apex is a spherical s-orbital. At low bias voltage the current is thus proportional to the voltage, from which it follows that the differential conductance is a direct measure of the LDOS:

$$\frac{dI}{dV} \propto \rho_\mathrm{s}(E_\mathrm{F},\ \mathbf{r}_t) \tag{1.8}$$

Therefore by recording a spectrum of the differential conductance, the LDOS of the sample at the Fermi level E_F and position $\mathbf{r}_t$ of the tip can be probed. Fig. 1.2 displays the tunnel junction in a schematic energy diagram. When a positive bias voltage is applied to the sample, its Fermi level is lowered as the electronic potential energy is lowered. If tip and sample are close, this results in tunnelling from the

tip into unoccupied states of the sample (occupied states are highlighted in orange). The reason why the current and differential conductance are primarily sensitive to the LDOS at the Fermi level of the tip E_F is that the tunnelling probability for electrons with lower energies is exponentially higher according to Eq. 1.3, illustrated by the arrows in Fig. 1.2.

It is however nigh-on impossible to guarantee spherical tip symmetry in the experimental realization of STM. Chen [29] showed with his derivative rule what the effect of p- or d-wave tips would be, and was able to explain the extraordinary lateral contrast that had been observed in experiment [30, 31], which was beyond the limits of what the Tersoff-Hamann model predicted. In fact, determining the exact structure of the tip remains one of the main obstacles in scanning probe microscopies, since it often influences measurement in a profound and non-trivial way.

1.2. Introduction to atomic force microscopy

The idea for a microscope capable of detecting forces at the atomic level came soon after the advent of the STM, and in fact the first design concept of the atomic force microscope (AFM) used an STM to detect microscopic changes in the deflection of a cantilever due to tip-sample forces [32]. The ubiquitous presence of tip-sample forces forms the key advantage of AFM over STM: its ability to characterize not only electrically conducting samples such as metals and semiconductors but also insulators, in solid or liquid phases. The force acting between tip and sample has several contributions at several different length scales. The long range force acting between tip and sample consists of the electrostatic as well as the dispersion or van der Waals interactions, which are both attractive. The electrostatic force is due to the surface charges on the two electrodes and has a simple form:

$$F_{\mathrm{el}} = -\frac{1}{2}\frac{\partial C}{\partial z}V_{\mathrm{b}}^2 \tag{1.9}$$

where C is the capacitance of the macroscopic tip-sample junction. The exact form of $\frac{\partial C}{\partial z}$ therefore depends on the junction geometry. If the tip and sample can be modelled as infinite parallel planes, then $F_{\mathrm{el}} \propto z_{\mathrm{tip}}^{-2}$ (see the definition of z_{tip} in Fig. 1.1). The van der Waals interaction between a sphere and an infinite plane, a relatively

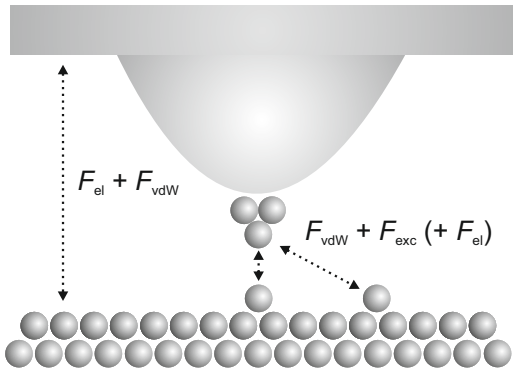

Figure 1.3: Forces acting in the scanning probe microscope junction.

good approximation to the AFM junction geometry, was shown by Hamaker [33] to be

$$F_{\mathrm{vdW}} = -\frac{AR}{6z_{\mathrm{tip}}^2} \tag{1.10}$$

R is the radius of the sphere, z_{tip} is the distance between the edge of the sphere and the plane and A is the Hamaker constant, which depends on the density of the materials and the atomic pair-potentials between them. F_{el} and F_{vdW} will therefore have similar distance dependences and typically are of similar sizes, in the nN range [34]. The exact geometry and tip-sample distance define which contribution dominates.

The long range forces most often make up the background of an AFM measurement, while the medium to short range forces are of greater interest. The dispersion or van der Waals interaction between two neutral atoms is proportional to the inverse of the sixth power of the distance between them, i.e. $E_{\mathrm{vdW}} \propto r^{-6}$ and therefore $F_{\mathrm{vdW}} \propto r^{-7}$. At very short range, this attractive force competes with the repulsive force based on the Pauli exclusion principle, which states that fermions are forbidden from occupying the same quantum state. Often termed Pauli repulsion, this apparent force comes about when the electronic wave function overlap between atoms becomes high at separations of a few ångströms. The combination of these two contributions is often summarized in a single interatomic potential, the most simple and frequently used variety of which is the Lennard-Jones potential:

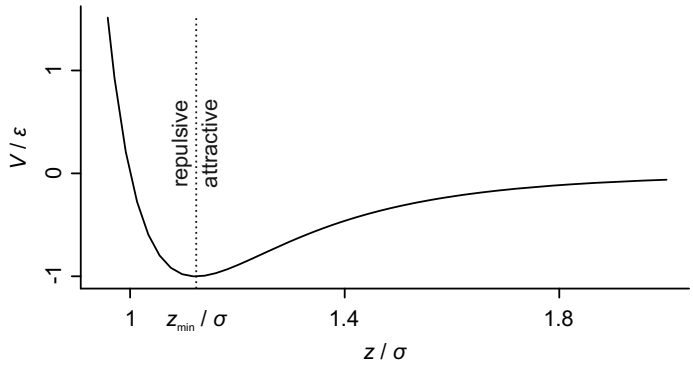

Figure 1.4: The interatomic Lennard-Jones potential, highlighting the transition from the attractive to the repulsive force regime.

$$V_{\text{L-J}} = 4\epsilon \left[\left(\frac{\sigma}{z} \right)^{12} - \left(\frac{\sigma}{z} \right)^{6} \right] \tag{1.11}$$

ϵ is equal to the potential minimum and σ refers to the z value at the minimum. The power of twelve in the repulsive contribution is empirically derived. Eq. 1.11 is plotted in Fig. 1.4, where the crossover between attractive and repulsive force regimes is highlighted. Since the overall force at this length scale changes dramatically with distance, it is often the regime where the desired experimental information is drawn from. However when the objects in question possess permanent electric charge, the longer range Coulomb interaction between them can also form the quantity of interest.

Three different operating regimes of AFM can be distinguished. In *contact mode*, or static deflection mode, the deflection of the AFM cantilever is detected as it is scanned across a surface while in the repulsive force regime [32]. The deflection itself can be used as the output signal, however small changes in height can lead to the cantilever tip 'snapping out' of contact, or undesirably large forces being applied to the sample. For this reason a feedback loop is usually utilized to maintain the deflection at a constant value. To get around the problem of high forces damaging the sample, *tapping mode* was created, whereby a cantilever is driven to oscillate at its resonant frequency, at an amplitude of several to hundreds of nanometres, while the sample is scanned [35]. Over the large oscillation cycle the entire force curve is

sampled, from weakly attractive to strongly repulsive. For this reason the cantilever is said to 'tap' the sample. The third imaging mode, which can achieve the highest lateral resolution, is the *non-contact mode*. In non-contact mode the AFM sensor oscillates at its resonant frequency, at a distance range from several nanometres above the surface, with soft (low stiffness) sensors, to several ångströms above the surface, where very stiff sensors must be employed to stop the tip from snapping into contact and the resonance being interrupted. Here the force is no longer the output signal, rather the resonant frequency of the sensor, which is related to the stiffness i.e. the force gradient of the junction. Two sub-modes can be employed: amplitude modulation and frequency modulation. In the amplitude modulation (AM) mode, the sensor is driven at a frequency slightly off resonance, and detected changes in the amplitude are used to reconstruct the shift in the sensor's resonant frequency [36]. Frequency modulation (FM) on the other hand directly tracks changes in the resonant frequency by demodulating the oscillation output [37], often with a phase locked loop [38]. An additional feedback loop is used in FM-AFM to keep the oscillation amplitude constant, from which the energy dissipation in the experiment can be reconstructed. FM-AFM has proved to be the ultimate AFM mode for sensitivity, and was thus the first of the measurement schemes to achieve atomic resolution [39].

1.3. Experimental details

1.3.1. Experimental setup

The scanning probe microscope used in this work is a combined non-contact atomic force microscope / scanning tunnelling microscope (nc-AFM/STM). The microscope head is based on the Besocke beetle-type design [40] and the system is produced by CreaTec Fischer & Co. GmbH. Throughout the work presented in this thesis the microscope was operated in ultrahigh vacuum conditions and at low temperatures. The system consists of a series of chambers with gate valves to separate them. Pressures of $\sim 10^{-7}$ mbar are achieved by initial evacuation with a scroll pump, followed by the addition of a turbomolecular pump. The system must also be baked such that water evaporates, after this pressures of $\sim 10^{-9}$ mbar can be achieved. The final base pressure of $1 * 10^{-10}$ mbar is reached with the use of two titanium

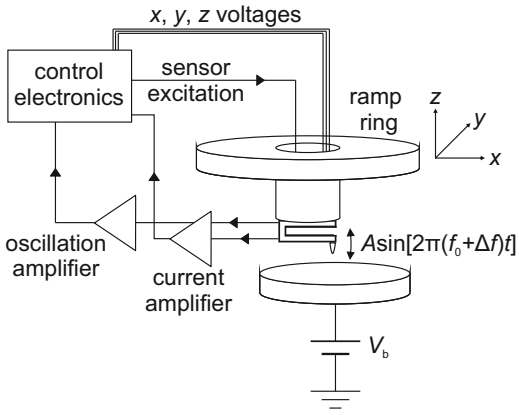

Figure 1.5: Schematic diagram of the SPM setup. The microscope tip is attached to a ramp ring, supported by three piezotubes (not shown). The ramp ring can be moved in three dimensions by extending the piezotubes, and coarse movement is possible through slip-stick motion of the ramp ring. Tunnelling current or the tuning fork's resonant frequency shift can be recorded, either separately or simultaneously.

sublimation pumps and two ion getter pumps. Low temperatures are achieved by surrounding the microscope head by two bath cryostats, separated by insulating shields. The outer cryostat is filled with liquid nitrogen (T = 77 K) and the inner with liquid helium (T = 4.2 K); in our setup the base temperature is 5 K. The cryopumping effect of the cryogens means that the base pressure in the measurement chamber is $< 3{*}10^{-11}$ mbar. Additionally, to isolate the microscope from mechanical disturbance, the entire system is suspended on four passive air dampers.

The microscope tip is connected to a ramp ring, supported by three piezotubes. Lateral motion in the xy-plane is achieved by lateral extension of the piezotubes. Motion in the z-direction is possible through vertical piezotube extension, and coarse motion (within a range of 1 mm) is facilitated by slip-stick rotation of the ramp ring. The tip is in fact attached to a fourth piezotube in the middle of the ramp ring that can be used for xyz-motion, however we utilize this piezotube to excite the AFM sensor. We use a quartz tuning fork of the qPlus type as a sensor [41]. In this design, one of the fork prongs is firmly connected to the tip holder and the second prong is free to oscillate.

Principle of STM operation

The STM uses tunnelling current to detect features on the surface. For this reason, a conducting tip and sample are required. In our setup the bias voltage is applied to the sample and the tip is grounded. The measured tunnelling current is directed from the tip to a transimpedance amplifier, the gain of which is set between 10^6 and 10^9, i.e. 1 nA $\equiv \{0.001, 0.01, 0.1, 1\}$ V. The signal is then recorded by the digital signal processor (DSP) and attributed to the scan pixel in question, before the tip is moved onto the next pixel of the image. There are two main scan modes available for STM measurement:

1. *Constant current mode.* Here the height of the tip is adjusted at each pixel to keep the tunnelling current constant. This is done by employing a PI feedback loop with a set point defined by a certain bias voltage and certain desired tunnelling current. This mode is useful for initial surface characterization: large surface protrusions or defects can cause the tip to crash into the surface, however with feedback that is fast enough this can be avoided. The image is composed of the tip height required to hold the current constant as a function of lateral tip position. However this does not correspond directly to the surface topography since the electronic structure also plays a role.

2. *Constant height mode.* This mode entails opening the current feedback loop and holding the tip height constant while recording the current as a function of lateral tip position. Due to its simplicity, constant height measurement allows for fast scanning, however the sample must be atomically flat or tip crashes will occur. Additionally, piezo creep and thermally induced drift mean that constant height scanning is more suitable for cryogenic temperatures.

Principle of AFM operation

AFM has in the last several years found a wider scope of application than STM since the detection of forces does not require the tip or sample to be conducting. Nevertheless, the detection scheme is somewhat more involved than that of STM. In the following we briefly introduce the key features of our non-contact, frequency modulated AFM setup. The qPlus tuning fork is excited piezoelectrically by broad-band pulses, and in the absence of interactions with the sample, oscillates at its

resonant frequency f_0. However when the tip begins to interact with the sample, the force acting on the tuning fork affects its oscillation and perturbs its resonant frequency. The new frequency of oscillation can be written as $f_{\text{res}} = f_0 + \Delta f$, where Δf is the frequency shift due to tip-sample interaction. Giessibl [42] described how tip-sample stiffness and force can be reconstructed from this frequency shift, which we will utilize in Chap. 4.

The deflection signal of the qPlus is also read out piezoelectrically, and the signal is internally amplified before being input into the phase-locked loop (PLL). The basic functionality of the PLL is as follows: its locks the phase of a reference oscillation, with a specific phase and frequency, to that of the experimental oscillation. When the frequency of the input signal changes, its phase diverges from that of the reference signal. By adjusting the frequency of the reference signal in order to match the phases, the PLL tracks the change in resonant frequency when tip-sample interactions are present [43]. In addition, a PI controller is utilized to maintain a constant oscillation amplitude. If dissipative processes have taken place during the oscillation cycle of the tuning fork (e.g. vibrational excitations of a surface structure), then the energy stored in the tuning fork reduces and the excitation amplitude must be temporarily increased to maintain the set point amplitude. The energy that is lost is recorded and referred to as the energy dissipation.

Similar to STM, there are again two main imaging modes within nc-AFM:

1. *Constant frequency shift mode.* A feedback loop is employed to keep the resonant frequency shift of the tuning fork constant during imaging. As the force-distance relationship at an atomic level is non-monotonic (see Fig. 1.4), the chance of a tip crash in this mode is high. Since the complexity of the PLL tends to limit the scan speed, an additional feedback loop for frequency shift means that scanning is typically rather slow.

2. *Constant height mode.* The feedback loop is opened and the tip-sample distance is kept constant while the frequency shift is recorded. Due to the aforementioned drawbacks of constant frequency shift scanning, constant height mode is the more popular of the two.

A further frequently used function in AFM is approach curve spectroscopy: the distance between the tip and the sample is varied while the frequency shift is moni-

Substance	T_{evap} (K)	t_{dep} (s)	T_{crys} (K)	T_{ann} (K)
NTCDA	450	60–120	300	400
PTCDA†	570	120–240	300	470
PTCDA‡	570	30–60	100	230
TTCDA	670	180–300	300	470
NaCl	610	10–30	300	400

Table 1.1: Parameters for molecular deposition. Annealing took place over 60–120 seconds. †Extended layers. ‡Small islands.

tored. In this way the force and interaction energy between tip and sample can be reconstructed.

1.3.2. Sample and tip preparation

The preparation of the Ag(111) crystal used in this thesis was carried out by cycles of sputtering and annealing, which took place in the preparation chamber, separated from the main measurement chamber. Depending on the cleanliness of the crystal, the following procedure was carried out 1–4 times: 15 minutes of Ar^{+} ion bombardment at 0.8 keV to remove layers of material from the surface, and 15 minutes of annealing to 800 K to create atomically flat terraces.

The deposition of molecules onto the crystal is summarized in Tab. 1.1. The important parameters are the evaporation temperature T_{evap}, the deposition time t_{dep}, the crystal temperature during deposition T_{crys} and the annealing temperature T_{ann}. Except for PTCDA, each other substance was evaporated from a crucible mounted on a sample holder, direct from the sample storage rack within the preparation chamber. PTCDA was evaporated from a homebuilt Knudsen cell. Annealing the crystal was necessary either to order the molecules or to remove unwanted surface adsorbates. In the case of sodium chloride, instead of wetting layers, three-dimensional ionic crystals are formed upon annealing, therefore the annealing temperature plays a crucial role.

The microscope tips used in this thesis were 15 µm-thick PtIr wires, glued onto qPlus tuning forks by CreaTec. The tips were cut and sharpened by focused ion

beam (FIB) milling with the help of D. Park and J. Mayer from RWTH Aachen University. Once cut, the resonant frequencies of the sensors used in this work were between 30.3 kHz and 31.8 kHz, with Q-factors between 20000 and 120000. The tips were not otherwise treated before being transferred into the microscope. To prepare the tip in experiment, a combination of voltage pulses and gentle dips into the metal surface was used. For large, structural changes on the mesoscopic scale, voltage pulses up to 10 V and dips of up to several tens of nanometres were carried out. The tip was deemed to be stable once pulses of ~ 6 V at a height of ~ 1 nm no longer changed the structure of the tip, signalled by abrupt jumps in the current-voltage trace. To sharpen the tip on the atomic level while simultaneously covering it with silver, dips of up to a nanometre into the surface were employed. The sharpness of the tip was judged in two ways: the sharpness of the features in an STM image and the resonant frequency shift at ~ 1 nm above the surface. The STM image quality is self-explanatory. In order to reliably perform the single molecule manipulation experiments to be discussed in this thesis, it was observed that a negative frequency shift of $< |5|$ Hz was required. This corresponds to a tip that is sharp on the mesoscopic scale.

2

Patterning a hydrogen-bonded molecular monolayer with a hand-controlled scanning probe microscope

Introduction

With the advent of the SPM in the early 1980s, it became clear that the precise manipulation of surface objects was something that the SPM would be well suited to. In the early 1990s, the first seminal works exhibited the arrangement of single atoms and small single molecules on surfaces using the tip of the microscope [44–46]. This attracted worldwide attention to the technique and since then atomic manipulation has become a standard procedure: most SPM groups have written their institute's name or logo in atoms at some point and many fascinating experiments have been presented [47–51]. Vertical manipulation, i.e. the transfer of an atom or molecule to the tip and back to the surface, as well as lateral manipulation, the lateral shifting of the particles, are both well-developed. However the manipulation process is in these cases essentially a two-stage operation. The initial state is the atom or molecule at a certain surface adsorption site and the final state is either at a certain tip adsorption site or another surface site, with no control over the intermediate state. This manipulation scheme has proved successful for point-like particles without internal, spatial degrees of freedom, however it is clear that with a more complex object, the probability of controlling each of its degrees of freedom during such a manipulation process is minimal.

In this chapter a method for atomically precise single molecule manipulation is presented, with which complex molecules can be controllably and reversibly manipulated between various geometric configurations. A commercial three-dimensional motion tracking device is combined with the standard SPM electronics, such that the tracked coordinates of an object in the lab are translated in real time to movements of the SPM tip. This apparatus is applied to the problem of patterning a PTCDA monolayer by removing molecules, where the molecules are tightly bound by their mutual hydrogen bonds. The overall intermolecular potential is a complex function of many contributions, including van der Waals interactions. There exists a path, or trajectory, along which the intermolecular forces are minimized, however the computation of this path is prohibitively costly, especially since the exact tip structure is unknown. For this reason the motion tracking approach is taken, where custom trajectories can be dynamically tested and selectively varied. This trial-and-error approach led to the successful manipulation of 47 PTCDA molecules from a monolayer, whereby the word 'JÜLICH' was patterned into the monolayer. We be-

lieve that this transferable method could help significantly on the way to functional molecular design, as a learning procedure as well as a training set for an automated process.

2.1. Patterning a hydrogen-bonded molecular monolayer with a hand-controlled scanning probe microscope

The journal article in this section was published in the Beilstein Journal of Nanotechnology [52]. The author contributions were as follows: M.F.B.G., C.W., R.T. and F.S.T. conceived the experiments. M.F.B.G. and P.L. performed the experiments. M.F.B.G. and A.G. installed the motion tracking system. M.F.B.G., T.E. and P.L. wrote the software to incorporate the motion tracking system. M.F.B.G. and R.T. analyzed the data. M.F.B.G., R.T. and F.S.T. wrote the paper and all authors discussed the manuscript throughout.

BEILSTEIN JOURNAL OF NANOTECHNOLOGY

Patterning a hydrogen-bonded molecular monolayer with a hand-controlled scanning probe microscope

Matthew F. B. Green[1,2], Taner Esat[1,2], Christian Wagner[1,2,3], Philipp Leinen[1,2], Alexander Grötsch[1,2,4], F. Stefan Tautz[1,2] and Ruslan Temirov[*1,2]

Full Research Paper

Open Access

Address:
[1]Peter Grünberg Institut (PGI-3), Forschungszentrum Jülich, 52425 Jülich, Germany, [2]Jülich Aachen Research Alliance (JARA)-Fundamentals of Future Information Technology, 52425 Jülich, Germany, [3]Leiden Institute of Physics, Universiteit Leiden, Niels Bohrweg 2, 2333 CA Leiden, The Netherlands and [4]Unit Human Factors, Ergonomics, Federal Institute for Occupational Safety and Health (BAuA), 44149 Dortmund, Germany

Email:
Ruslan Temirov[*] - r.temirov@fz-juelich.de

* Corresponding author

Keywords:
atomic force microscopy (AFM); scanning tunneling microscopy (STM); single-molecule manipulation; 3,4,9,10-perylene tetracarboxylic acid dianhydride (PTCDA)

Beilstein J. Nanotechnol. **2014,** *5,* 1926–1932.
doi:10.3762/bjnano.5.203

Received: 09 July 2014
Accepted: 10 October 2014
Published: 31 October 2014

Associate Editor: S. R. Cohen

Abstract

One of the paramount goals in nanotechnology is molecular-scale functional design, which includes arranging molecules into complex structures at will. The first steps towards this goal were made through the invention of the scanning probe microscope (SPM), which put single-atom and single-molecule manipulation into practice for the first time. Extending the controlled manipulation to larger molecules is expected to multiply the potential of engineered nanostructures. Here we report an enhancement of the SPM technique that makes the manipulation of large molecular adsorbates much more effective. By using a commercial motion tracking system, we couple the movements of an operator's hand to the sub-angstrom precise positioning of an SPM tip. Literally moving the tip by hand we write a nanoscale structure in a monolayer of large molecules, thereby showing that our method allows for the successful execution of complex manipulation protocols even when the potential energy surface that governs the interaction behaviour of the manipulated nanoscale object(s) is largely unknown.

Introduction

The scanning probe microscope (SPM) is an excellent tool for the manipulation of atoms and molecules on surfaces due to its high spatial imaging resolution and atomic-scale precision [1-7]. Today, controlled SPM manipulation of individual atoms and small molecules is a routine operation [6-8]. It has been recognised that the outcome of such manipulations is fully

defined by the microscopic interactions between the manipulated atom or molecule, the surface and the tip [5].

If the manipulated object is an individual atom or a small molecule its internal degrees of freedom can be neglected (as for a point-like particle) such that the state of the particle is fully described by its three spatial coordinates. Since the position of the tip apex is also defined by a set of three coordinates, the full state space of an SPM junction that contains one point-like particle essentially has at least six independent dimensions [9]. Therefore in order to perform a successful SPM manipulation one ideally needs to know the junction potential function defined over the whole 6-D state space. Because most of the detailed studies of SPM manipulation have been performed on individual atoms or small molecules adsorbed on surfaces with a highly symmetric structure, their success can be explained to a large extent by the fact that the high symmetry of the surface considerably simplifies the potential of the junction in multifunctional state space [5,8]. At the same time it is clear that the realisation of more advanced nanoscale functions will eventually rely on highly controlled manipulations with molecular objects of larger size, possessing numerous internal degrees of freedom and adsorbed on surfaces with a more complex and thus less symmetric structure.

Unfortunately, the behaviour of large molecules on surfaces is generally not well understood. Despite the fact that studies of complex molecular adsorption are progressing quickly, even in the best-studied model cases a full and quantitatively precise picture of the molecular adsorption potential (even in the absence of the SPM tip) is not yet available. For systems that contain a larger number of molecules that may simultaneously interact with the surface, the SPM tip and each other, reconstruction of the potential does not seem realistic in the nearest future.

How can we nevertheless manipulate large molecules successfully, despite lacking full knowledge of their complex interaction potential? Generally, the manipulation act is defined as a trajectory that connects the initial and the final states of the junction in its multidimensional state space. In SPM such trajectories can only be executed by controlled changes of the spatial coordinates of the tip. The other degrees of freedom of the junction, namely the centre of mass and the internal degrees of freedom of the manipulated molecule, cannot be directly controlled; instead they relax spontaneously as the tip is moved along its 3-D trajectory. Their relaxations are always directed such that they minimize (locally) the total potential of the junction. For a manipulation to be "successful" the sequence of spontaneous relaxations of molecular degrees of freedom must steer the junction into the final state of the manipulation. If the potential of the system were known at each point of its state space, the identification of the desired tip trajectory would become a mathematical problem. In reality, since the potential is not known "successful" trajectories can only be determined with the help of an experiment in which the relevant regions of the potential landscape are explored in a "trial and error" fashion and the obtained information is finally used for learning. In future one could envision a computer-driven SPM that automatically learns successful manipulation protocols through performing specific experiments on single molecules and analysing their outcomes. Here we demonstrate the principal possibility of such learning by substituting a computer-driven system with a human operator controlling the position of the SPM tip with their hand. Our experiments directly show that the operator efficiently finds trajectories for the intentional manipulation of large organic adsorbates without prior knowledge of the potential to which the manipulated system is subjected.

Experimental

For the demonstration of our manipulation technique we chose one of the best-studied cases of the adsorption of complex organic molecules: the well-ordered interface formed by the archetypal organic semiconductor 3,4,9,10-perylene tetracarboxylic acid dianhydride (PTCDA) on a single-crystalline Ag(111) surface [10] (see Figure 1a). An Ag(111) single crystal was cleaned by repeated Ar-sputtering and annealing cycles. A small coverage of PTCDA molecules (less than 10% of a monolayer) was subsequently deposited from a custom-built Knudsen-cell onto the freshly prepared Ag(111) surface kept at room temperature. Immediately after deposition the sample was moved into the microscope and cooled to 5 K. Prior to the imaging and manipulation experiments the SPM tips were prepared by voltage pulses of 3–6 V (applied to the sample) and by crashing 10–30 Å deep into the clean Ag(111) surface whilst simultaneously applying a voltage of 0.1–1 V. The cleanness of the tip was validated by STM imaging of the former lowest unoccupied molecular orbital (LUMO) of PTCDA [10] and spectroscopy of the Ag(111) surface state. All PTCDA images shown were made with STM at $I = 0.1$ nA and with an applied bias voltage of $V = -0.34$ V that facilitates the intramolecular resolution corresponding to the LUMO. All of the reported experiments were performed in situ under ultra high vacuum conditions.

The adsorption mechanics of PTCDA on Ag(111) is well understood: a PTCDA molecule binds to the metal surface through an extended bond that involves charge transfer into its LUMO and also locally with its four carboxylic oxygen atoms [10,11] (marked by white circles in Figure 1a). The same atoms enable SPM manipulation with the molecule, since an individual

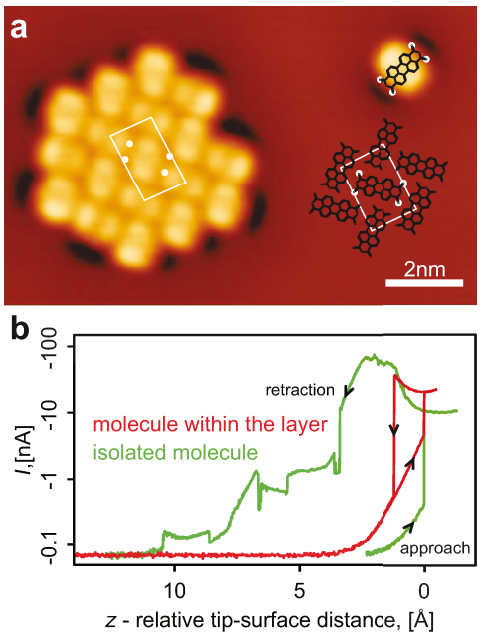

Figure 1: (a) 13 × 8 nm^2 STM image of a PTCDA island grown on an Ag(111) surface and of an isolated PTCDA molecule detached from it. The white rectangle marks the unit cell of the monolayer. The structure of the PTCDA/Ag(111) layer is displayed on the right. The positions of the carboxylic oxygen atoms of PTCDA are marked by white circles. All of the STM images were post-processed with WSxM software [14]. (b) $I(z)$ curves measured upon tip approach and subsequent retraction executed over one of the carboxylic oxygen atoms of PTCDA with the applied bias voltage of $V = -5$ mV. Black arrows superimposed on the red and green curves show the direction of the tip movement. The contact event is observed as a sharp increase of $I(z)$. The isolated PTCDA molecule can be pulled away from the surface simply by retracting the tip vertically (green curve). PTCDA molecules that reside inside monolayer islands resist pulling, which breaks their contact to the tip prematurely (red curve). The relative tip–surface distance scale (z) was aligned such that the contact point defined its zero value.

carboxylic oxygen atom can bind the molecule to the SPM tip [12]. For a molecule residing within a compactly ordered monolayer, the same carboxylic groups are involved in hydrogen-bonds with the C–H side groups of neighbouring PTCDA molecules [10,11]. These intermolecular interactions bind the molecules to each other, holding them tightly within the molecular islands [13].

An attempt to manipulate PTCDA thus faces a conspicuous practical problem: while an isolated molecule that has no neighbours can be contacted and lifted from the surface with the SPM tip in a straightforward manner, the interactions between the molecules foil most of the attempts to remove a molecule residing inside the compact molecular monolayer [15,16] (see Figure 1b). Although the nature of the forces that hold the layer together is qualitatively understood, due to the lack of quantitative information it is not clear a priori how to remove a molecule from the layer with the SPM tip; because of the prohibitively large state space it would also be impossible to calculate this with reasonable effort. As will be shown here, hand-controlled manipulation (HCM) using the SPM tip allows us to find a manipulation protocol that removes single PTCDA molecules from the molecular monolayer very reliably.

We performed the molecular manipulation with a commercially available SPM. Our instrument, the low-temperature combined non-contact atomic force/scanning tunnelling microscope (NC-AFM/STM) from CREATEC, allows for a stable and precise positioning of the tip, while simultaneously measuring the current flowing through the junction (I) and the frequency shift of the oscillating tip (Δf). Measuring Δf provides additional information about the microscopic junction structure [15,16]. For the AFM functionality we used a qPlus sensor [17] manufactured by CREATEC. The AFM/STM tip was made from a 0.3 mm long and 15 µm thick PtIr wire glued to the tuning fork of the qPlus sensor, and sharpened with a gallium focused ion beam (FIB). The resulting resonance frequency of the qPlus sensor was $f_0 = 30{,}300$ Hz with a quality factor of $Q \approx 70{,}000$. Contacting and manipulation were performed with the qPlus sensor oscillating with an amplitude of $A_0 \approx 0.2$–0.3 Å. Interactions in the junction were monitored by measuring the frequency shift $\Delta f(z) \approx -(f_0/2k_0)dF_z/dz$, where $k_0 = 1800$ N/m is the stiffness of the quartz tuning fork used.

The essence of our approach lies in the coupling of the sub-angstrom precise positioning of the tip of our instrument to the motion of the operator's hand [18]. This is achieved with the help of a commercial motion tracking system from VICON (see Figure 2). The VICON software was used to obtain Cartesian coordinates of a marker attached to the hand of the operator and feed them into a high precision power supply from STAHL ELECTRONICS that generated three voltages, v_x, v_y and v_z, which were added to the voltages u_x, u_y, u_z used by the scanning probe software to control the position of the SPM tip. The system was calibrated such that 5 cm of hand motion corresponded to 1 Å of tip movement, and calibration constants were chosen to be the same for x, y, and z directions. The tip manipulation speed did not exceed 0.2 Å/s. This limitation was imposed by the latency time of the communication channel between the tracking software and the power supply generating the voltages v_x, v_y, v_z (see Figure 2). The spatial uncertainty introduced by the motion tracking software was equal to 0.01 Å along each of the axes (x, y, z). The uncertainty introduced by the electrical noise in the low- and high-voltage amplifiers was about 0.01 Å along z and 0.05 Å along x and y directions. The

coupling latency time was 50 ms. The contacting and molecular manipulation was performed at V_b = −5 mV. In total 48 molecules were extracted from the monolayer. Each HCM was preceded by an attempt to lift the molecule by moving the tip straight up from the surface; only five molecules were removed in this manner.

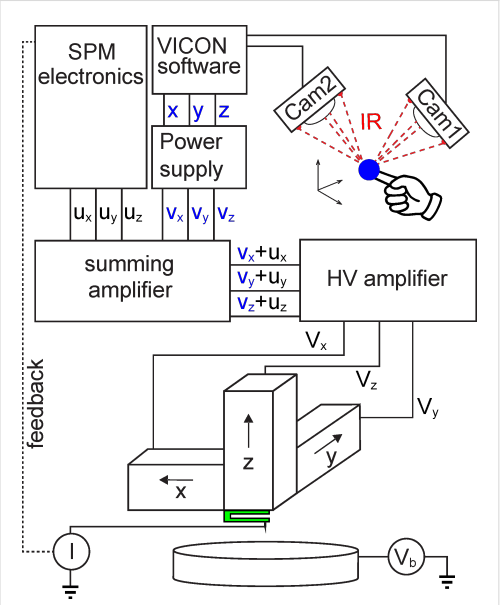

Figure 2: Scheme of the set-up for manual control of the SPM tip. Lamps mounted on the front of the two cameras emit infrared light that is reflected by a single marker fixed rigidly to the hand of the operator. The reflected light is captured by the cameras; with two cameras full three-dimensional triangulation is achieved. At the system output the real-time $x(t)$, $y(t)$, $z(t)$-coordinates of the marker are extracted. These coordinates are converted into a set of three voltages v_x, v_y, v_z that are further added to the u_x, u_y, u_z voltages of the SPM software used to control the scanning piezo-elements of the microscope. In this way when the feedback loop is closed the position of the SPM tip is controlled by the SPM software, but when the feedback loop is open the tip is controlled by the hand of the operator. During the manipulation $v_x + u_x$, $v_y + u_y$ and $v_z + u_z$ voltages are sampled at a frequency of 1 kHz.

Each individual HCM started by acquiring a constant current STM image of the molecule to be manipulated. The tip was then parked over the carboxylic oxygen atom of PTCDA that had been selected for contacting and the current feedback loop of the SPM software was opened. The contact to the molecule was established by approaching the tip vertically towards the surface; this approach was effected by downward movement of the hand of the operator. Over the course of HCM the current I flowing through the junction and the frequency shift Δf were displayed on the screen of an oscilloscope and served as feedback signals for the operator. Formation (loss) of the contact was monitored in real time by a sharp increase (decrease) of I (cf. Figure 1b) or a kink in Δf [15,16]. After establishing the contact between the tip and the molecule, the operator retracted the tip along an arbitrary three-dimensional trajectory. If the contact to the molecule was lost prematurely, the tip was moved back to the initial parking position by zeroing the v_x, v_y and v_z voltages and the manipulation was re-initiated. If contact was maintained up to retraction distances of 10–15 Å, the tip was moved, with the help of the SPM software, laterally at constant height to a clean silver surface area. There an attempt to re-deposit the molecule from the tip back to the surface was made. Re-deposition was performed by approaching the tip with the removed PTCDA molecule hanging on its apex towards the Ag(111) surface and applying a voltage pulse of 0.6–1 V. Afterwards the current feedback loop was closed and the manipulation area was scanned in constant current STM mode (a movie that was made of the scanned STM images can be found in the Supporting Information). If the state of the tip apex was changed during HCM it was reshaped by gentle dipping into the surface.

With this approach and without any prior experience it took about 40 minutes to remove the first molecule from the layer. Repeating the experiment, we observed that the average time necessary to remove one molecule decreased to 13 minutes after about 10 successful attempts. We stress here that this learning was based entirely on rather sparse information about the junction, namely the conductance at a fixed bias voltage and the frequency shift Δf related to the z-gradient of the vertical force [15,16].

Results and Discussion

Inspecting Figure 3a, which displays the 3-D trajectories that successfully extracted the PTCDA molecules from the layer, we note several interesting observations. First we see that all of the successful trajectories tend to “bunch” in a relatively narrow solid angle. The correct determination of that angle thus largely defines the success of the manipulation. Here the operator determines the required solid angle by using the fact that unsuccessful trajectories terminate prematurely with the tip-molecule bond rupture. As Figure 3b shows, many of the trajectories “survive” the first 3 Å of pulling, although the ones that are going to become successful start to concentrate in the upper right quadrant. As the tip moves further away from the surface many unsuccessful traces get terminated due to the premature breaking of the tip–molecule contact. Indeed Figure 3c shows that at a distance of 7 Å most of the successful trajectories lie within the solid angle Ω (cf. Figure 3c), the direction of which suggests that the molecule is peeled off the surface starting from the corner at which the contact to the tip was established [19].

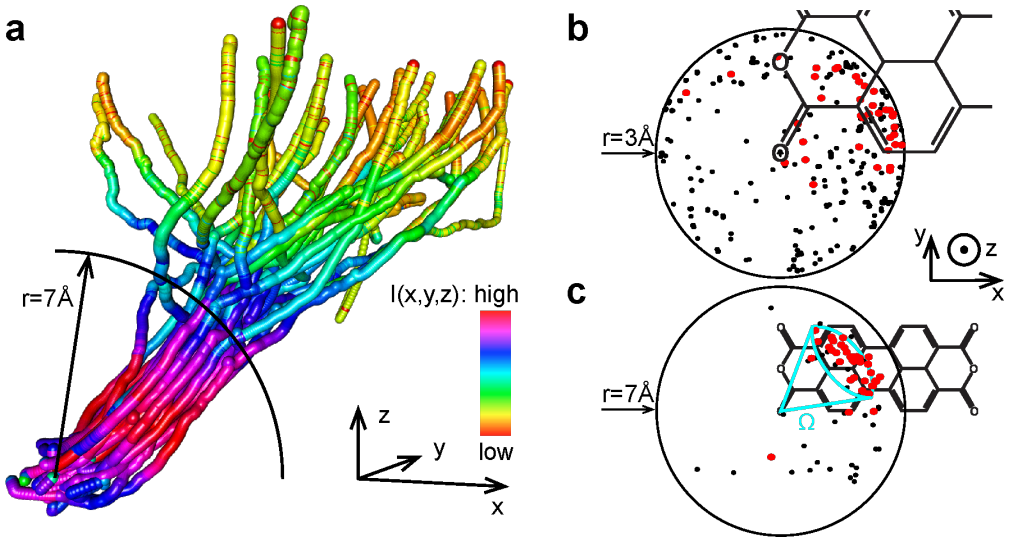

Figure 3: a) A perspective view on a set of 34 3-D manipulation trajectories that resulted in the removal of PTCDA molecules from the monolayer. In order to facilitate plotting, the density of recorded data was reduced by a factor of 100 to a sampling frequency of 10 Hz. Each point of the trajectory is plotted as a sphere with a radius of 0.2 Å, corresponding to the amplitude of the oscillations of the AFM/STM tip. The colour of the sphere reflects the value of $I(x, y, z)$ measured at the given point of the manipulation trajectory. The black circle shows the boundary of the sphere from Figure 3c. For a more detailed view of the displayed 3D trajectories download the 3D animation or the interactive 3D model from Supporting Information. b,c) Full statistics of manipulation trajectories (including unsuccessful ones) (top view). The circle marks the boundary of a sphere with the radius 3 Å (b) and 7 Å (c) the center of which was placed at the position of the carboxylic oxygen atom through which the molecule was contacted by the tip. Red (black) points mark locations where the successful (unsuccessful) trajectories penetrate the sphere. Bunching of the successful trajectories in a narrow solid angle is visible at larger tip–surface distances.

We remarked previously that the effectiveness of peeling stems from the fact that it promotes gradual (vs simultaneous) cleavage of the existing molecule–surface bonds [12,16]. In contrast to the case of an isolated molecule, when the molecule is peeled out of the compact layer the intermolecular bonds also need to be cleaved. Therefore extraction of the molecule from the layer needs a much more carefully chosen trajectory which "schedules" the cleavage of the molecule–surface bonds as well as the bonds between molecules in such a manner that the total force acting on the tip–molecule bond is kept under a critical threshold. The identification of such trajectories is performed here by the operator carrying out HCM and we find that the success of the peeling is largely defined by the direction along which the tip is moved for the first 7 Å.

Notably, after reaching a retraction distance of about 7 Å the trajectories shown in Figure 3a start to diverge from each other. This suggests that the majority of the bonds that hold the molecule within the monolayer have been cleaved by that point, thus reducing the importance of the shape of the trajectory substantially. Interestingly, the process of gradual bond cleavage is also reflected by the initial increase in the current $I(x, y, z)$ flowing through the junction (cf. the red sections of the successful trajectories in Figure 3a). This observation is in agreement with previously published data that relate the increase of conductance through the tip–PTCDA–Ag(111) junction with the effects of de-population and de-hybridization of the LUMO of PTCDA, which occur upon the gradual breaking of the PTCDA–Ag(111) bonds [12,20,21].

Finally, to illustrate the reliability of the HCM, we present a structure "stencilled" into PTCDA/Ag(111) by sequentially removing single molecules from the layer (Figure 4). Importantly, the images report the very first attempt, with no previous experience and without training. A movie, assembled from constant current STM images scanned after each removal step, can be downloaded as Supporting Information. It shows that 48 molecules were extracted from the layer in a sequence defined by the will of the operator. Remarkably, it was possible to re-deposit 40 of the removed molecules onto the clean Ag(111) surface nearby, showing that the molecules are not damaged during their extraction [22]. Therefore, as Figure 4

shows, manual manipulation can also be used to "correct" errors by filling a created vacancy with a molecule that has been extracted from a different location.

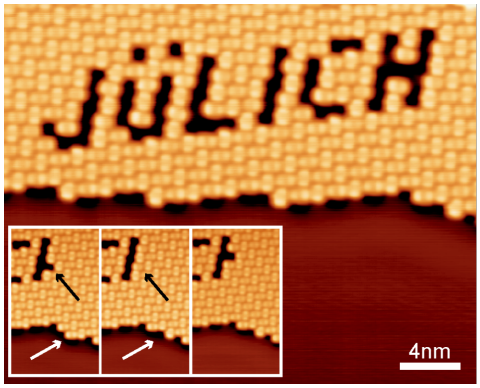

Figure 4: Constant current STM image of a structure consisting of 47 vacancies that were created by removing individual PTCDA molecules from the PTCDA/Ag(111) monolayer. The sequence of intermediate steps recorded during writing can be downloaded from the supplement. The three insets show the "repair" of a vacancy created by mistake. The black arrow marks the position of the error vacancy. The white arrow marks the position of the molecule at the edge of the molecular monolayer island that was used to fill the error vacancy. The molecule from the edge was removed by using the same manipulation protocol as for all other vacancies and was then placed into the error vacancy by approaching the tip to the vacancy and increasing the voltage steadily to 0.6 V.

Conclusion

In summary, HCM allows for the straightforward manipulation of single molecules of large organic adsorbates in bound assemblies. The strength of the method derives from the direct manual control of the AFM/STM tip. This allows the operator to explore the unknown potential in the state space of the manipulated system, quickly determining the manipulation trajectories that steer the system into the desired final state(s). By using HCM we were able to find the trajectories of the AFM/STM tip that break the intermolecular bonds in the molecular monolayer of PTCDA/Ag(111) and write the first ever complex structure with *large* molecules.

The HCM method reported here brings us a step closer to the possibility of building functional nanoscale molecular structures. In particular, it shows that in spite of the limited information about the junction that is accessible in real time, it is nevertheless possible to efficiently learn along which paths through the multidimensional state space with its highly complex potential molecules can be manipulated successfully. In future applications of the method, this learning could be delegated to a suitable computer algorithm. At the same time, the data collected with this method may promote a deeper understanding of interactions in complex adsorption systems and thus eventually help us to make another step towards machine-controlled molecular-scale functional design.

Supporting Information

The paper is accompanied by a ZIP archive containing the following files: The file "Manipulation-sequence.avi" contains the sequence of intermediate images recorded during the manipulation, the final result of which is shown in Figure 4. The file "3Dmovie.avi" contains an animation exhibiting the 3-D model of the recorded manipulation trajectories shown in Figure 3 (for details cf. the caption of Figure 3). The file "3Dmodel.html" contains an interactive 3-D model of the recorded manipulation trajectories. To be viewed it must be placed in the same directory as the file "CanvasMatrix.js" (included in the ZIP archive) and opened with a browser. Use the mouse to rotate or zoom the field of view of the 3-D model.

Supporting Information File 1

Additional experimental data
[http://www.beilstein-journals.org/bjnano/content/supplementary/2190-4286-5-203-S1.zip]

Acknowledgements

RT acknowledges support from the Helmholtz Association. CW acknowledges support from the European Union by a Marie-Curie Fellowship.

References

1. Eigler, D. M.; Schweizer, E. K. *Nature* **1990,** *344,* 524–526. doi:10.1038/344524a0
2. Heller, E. J.; Crommie, M. F.; Lutz, C. P.; Eigler, D. M. *Nature* **1994,** *369,* 464–466. doi:10.1038/369464a0
3. Heinrich, A. J.; Lutz, C. P.; Gupta, J. A.; Eigler, D. M. *Science* **2002,** *298,* 1381–1387. doi:10.1126/science.1076768
4. Sugimoto, Y.; Pou, P.; Custance, O.; Jelinek, P.; Abe, M.; Perez, R.; Morita, S. *Science* **2008,** *322,* 413–417. doi:10.1126/science.1160601
5. Ternes, M.; Lutz, C. P.; Hirjibehedin, C. F.; Giessibl, F. J.; Heinrich, A. J. *Science* **2008,** *319,* 1066–1069. doi:10.1126/science.1150288
6. Gomes, K. K.; Mar, W.; Ko, W.; Guinea, F.; Manoharan, H. C. *Nature* **2012,** *483,* 306–310. doi:10.1038/nature10941
7. IBM Research: A Boy And His Atom. http://researchweb.watson.ibm.com/articles/madewithatoms.shtml (accessed July 8, 2014).
8. Hla, S. W. *Rep. Prog. Phys.* **2014,** *77,* 056502. doi:10.1088/0034-4885/77/5/056502

9. Effectively the number of independent degrees of freedom of the junction is higher if one accounts for the applied electric bias and, e.g., vibrational motion of a cantilever.
10. Tautz, F. S. *Prog. Surf. Sci.* **2007,** *82,* 479–520. doi:10.1016/j.progsurf.2007.09.001
11. Kilian, L.; Hauschild, A.; Temirov, R.; Soubatch, S.; Schöll, A.; Bendounan, A.; Reinert, F.; Lee, T.-L.; Tautz, F. S.; Sokolowski, M.; Umbach, E. *Phys. Rev. Lett.* **2008,** *100,* 136103. doi:10.1103/PhysRevLett.100.136103
12. Toher, C.; Temirov, R.; Greuling, A.; Pump, F.; Kaczmarski, M.; Cuniberti, G.; Rohlfing, M.; Tautz, F. S. *Phys. Rev. B* **2011,** *83,* 155402. doi:10.1103/PhysRevB.83.155402
13. Rohlfing, M.; Temirov, R.; Tautz, F. S. *Phys. Rev. B* **2007,** *76,* 115421. doi:10.1103/PhysRevB.76.115421
14. Horcas, I.; Fernández, R.; Gómez-Rodriguez, J. M.; Colchero, J.; Gómez-Herrero, J.; Baro, A. M. *Rev. Sci. Instrum.* **2007,** *78,* 013705. doi:10.1063/1.2432410
15. Fournier, N.; Wagner, C.; Weiss, C.; Temirov, R.; Tautz, F. S. *Phys. Rev. B* **2011,** *84,* 035435. doi:10.1103/PhysRevB.84.035435
16. Wagner, C.; Fournier, N.; Tautz, F. S.; Temirov, R. *Phys. Rev. Lett.* **2012,** *109,* 076102. doi:10.1103/PhysRevLett.109.076102
17. Giessibl, F. J. *Rev. Mod. Phys.* **2003,** *75,* 949–983. doi:10.1103/RevModPhys.75.949
18. In contrast to the previous attempts to bring the AFM or STM tip under manual control, which mostly concentrated on providing a direct force feedback to the operator [23-25], our system is optimized for a precise positioning of the tip in all three dimensions rather than for haptic feedback. Note that since we use a dynamic version of the AFM, the true force-feedback is in fact impossible in our set-up since our AFM detects the first derivative of the force dF_z/dz only.
19. To get an idea how the junction structure evolves during the PTCDA peeling please refer to the supplementary section of [15].
20. Temirov, R.; Lassise, A.; Anders, F. B.; Tautz, F. S. *Nanotechnology* **2008,** *19,* 065401. doi:10.1088/0957-4484/19/6/065401
21. Greuling, A.; Rohlfing, M.; Temirov, R.; Tautz, F. S.; Anders, F. B. *Phys. Rev. B* **2011,** *84,* 125413. doi:10.1103/PhysRevB.84.125413
22. In all cases in which a molecule was damaged this occurred during the attempt to deposit it back to the surface.
23. Guthold, M.; Falvo, M. R.; Matthews, W. G.; Paulson, S.; Washburn, S.; Erie, D. A.; Superfine, R.; Brooks, F. P., Jr.; Taylor, R. M. *IEEE/ASME Trans. Mechatronics* **2000,** *5,* 189–198. doi:10.1109/3516.847092
24. Perdigão, L. M. A.; Saywell, A. *Rev. Sci. Instrum.* **2011,** *82,* 073704. doi:10.1063/1.3600572
25. Jobin, M.; Foschia, R.; Grange, S.; Baur, C.; Gremaud, G.; Lee, K.; Forró, L.; Kulik, A. *Rev. Sci. Instrum.* **2005,** *76,* 053701. doi:10.1063/1.1891346

License and Terms

The definitive version of this article is the electronic one which can be found at: doi:10.3762/bjnano.5.203

3

Scanning Quantum Dot Microscopy

Introduction

In the last decade the advantages of functionalizing the SPM tip have been established: by attaching a single, well-defined object to the tip, resolution can be improved and new physical effects can become accessible [53–60]. These benefits stem from the additional degrees of freedom (DoF) that the functionalizing object introduces [61]. For example, it was shown that the contrast enhancement in SPM images with a tip functionalized by a small probe particle came from the additional spatial DoF of the probe particle [62–64]. The principle can however be extended to different types of DoF, for example spin (spin-polarized STM [65]) or electronic DoF. These DoF of a different nature can be influenced by the microscope junction and induce previously unobservable effects, expanding the quantity of information that can be drawn from experiment.

Here we augment the SPM tip with the electronic degrees of freedom of a gateable QD, attached to the tip by controlled single molecule manipulation. The electronic coupling between the tip and QD is sufficiently weak such that discrete electronic states can exist on the QD, which can be populated and depopulated by gating. These charging events change the charge distribution in the microscope junction, leading to a change in the electrostatic force acting between tip and sample, which in turn can be detected in the AFM frequency shift signal. We go on to show how the gating is affected by local electrostatic potentials, leading to the invention of the new microscopy method, SQDM, where the charging events of a QD are used to map electrostatic potentials near surfaces. The method is demonstrated by the measurement of the potential of a single PTCDA molecule adsorbed on Ag(111), with quadrupolar (from the partial charges) and dipolar (from the charge transfer) contributions. This measurement compares favourably to a microelectrostatic simulation of the potential, which suggests that the potential is detected at a well-defined point below the apex of the metal tip. The quantitative nature of the technique is thereafter displayed by the measurement of the Smoluchowski dipole of a single silver adatom, which follows a z^{-2} decay law as expected. Finally, the detection of the Smoluchowski potential at $\sim$7 nm from the atom demonstrates the outstanding sensitivity of SQDM. Since the active element of the SQDM sensor is the molecular QD, it can be described as a single molecule device.

3.1. Scanning Quantum Dot Microscopy

The journal article in this section was published in Physical Review Letters [66]. The author contributions are as follows: C.W., M.F.B.G., R.T. and F.S.T. conceived the experiments. M.F.B.G. and P.L. performed the experiments. C.W., M.F.B.G. and R.T. analyzed the data. T.D., P.K. and M.R. performed the DFT calculations. C.W., M.F.B.G., R.T. and F.S.T. wrote the paper and all authors discussed the manuscript.

Scanning Quantum Dot Microscopy

Christian Wagner,[1,2] Matthew F. B. Green,[1,2] Philipp Leinen,[1,2] Thorsten Deilmann,[3] Peter Krüger,[3] Michael Rohlfing,[3] Ruslan Temirov,[1,2,*] and F. Stefan Tautz[1,2]

[1]*Peter Grünberg Institut (PGI-3), Forschungszentrum Jülich, 52425 Jülich, Germany*

[2]*Jülich Aachen Research Alliance (JARA)–Fundamentals of Future Information Technology, 52425 Jülich, Germany*

[3]*Institut für Festkörpertheorie, Westfälische Wilhelms-Universität Münster, 48149 Münster, Germany*

(Received 26 February 2015; published 6 July 2015)

We introduce a scanning probe technique that enables three-dimensional imaging of local electrostatic potential fields with subnanometer resolution. Registering single electron charging events of a molecular quantum dot attached to the tip of an atomic force microscope operated at 5 K, equipped with a qPlus tuning fork, we image the quadrupole field of a single molecule. To demonstrate quantitative measurements, we investigate the dipole field of a single metal adatom adsorbed on a metal surface. We show that because of its high sensitivity the technique can probe electrostatic potentials at large distances from their sources, which should allow for the imaging of samples with increased surface roughness.

DOI: 10.1103/PhysRevLett.115.026101 PACS numbers: 68.37.-d, 73.23.Hk, 82.37.Gk, 85.65.+h

The atomic structure of matter inevitably leads to local electrostatic fields in the vicinity of nanoscale objects even if they are neutral [1]. Hence, electrostatic forces often dominate the interactions between nanostructures, but experimental access to such local electrostatic fields is a challenge, Kelvin probe force microscopy (KPFM) being the most promising attempt to address it so far [2–4]. However, since KPFM measures the contact potential difference between surfaces, which by definition are extended objects, it inevitably involves lateral averaging, especially for larger probe-to-surface distances. True three-dimensional imaging of local electrostatic fields in a broad distance range is therefore difficult with KPFM [5].

Here we introduce a scanning probe technique, scanning quantum dot microscopy (SQDM), that provides a contact-free measurement of the electrostatic potential in all three spatial dimensions, without the drawback of distance-dependent averaging. This is possible because SQDM, unlike KPFM, directly probes the local electrostatic potential at a well-defined subnanometer-sized spot in the junction. SQDM also shows a remarkable sensitivity that allows, e.g., the detection of the electrostatic potential ~6 nm above a single adatom on a metal surface.

We start by describing the general working principle of SQDM, independent of the specific nature of the employed quantum dot (QD). We image the electrostatic potential using a nanometer-sized QD attached to the apex of a scanning probe tip [Fig. 1(a)]. In the experiment, the electronic levels of the QD are gated with respect to the Fermi level E_F of the tip by applying a bias voltage to the tip-surface junction [Fig. 1(b)] [6–10]. In this way, the charge state of the QD can be changed, e.g., if the bias voltage V applied to the junction reaches a critical value V^- that aligns one of the QD's occupied electronic levels with E_F, this level is depopulated [Fig. 1(b)]. With this device, the measurement of a local electrostatic potential field

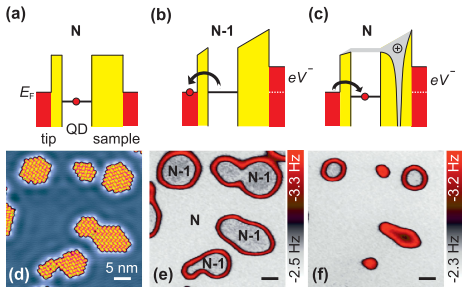

FIG. 1 (color). Working principle of SQDM. (a)–(c) Energy diagrams showing the QD attached to a scanning probe tip. (a) In the absence of a sample bias, a given level of the QD is occupied (QD charge state N). (b) When a critical sample bias V^- is reached, one electron tunnels from the QD into the tip (QD charge state $N-1$). (c) If a local charge at the surface modifies the potential in the junction, the QD level shifts and becomes reoccupied (QD charge state N). (d) STM image of monolayer PTCDA islands on Ag(111). Here, and on all further images, a 5 nm scale bar is shown. (e) Const. height Δf image of the area in (d) recorded at $z_{tip} = 3$ nm [for definition, see Fig. 2(a)] and $V = -990$ mV. Prominently visible in red are lines where the QD changes its occupation between N and $N-1$. The charge states of the QD in the different regions are labeled. (f) Same as (e), but recorded at $V = -910$ mV.

$\Phi(x, y, z)$, caused for example by a surface adsorbate, is possible because the electronic levels of the QD shift in response to any perturbation of the potential at the position (x, y, z) of the QD. These shifts can be detected by their effect on the charge state [Fig. 1(c)]. Detecting charging events of the QD while scanning the three-dimensional half-space above the surface is the working principle of our method.

Figures 1(e) and 1(f), recorded 3 nm above islands of perylene tetracarboxylic dianhydride (PTCDA) on the Ag(111) surface, provide an initial illustration of SQDM imaging. The red contours in Figs. 1(e) and 1(f) mark locations where the QD changes its charge state. Note that these contours follow the shape of the standing wave pattern [Fig. 1(d)], which is formed by the surface state as it is scattered by the perturbed electrostatic potential in the surface [11]. This is an indication that the QD is indeed sensitive to the electrostatic potential created by the sample. In the remainder of the Letter, we present experimental results that unambiguously confirm this conjecture.

We now turn to a description of the QD used in the present work. Since the spatial resolution of SQDM is related to the size of the QD, we chose a single molecule as the QD to optimize it. Two questions then arise: is it possible to controllably attach a single molecule to the tip of the scanning probe microscope, and does this molecule indeed exhibit the properties of a QD?

Regarding the first question, we were able to attach both single PTCDA and naphthalene tetracarboxylic dianhydride (NTCDA) molecules [Figs. 2(a) and 2(b)] to the apex of the tip of a CREATEC qPlus tuning fork [12] noncontact atomic force/scanning tunneling microscope (NC-AFM/STM), operated at 5 K and in ultrahigh vacuum. This is achieved with a well-documented manipulation routine [13–16]: an isolated PTCDA or NTCDA molecule, adsorbed on Ag(111), is approached by the silver-terminated AFM/STM tip directly above one of its corner oxygen atoms. At a tip-surface distance of ~6.5 Å, the chosen oxygen atom flips up by ~1.4 Å to establish a chemical bond to the apex of the metal tip [13]. By this oxygen-silver bond, the entire molecule can be lifted off the surface [13,14]. As the final bond between the molecule and the surface is broken, the attractive interaction with the surface aligns the molecule perpendicularly to the surface [15,16] in a configuration in which the molecule is hanging from the tip by its oxygen-silver bond [Fig. 2(a)] [17].

The tip-suspended PTCDA and NTCDA molecules behave as QDs because their frontier orbitals have π character and a weak amplitude at the corner oxygen atoms. Moreover, in the given configuration, the lobes point in a direction that minimizes overlap with the tip; hence, the bond to the tip acts as an insulating spacer, which prevents their hybridization with the tip. This results in very sharp line widths [13,18] and, equally importantly, in the possibility to gate these levels because a sizeable fraction of

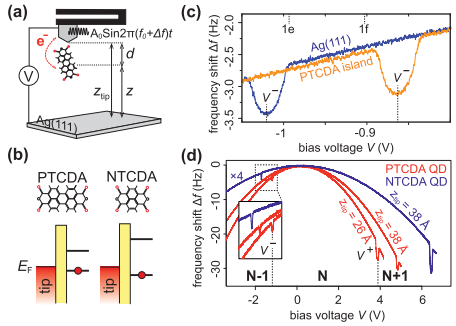

FIG. 2 (color). SQDM with a molecular QD and a NC-AFM. (a) Schematic view of the QD sensor: A single PTCDA molecule is chemically bonded to the AFM tip via a corner oxygen atom. The definitions of z_{tip}, z, and d are indicated. The calibration of z_{tip} was performed as described in Ref. [16]. (b) Schematics of the energy level alignment of the PTCDA and NTCDA QD tips. (c) $\Delta f(V)$ spectra taken with the PTCDA QD tip at $z_{tip} = 3$ nm above the clean Ag(111) surface (blue) or above a PTCDA island (orange). The center of each dip determines V^-. The voltages used for scanning Figs. 1(e) and 1(f) are indicated at the top. (d) $\Delta f(V)$ spectra, recorded with PTCDA (red) and NTCDA (blue) QD tips above the bare Ag(111) surface. The NTCDA spectrum is multiplied by 4. For the PTCDA spectrum, recorded at $z_{tip} = 26$ Å, the QD charge states $N-1$, N, and $N+1$ are indicated.

the applied bias voltage drops over the insulating oxygen-tip bond. It should be noted, however, that in some respects the properties of our molecular QDs differ from those of more conventional QDs: first, due to large (and size-dependent) intramolecular Coulomb repulsion, the charging energies are in the eV rather than the meV range, and second, particle-hole symmetry is broken [19]. In fact, while both NTCDA and PTCDA show the same functionality, the actual level alignment and smaller level spacing in PTCDA [Fig. 2(b)] make it more convenient to work with. Therefore, we focus on experiments with the PTCDA QD tip. The data obtained with NTCDA can be found in the Supplemental Material [18].

Since electrostatic potential measurements in SQDM are based on changes of the QD's electron occupation, a sensitive detection of charging events is crucial. Here this is accomplished by registering abrupt steps in the tip-sample force that accompany the change of the QD's charge state [6–8,10]. In the qPlus NC-AFM, these steps show up as sharp dips in the frequency shift curve $\Delta f(V)$ [Fig. 2(c)] [12,20,21].

Based on our detection method, SQDM images can be recorded either by mapping Δf [Figs. 1(e) and 1(f)] or by plotting constant-height maps of charging voltages V^- [Fig. 2(c)]. If only one Δf feature is used, the resulting SQDM contrast contains a combination of electrostatic and topography effects. Fortunately, we are able to detect *two*

$\Delta f(V)$ features (at V^- and V^+), corresponding to the $N \rightarrow N-1$ and $N \rightarrow N+1$ transitions of the QD [Fig. 2(d)] [22]. The simultaneous analysis of both $\Delta f(V)$ features allows for a straightforward disentanglement of topography and electrostatics.

The fact that topographic signatures in the surface can change the charge state of the QD if it is scanned at constant height (i.e., fixed z) across the surface is naturally explained by changes of the junction capacitance with the distance between tip and sample [7]. The effect is illustrated in Fig. 2(d) by the observation that the absolute values $|V^+|$ and $|V^-|$ increase with z_{tip}. We describe this behavior in terms of a "gating efficiency" α. A smaller value of α implies that a larger bias is needed to align any given QD level with E_{F}. In contrast to the topography, a local electrostatic potential Φ^* at the position of the QD shifts V^- and V^+ rigidly on the voltage axis ($\Delta V \equiv V^+ - V^- = \mathrm{const}$). For a fixed z, the separation of Φ^* from topography can be achieved straightforwardly by writing down the charging conditions $E_{\mathrm{hole}} + \alpha e V^- + e\Phi^* = 0$ and $E_{\mathrm{el}} - \alpha e V^+ - e\Phi^* = 0$ (E_{el} and E_{hole} are the electron and hole charging energies of the QD) for transitions $N \rightarrow N-1$ and $N \rightarrow N+1$, respectively, and solving for α and Φ^*. The result is $\alpha = C/\Delta V$ and $\Phi^* = -CV^-/\Delta V + \Phi_0^*$, where C and Φ_0^* are constants that can be determined by a calibration experiment where $\Phi^* = 0$ (see below). Details can be found in the Supplemental Material [18]. The fact that ΔV is inversely proportional to α shows that it primarily carries information about the topography [23].

We now demonstrate the power of SQDM by mapping out the local electrostatic potential field of a nanostructure. As the latter, we choose a single PTCDA molecule on Ag(111). Its field is expected to contain two major contributions, a quadrupolar field, produced by the internal charge distribution of the molecule [Fig. 3(a)], and a dipolar field due to the electron transfer from Ag(111) to PTCDA upon adsorption [24].

Using the PTCDA QD, we measure V^- and V^+ on a grid above the adsorbed PTCDA molecule and plot in Figs. 3(a)–3(f) the experimental quantities $\Delta V(x,y)$, related to the topography, and $V^-/\Delta V(x,y)$, proportional to the electrostatic potential (up to a constant offset). Figures 3(d)–3(f) bear a close resemblance to the expected molecular quadrupole field. This is reinforced by a comparison to the results of a microelectrostatic simulation, in which the internal charge distribution of a gas-phase PTCDA, as calculated by density functional theory (DFT), its screening by the metal, and a homogeneous charge transfer from the metal to the molecule have been taken into account. The simulated images in Figs. 3(g)–3(i) were obtained by fitting the experimental data from Figs. 3(d)–3(f) with a two-parameter model, the first parameter being the charge transfer from Ag(111) to PTCDA ($q = -0.09\,e$), and the second parameter the distance z from the surface at

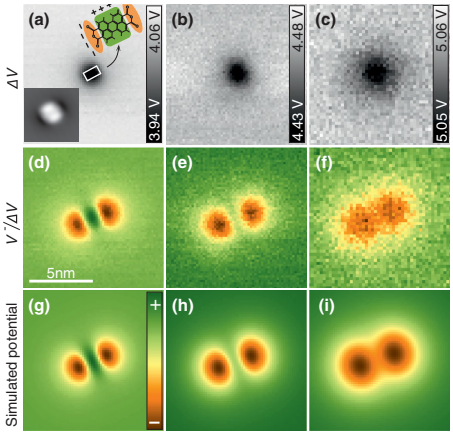

FIG. 3 (color). PTCDA on Ag(111): separation of topographic and electrostatic contrasts in SQDM. (a)–(c) Experimental $\Delta V(x,y)$ maps (related to topography, cf. text) recorded with the PTCDA QD tip above an isolated PTCDA molecule adsorbed on the Ag(111) surface. (a) A white rectangle outlines the size of the PTCDA molecule. In the upper right corner, an enlarged structure formula, on which the quadrupolar charge distribution is indicated, is displayed. The inset in the bottom left corner shows an STM image [scale as in (a)]. (d)–(f) Experimental $V^-/\Delta V(x,y)$ maps (related to electrostatic potential, cf. text) of the same area as in (a)–(c). Maps (a) and (d) were recorded at $z_{\mathrm{tip}} = 24$ Å, (b) and (e) at 28 Å, and (c) and (f) at 36 Å. (g)–(i) Simulated electrostatic potential of adsorbed PTCDA at $z = 16$ Å (g), 22 Å (h), and 28 Å (i). The color scales in (d)–(i) were adjusted to optimize the contrast of each figure.

which the simulated potential is plotted [16 Å, 22 Å, and 28 Å in Figs. 3(g), 3(h), and 3(i), respectively]. Remarkably, comparing the obtained distances z with the experimental z_{tip} [24 Å, 28 Å, and 36 Å in Figs. 3(d), 3(e), and 3(f)], we obtain an estimate of $d = (7 \pm 1)$ Å in Fig. 2(a). This shows that the electrostatic potential is probed at a point approximately 7 Å below the tip apex, hence at the position of the PTCDA QD, as expected from the proposed junction geometry [Fig. 2(a)].

We now choose the Smoluchowski dipole [1], created here by a single Ag atom adsorbed on Ag(111) [Figs. 4(a)–4(c)], to demonstrate that SQDM can deliver *quantitative* three-dimensional electrostatic potential imaging. To this end, reference measurements $V_0^-(z)$ and $V_0^+(z)$ (for a fixed set of heights z) at locations where the local electrostatic potential Φ^* is taken to be zero, e.g., above bare Ag(111), can be used to eliminate the z-dependent constants C and Φ_0^*. In this way, Φ^* can be evaluated from $\Phi^*(x,y,z) = -\alpha_0(z)\{[V^-(x,y,z)/\Delta V(x,y,z)]\Delta V_0(z) - V_0^-(z)\}$ [18], where $\alpha_0(z)$ is the z-dependent gating efficiency when the QD tip is above bare Ag(111). In the simplest case, $\alpha_0(z) = d/(z+d)$, if a plate capacitor geometry is assumed. Figure 4(d) shows the experimental

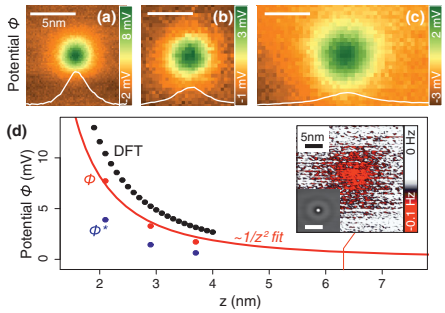

FIG. 4 (color). Smoluchowski dipole of an adatom: quantitative electrostatic potential measurements with SQDM. (a)–(c) Electrostatic potential maps $\Phi(x, y)$ measured above a silver adatom on Ag(111) at $z = 21$ Å (a), 29 Å (b), and 37 Å (c). The scale bars show the absolute values of the electrostatic potential Φ, obtained as described in the text. Line profiles through the adatom are shown in white. (d) Comparison of the experimental $\Phi^\star$ (blue), Φ (red), and DFT-calculated (black) potentials vertically above the adatom. The red line shows a $1/(z - z_0)^2$ fit of the experimental data, where z_0 was obtained by fitting the DFT dataset. For the experimental data, z is the distance between the point inside the QD, at which the electrostatic potential is measured, and the surface. For DFT, z is the distance from the surface at which the potential of the adatom was calculated. (Inset) Constant height raw Δf image recorded at $z = 6.3$ nm with an applied bias of $V = 9.6$ V, close to V^+ for this z. (Bottom left corner) STM image of the adatom.

electrostatic potential vertically above the adatom, evaluated by the above formula, in comparison to the result of a DFT calculation [25].

Before making the comparison, one should note that DFT yields the electrostatic potential Φ in the absence of the tip. It is clear that the grounded tip screens the local electrostatic potential Φ to a smaller value Φ^*. Taking into the account this screening [28], we obtain an experimental Φ that is ~70% of the DFT values. We consider this agreement a remarkable verification of quantitative electrostatic potential mapping in SQDM. The remaining discrepancy between theory and experiment can be explained by an increase of α (in comparison to the plate capacitor model), caused by the curvature of the metal tip used in the experiment. We note that this influence can be quantified by measuring a structure whose electrostatic potential is known and then transferred to any other experiment with the same tip.

Finally, we comment on the sensitivity of our electrostatic potential field measurement. An accuracy of ~1 mV in measuring V^-, V^+ translates into $\Phi^*(z)$ from the adatom being detectable at z up to ~4 nm. The inset in Fig. 4(d) shows that, imaging Δf directly, the Smoluchowski dipole field of the adatom is observed even at a distance of 6.3 nm from the surface.

In conclusion, we have reported a scanning probe technique that is able to provide truly three-dimensional, so far elusive, maps of the electrostatic potential field with nanometer resolution. Since the QD serves as a sensor of the electrostatic potential that at the same time transduces this signal to a charging event, the technique is a particularly interesting variant of the general sensor-transducer concept for scanning probe microscopy introduced earlier [29–31]. Here, however, the transduction involves electronic rather than the mechanical degrees of freedom that were utilized in previous work.

As a consequence of its high sensitivity, SQDM may in the future be applied to the characterization of rough and high-aspect-ratio samples such as semiconductor devices or large biomolecular structures [18]. Moreover, the combination of high sensitivity and spatial resolution suggests the possibility of reading nanoscale electric memory cells entirely contact and current free. Finally, we stress that the molecular QD realization of SQDM reported here, although particularly attractive, does not exhaust all possibilities [32]. SQDM probes with nano-fabricated QDs on standard silicon AFM cantilevers may in the future extend the applicability beyond ultrahigh vacuum and cryogenic temperatures.

T. D., P. K., and M. R. gratefully acknowledge the computing time granted by the John von Neumann Institute for Computing (NIC) and provided on the supercomputer JUROPA at Jülich Supercomputing Centre (JSC). R. T. acknowledges discussions with D. Ryndyk (TU-Dresden) and H. Vázquez (AS CR).

*r.temirov@fz-juelich.de

[1] R. Smoluchowski, Anisotropy of the Electronic Work Function of Metals, Phys. Rev. **60**, 661 (1941).
[2] M. Nonnenmacher, M. P. O'Boyle, and H. K. Wickramasinghe, Kelvin probe force microscopy, Appl. Phys. Lett. **58**, 2921 (1991).
[3] L. Gross, F. Mohn, P. Liljeroth, J. Repp, F. Giessibl, and G. Meyer, Measuring the charge state of an adatom with noncontact atomic force microscopy, Science **324**, 1428 (2009).
[4] F. Mohn, L. Gross, N. Moll, and G. Meyer, Imaging the charge distribution within a single molecule, Nat. Nanotechnol. **7**, 227 (2012).
[5] B. Schuler, S. Liu,Y. Geng, S. Decurtins, G. Meyer, and L. Gross, Contrast formation in Kelvin probe force microscopy of single π-conjugated molecules, Nano Lett. **14**, 3342 (2014).
[6] M. T. Woodside and P. L. McEuen, Scanned probe imaging of single-electron charge states in nanotube quantum dots, Science **296**, 1098 (2002).
[7] R. Stomp, Y. Miyahara, S. Schaer, Q. Sun, H. Guo, P. Grutter, S. Studenikin, P. Poole, and A. Sachrajda, Detection of Single-Electron Charging in an Individual InAs Quantum Dot by Noncontact Atomic-Force Microscopy, Phys. Rev. Lett. **94**, 056802 (2005).
[8] L. Cockins, Y. Miyahara, S. D. Bennett, A. Clerk, S. Studenikin, P. Poole, and P. Grutter, Energy levels of

few-electron quantum dots imaged and characterized by atomic force microscopy, Proc. Natl. Acad. Sci. U.S.A. **107**, 9496 (2010).

[9] I. Fernandez-Torrente, D. Kreikemeyer-Lorenzo, A. Stróżecka, K. J. Franke, and J. I. Pascual, Gating the Charge State of Single Molecules by Local Electric Fields, Phys. Rev. Lett. **108**, 036801 (2012).

[10] C. Lotze, PhD Thesis, Freie Universität Berlin, 2013.

[11] M. F. Crommie, C. P. Lutz, and D. M. Eigler, Imaging standing waves in a two-dimensional electron gas, Nature (London) **363**, 524 (1993).

[12] F. J. Giessibl, Advances in atomic force microscopy, Rev. Mod. Phys. **75**, 949 (2003).

[13] C. Toher, R. Temirov, A. Greuling, F. Pump, M. Kaczmarski, G. Cuniberti, and F. S. Tautz, Electrical transport through a mechanically gated molecular wire, Phys. Rev. B, **83**, 155402 (2011).

[14] N. Fournier, C. Wagner, C. Weiss, R. Temirov, and F. S. Tautz, Force-controlled lifting of molecular wires, Phys. Rev. B **84**, 035435 (2011).

[15] C. Wagner, N. Fournier, F. S. Tautz, and R. Temirov, Measurement of the Binding Energies of the Organic-Metal Perylene-Tetracarboxylic-Dianhydride/Au(111) Bonds by Molecular Manipulation using an Atomic Force Microscope, Phys. Rev. Lett. **109**, 076102 (2012).

[16] C. Wagner, N. Fournier, V. G. Ruiz, C. Li, K. Müllen, M. Rohlfing, A. Tkatchenko, R. Temirov, and F. S. Tautz, Non-additivity of molecule-surface van der Waals potentials from force measurements, Nat. Commun. **5**, 5568 (2014).

[17] This configuration has been validated, e.g., by DFT simulations [13] and by quantitative measurements of the van der Waals attraction in this geometry [16], and it is in fact further supported by the QD properties of the tip-suspended molecules because any overlap of the molecular π electron system with the metal tip would destroy these properties.

[18] See Supplemental Material at http://link.aps.org/supplemental/10.1103/PhysRevLett.115.026101 for a PTCDA QD level width measurement, the derivation of the expressions for α and Φ^*, and for additional SQDM images recorded with PTCDA and NTCDA QDs.

[19] We explain the breaking of particle-hole symmetry, i.e., the fact that unlike in Ref. [7] V^- and V^+ are not symmetric with respect to zero, by the presence of electric fields that originate from charge transfer effects that are caused by the attachment of the molecule to the tip. Our data suggest that in the state N the molecules are slightly negatively charged. Hence, it requires less voltage to decrease the occupation of the dot (V^-) than to increase it (V^+).

[20] Our NC AFM, operated in the frequency modulation mode, measures the gradient dF_z/dz of the vertical force F_z acting on the tip, which oscillates with sub-Å amplitudes [12].

[21] We note that the molecular QDs employed here show no dissipation signal at these charging events because, due to the meV level widths, the corresponding time scales are of the order of picoseconds and thus much shorter than the oscillation period of the qPlus sensor ($\sim$30 μs). Hence, no charging hysteresis and no dissipation will occur.

[22] Note that V^- and V^+ charging events appear on top of the parabola, which originates from the attractive interaction between the opposing electrodes of the biased tip-surface junction [3].

[23] Note that local variations of the surface dielectric constant can also change the gating efficiency α.

[24] Y. Zou, L. Kilian, A. Schöll, T. Schmidt, R. Fink, and E. Umbach, Chemical bonding of PTCDA on Ag surfaces and the formation of interface states, Surf. Sci. **600**, 1240 (2006).

[25] The DFT calculation was carried out using the SIESTA package [26,27]. The exchange-correlation part was treated within the local-density approximation, which gives realistic results for strongly bound adsorbates like the Ag adatom considered here. The adatom adsorbs at the hollow site with a height of 2.11 Å, which is 0.25 Å closer to the surface than its ideal position would be. In order to calculate the electrostatic potential in real space, we decompose the charge density into two parts, by the clean surface and by the adatom. The main contribution of the Ag adatom originates from a region of about 4 Å around the adatom. Since the potential of the clean neutral surface decays exponentially with increasing height, only the charge density contribution due to the adatom causes a measurable electrostatic potential at the position of the QD. This potential is evaluated from the charge density by solving Poisson's equation in real space, without any supercell periodicity.

[26] P. Ordejon, E. Artacho, and J. M. Soler, Self-consistent Order-N density functional calculations for very large systems, Phys. Rev. B **53**, R10441 (1996).

[27] J. M. Soler, E. Artacho, J. D. Gale, A. Garcia, J. Junquera, P. Ordejón, and D. Sánchez-Portal, The SIESTA method for *ab initio* order-N materials simulation, J. Phys. Condens. Matter **14**, 2745 (2002).

[28] The screening was evaluated by considering an elementary electrostatic model of a point charge in front of an infinite metal surface.

[29] G. Kichin, C. Weiss, C. Wagner, F. S. Tautz, and R. Temirov, Single molecule and single atom sensors for atomic resolution imaging of chemically complex surfaces, J. Am. Chem. Soc. **133**, 16847 (2011).

[30] P. Hapala, G. Kichin, C. Wagner, F. S. Tautz, and P. Jelínek, Mechanism of high-resolution STM/AFM imaging with functionalized tips, Phys. Rev. B **90**, 085421 (2014).

[31] C. Wagner and R. Temirov, Tunnelling junctions with additional degrees of freedom: An extended toolbox of scanning probe microscopy, Prog. Surf. Sci. **90**, 194 (2015).

[32] M. Hauser, J. Smoliner, C. Eder, G. Ploner, G. Strasser, and E. Gornik, Single quantum dots as scanning tunneling microscope tips, Superlattices Microstruct. **20**, 623 (1996).

3.2. Scanning Quantum Dot Microscopy: Supplemental Information

The supplemental information to the journal article 'Scanning Quantum Dot Microscopy' is presented in this section.

Scanning Quantum Dot Microscopy: Supplemental Information

Christian Wagner,[1,2] Matthew F. B. Green,[1,2] Philipp Leinen,[1,2]
Thorsten Deilmann,[3] Peter Krüger,[3] Michael Rohlfing,[3]
Ruslan Temirov,[1,2*] F. Stefan Tautz[1,2]

[1]Peter Grünberg Institut (PGI-3), Forschungszentrum Jülich, 52425 Jülich, Germany
[2]Jülich Aachen Research Alliance (JARA)-Fundamentals of Future Information Technology, 52425 Jülich, Germany
[3]Institut für Festkörpertheorie, Westfälische Wilhelms-Universität Münster, 48149 Münster, Germany
*To whom correspondence should be addressed; E-mail: r.temirov@fz-juelich.de.

April 15, 2015

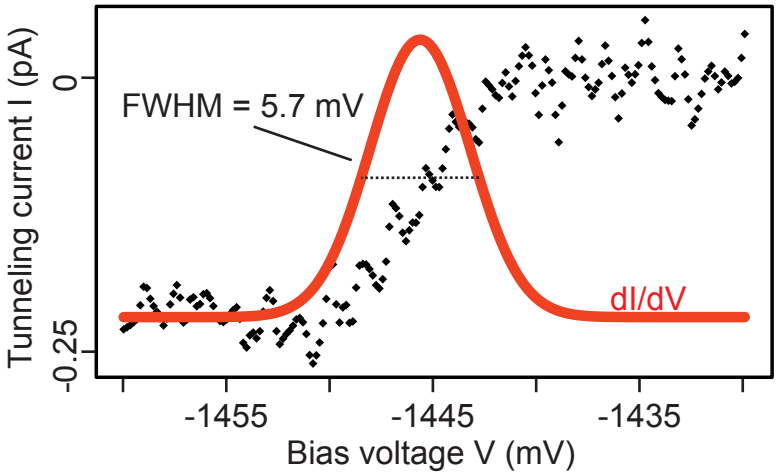

Figure S1: **Interaction between the PTCDA quantum dot and the tip electrode**, as determined from charge transport between the tip and the Ag(111) surface through the PTCDA quantum dot. The black data points show a sharp increase of the tunneling current I that occurs when the occupied level of the quantum dot crosses E_F of the tip at the bias voltage V^- and thus moves inside the bias window, becoming a channel for charge transport. The red curve shows the corresponding peak in the differential conductance dI/dV, the width of which is directly related to the width of the PTCDA level. Taking into account a thermal broadening of $5.4\,kT$, the Figure reveals that the broadening of the occupied PTCDA level through the interaction with the tip is smaller than 3.5 mV.

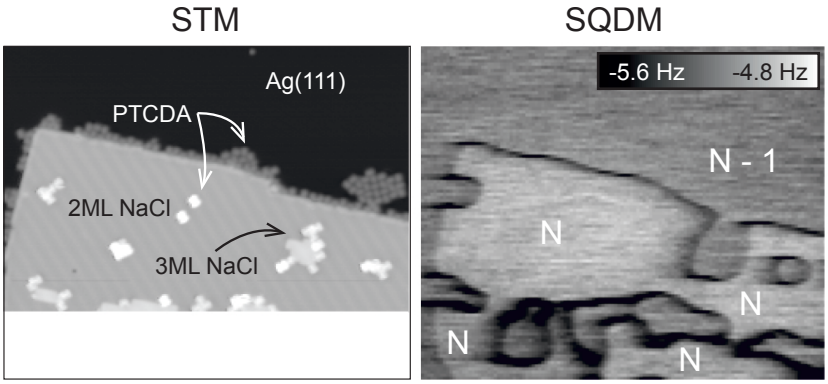

Figure S2: **SQDM imaging (with a PTCDA QD tip) of a PTCDA/NaCl/Ag(111) surface.** Size of the images 60×50 nm^2. Left panel: constant current STM image taken at $V = 2$ V and $I = 12$ pA with a clean metal tip. Right panel: constant height Δf image taken with the PTCDA QD tip, scanning the surface at $z_{\rm tip} \approx 4$ nm and $V = -2.07$ V. The sharp black boundaries mark the areas where the PTCDA QD changes its charge state. In the STM image, the lower part of the frame was not scanned, because in this area a large number of unstable islands, which are prone to be disturbed by the tip in conventional STM scanning conditions, is located. Note that, because of the large distance to the surface, imaging such unstable areas is no problem in SQDM. This illustrates the potential of SQDM to provide images of rough and delicate samples, as mentioned in the paper.

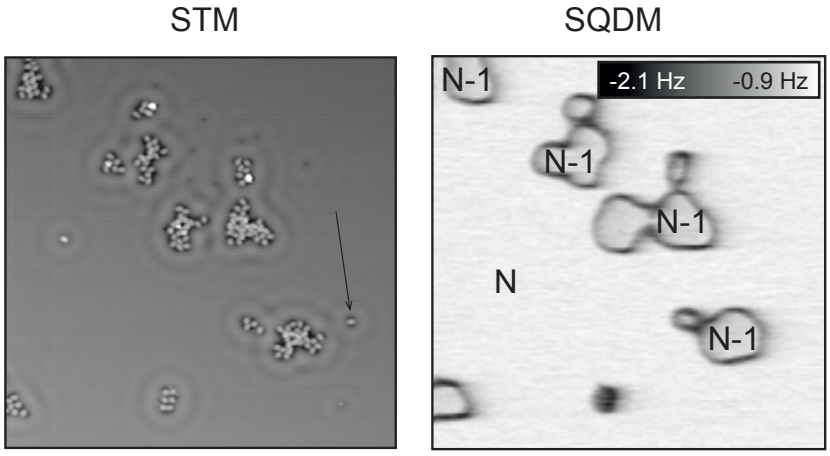

Figure S3: **SQDM imaging (with a NTCDA QD tip) of disordered NTCDA islands grown on the Ag(111) surface at** $110\,\mathrm{K}$**.** Size of the images 60×60 nm^2. Left panel: const. current STM image taken at $V = 50$ mV and $I = 50$ pA. The black arrow points to an isolated NTCDA molecule that was used as the QD to acquire the image shown in the right panel. After imaging, the molecule was deposited back to the shown location by applying a 0.6 V pulse to the tip in the close vicinity of the surface. Right panel: const. height Δf image taken with the NTCDA QD tip scanning the surface at $z_{\mathrm{tip}} \approx 3$ nm and $V = -1.32$ V. The sharp black boundaries mark the areas where the NTCDA QD changes its charge state.

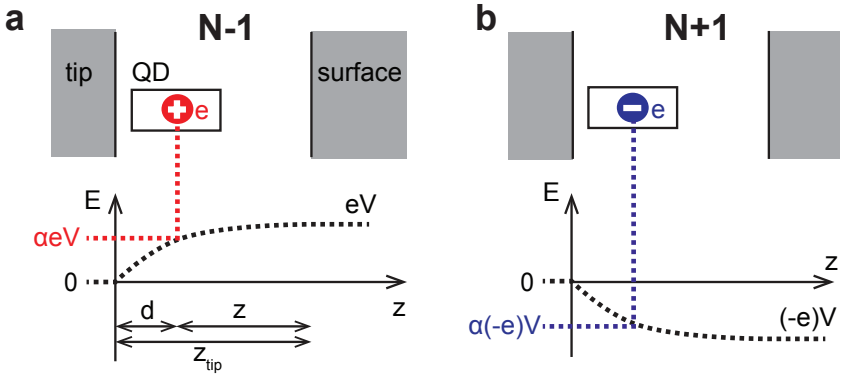

Figure S4: **Schematic diagram of the SQDM junction.** In **a**, the dot is positively charged with one hole (total number of electrons $N-1$), while in **b** the dot is negatively charged with one electron (total number of electrons $N+1$). V is the bias applied to the tip-surface junction. In both figures the bias V is positive. The thick dotted lines shows the energy of a hole (panel **a**, charge $+e$) or the energy of an electron (panel **b**, charge $-e$) as a function of z. The positive bias V tends to stabilize the electron in the dot (panel **b**), but to destabilize the hole in the dot (panel **a**). The stabilization and destabilization energies are shown in blue and red, respectively.

1 Extraction of constant height $\Phi^*(x,y)$ and $\alpha(x,y)$ images

Considering the diagrams shown in Figs. S4a-b, the energies of the states of the junction can be written as follows:

$$E(N-1) = E_{\text{hole}} + \alpha eV + e\Phi^* \tag{S1}$$

and

$$E(N+1) = E_{\text{el}} - \alpha eV - e\Phi^*, \tag{S2}$$

where E_{hole} (E_{el}) is the energy needed to create a hole (electron) in the quantum dot when no bias voltage V is applied to the junction. $\pm\alpha eV$ is the energy associated with the position of the hole or electron in the electrostatic potential created by the bias voltage V. α is the gating efficiency which determines which fraction of the bias voltage V drops between the tip and the quantum dot. Finally, Φ^* is an additional electrostatic potential present at the position of the quantum dot, created, e.g., by a nanostructure in the vicinity. In our experiment Φ^* is the measured quantity.

The charging conditions can be written as $E(N-1)=0$ and $E(N+1)=0$. This leads to a pair of equations

$$E_{\mathrm{hole}} + \alpha e V^- + e\Phi^* = 0 \tag{S3}$$

$$E_{\mathrm{el}} - \alpha e V^+ - e\Phi^* = 0, \tag{S4}$$

in which V^+ and V^- are the charging voltages measured in the experiment (cf. main text). From eqs. S3 and S4 we obtain

$$\alpha = \frac{E_{\mathrm{hole}} + E_{\mathrm{el}}}{e(V^+ - V^-)} = \frac{E_{\mathrm{hole}} + E_{\mathrm{el}}}{e\Delta V} \tag{S5}$$

$$\Phi^* = -\frac{V^-}{e\Delta V}(E_{\mathrm{hole}} + E_{\mathrm{el}}) - \frac{E_{\mathrm{hole}}}{e} \tag{S6}$$

Assuming that neither E_{hole} nor E_{el} changes when the tip is scanned at constant height (i.e. fixed z) across the surface, eqs. S5 and S6 show that from the measured $V^+(x,y)$, $V^-(x,y)$ at a given z we can obtain maps of the gating efficiency $\alpha(x,y)$ and the potential $\Phi^*(x,y)$ at this z, up to a scaling factor and an offset. In Figs. 3a-c of the main paper we plot the measured ΔV, related to α^{-1}, and in Figs. 3d-f of the main paper we plot the measured dimensionless quantity $V^-/\Delta V$, related to Φ^*.

2 Reference Measurement at constant z

The unknown scaling factor $(E_{\mathrm{hole}} + E_{\mathrm{el}})/e$ (appearing in the main text as C) and offset E_{hole}/e (appearing in the main text as Φ_0^*) in eqs. S5 and S6 can be eliminated by a reference measurement at a point (x_0, y_0) at which the local electrostatic potential Φ^* is zero, e.g. above the bare Ag(111) surface. It is important that this reference measurement is carried out at the same z at which $\alpha(x,y)$ and $\Phi^*(x,y)$ are evaluated. If the local electrostatic potential Φ^* is zero, eqs. S3 and S4 become

$$E_{\mathrm{hole}} = -\alpha_0 e V_0^- \tag{S7}$$

$$E_{\mathrm{el}} = \alpha_0 e V_0^+ \tag{S8}$$

where $\alpha_0 = \alpha(x_0, y_0)$, $V_0^- = V^-(x_0, y_0)$ and $V_0^+ = V^+(x_0, y_0)$ determined at the chosen fixed z.

Using eqs. S7 and S8, eqs. S5 and S6 become

$$\alpha(x,y) = \alpha_0 \left(\frac{\Delta V_0}{\Delta V(x,y)} \right) \tag{S9}$$

and

$$\Phi^*(x,y) = -\alpha_0 \left(\frac{V^-(x,y)}{\Delta V(x,y)} \Delta V_0 - V_0^- \right) \tag{S10}$$

where $\Delta V_0 = V_0^+ - V_0^-$. According to eqs. S9 and S10, both the gating efficiency α and the potential Φ^* can be fully expressed in terms of measurable quantities, up to a common scaling factor α_0.

3 Measurement of $\Phi^*(x,y,z)$

Eq. S10 can be directly applied to the measurement of Φ^* at an arbitrary location (x,y,z) if the reference data $V_0^-(z)$ and $V_0^+(z)$ are available. Since the scaling factor α_0 in eq. S10 is generally z-dependent, we obtain

$$\Phi^*(x,y,z) = -\alpha_0(z) \left(\frac{V^-(x,y,z)}{\Delta V(x,y,z)} \Delta V_0(z) - V_0^-(z) \right). \tag{S11}$$

If we assume the junction geometry to be that of a plate capacitor, where the potential drops linearly between the electrodes and therefore $\alpha_0(z) = d/(d+z)$ (for definitions of d, z and z_{tip} see Fig. 2a of the supplement), we finally obtain

$$\Phi^*(x,y,z) = -\frac{d}{d+z} \left(\frac{V^-(x,y,z)}{\Delta V(x,y,z)} \Delta V_0(z) - V_0^-(z) \right) \tag{S12}$$

3.3. A quantitative method to measure local electrostatic potential near surfaces

The review article in this section was published in the Japanese Journal of Applied Physics [67]. The author contributions are as follows: C.W., M.F.B.G., R.T. and F.S.T. conceived the experiments. M.F.B.G. and P.L. performed the experiments. C.W., M.F.B.G. and R.T. analyzed the data. T.D., P.K. and M.R. performed the DFT calculations. M.F.B.G. and R.T. wrote the paper and all authors discussed the manuscript.

Japanese Journal of Applied Physics **55**, 08NA04 (2016)
http://doi.org/10.7567/JJAP.55.08NA04

REVIEW

Scanning quantum dot microscopy: A quantitative method to measure local electrostatic potential near surfaces

Matthew F. B. Green[1,2*], Christian Wagner[1,2], Philipp Leinen[1,2], Thorsten Deilmann[3], Peter Krüger[3], Michael Rohlfing[3], F. Stefan Tautz[1,2], and Ruslan Temirov[1,2]

[1]*Peter Grünberg Institut (PGI-3), Forschungszentrum Jülich, 52425 Jülich, Germany*
[2]*Jülich Aachen Research Alliance (JARA)—Fundamentals of Future Information Technology, 52425 Jülich, Germany*
[3]*Institut für Festkörpertheorie, Westfälische Wilhelms-Universität Münster, 48149 Münster, Germany*

Received January 15, 2016; accepted March 29, 2016; published online July 20, 2016

In this paper we review a recently introduced microscopy technique, scanning quantum dot microscopy (SQDM), which delivers quantitative maps of local electrostatic potential near surfaces in three dimensions. The key to achieving SQDM imaging is the functionalization of a scanning probe microscope tip with a π-conjugated molecule that acts as a gateable QD. Mapping of electrostatic potential with SQDM is performed by gating the QD by the bias voltage applied to the scanning probe microscope junction and registering changes of the QD charge state with frequency-modulated atomic force microscopy.

1. Introduction

Scanning probe microscopy (SPM) has established itself as the premier tool for real-space, nanoscale surface analysis. The early success of scanning tunnelling microscopy (STM)[1,2] was quickly followed by the development of atomic force microscopy, including frequency-modulated AFM (FM-AFM),[3,4] and since then the field has burgeoned, not only in scope of application but also into many different technical variations.[5–12] The beautiful simplicity of the SPM principle makes this possible: as the tip is brought within the close vicinity of the surface, a physical interaction is driven and observed, where the interaction itself determines what information can be extracted from the data. With STM, the best known realization of SPM, the tunnelling current that flows through the sub-nanometre gap between the tip and the surface is used to probe the surface properties. The spatial degrees of freedom introduced by the piezoelectric tip-positioning system of the STM are used to scan the tip over the surface. This then enables the STM to detect the surface topography and electronic structure with sub-Ångström lateral resolution.

Recent years have seen the emergence of new SPM approaches exploiting controlled tip functionalization, where an atom or small molecule is attached to the tip.[13–16] Placing a point-like particle at the apex of the tip introduces additional spatial degrees of freedom into the SPM junction, due to which previously unobservable effects may become accessible.[17–28] Here we review a new SPM-based measurement technique that makes a further step and employs a tip functionalized with a complex, π-conjugated molecule (see Fig. 1). Remarkably, the large molecule attached to the tip in a particular, well-defined configuration displays properties of a gateable quantum dot (QD), thus introducing additional electronic degrees of freedom into the SPM junction. This gives birth to a new imaging method — scanning quantum dot microscopy (SQDM) — that can be used to characterize electrostatic potentials of various surface structures. The capabilities of SQDM have been demonstrated by mapping the electrostatic potential of a perylene tetracarboxylic dianhydride (PTCDA) molecule, and a quantitative measurement of the dipole potential of a single silver adatom, both adsorbed on a Ag(111) surface.[29]

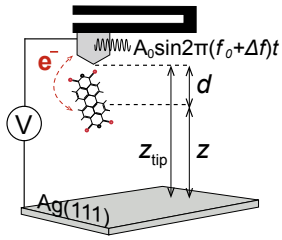

Fig. 1. (Color online) Schematic diagram of the SQDM junction geometry with a large, π-conjugated molecule attached to the SPM tip. With the tuning fork oscillating at an amplitude A_0 at its resonant frequency f_0, bias voltage applied to the sample can induce electron tunnelling events between tip and molecular QD, which can be detected by changes in the resonant frequency Δf. The definitions of d, z, and z_{tip} are displayed.

2. Tip functionalization

Functionalization of the SPM tip with a large organic molecule that facilitates SQDM measurements is achieved by controlled manipulation, in which the molecule is contacted and lifted from the surface with the SPM tip. Until now, three members of the tetracarboxylic dianhydride family: naphthalene-, perylene-, and tetrylene tetracarboxylic dianhydride (N-, P-, and TTCDA) [see Fig. 2(a)] have been shown to provide SQDM functionality when attached to a silver-covered SPM tip. To achieve the silver termination of the tip, the experiments were performed on the Ag(111) surface. Adsorption of PTCDA and NTCDA on Ag(111) has been studied extensively in the past (see Refs. 30–32 and references within). The single-molecule manipulation scheme used to prepare the SQDM tip is also based on previously reported data.[33–39] It proceeds as follows: a qPlus tuning fork atomic force/scanning tunnelling microscope (AFM/STM),[40] operated at 5 K and in ultrahigh vacuum is used to contact a single, isolated molecule. The molecule, adsorbed flat on Ag(111), is approached by the silver-terminated AFM/STM tip directly above one of its corner oxygen atoms [see Figs. 2(a) and 2(b)]. At a tip–oxygen distance of ~3.8 Å, the chosen oxygen atom flips up by ~1.4 Å to establish a chemical bond to the apex of the metal tip.[34] By this oxygen–silver bond, the entire molecule can be lifted from

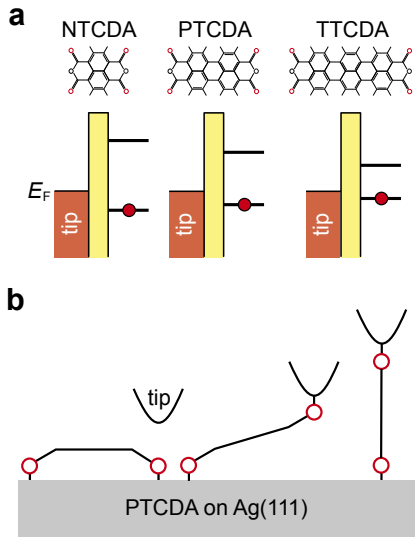

Fig. 2. (Color online) (a) Proposed qualitative level alignment of N-, P-, and TTCDA molecules hanging vertically from the SPM tip. (b) Schematic depiction of the functionalization of the SPM tip with a π-conjugated molecule. The three molecules described adsorb in a buckled geometry due to the interaction between the corner carboxylic oxygen atoms and the silver substrate.[41] By approaching one of these oxygen atoms with a silver-terminated tip, a chemical bond is formed that can then be used to lift the molecule from the surface.

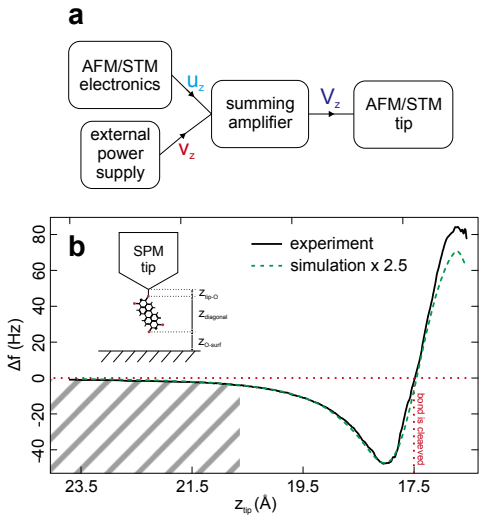

Fig. 3. (Color online) Scheme of SPM electronics, extended by an external power supply, and z-axis calibration method. (a) The voltage output of standard AFM/STM electronics for z-axis control u_z is combined with an externally generated voltage v_z, which are then amplified and applied to the piezo-actuator of the AFM/STM tip. This allows for manual positioning and stabilization of the tip, even when the feedback loop is open. (b) Black curve — fragment of a $\Delta f(z)$ approach curve, recorded on Ag(111) with a PTCDA molecule hanging vertically from the silver-covered SPM tip. The green curve is the result of a force-field simulation obtained for the case of the Au(111) surface and PTCDA attached to a gold-covered SPM tip. The curve is vertically scaled by a factor of 2.5. Differences in the absolute values of $\Delta f(z)$ are explained by the different strength of interaction between the molecule and gold and silver surfaces. The highlighted region indicates the z_{tip} values where stable measurements of the transport feature described in the main text are possible.

the surface into an upstanding configuration, bound via a single Ag–O bond to the tip on one side and the surface on the other side.[34,35] Experiments show that in the majority of cases the tip Ag–O bond has a higher mechanical stability than the Ag–O bond to the surface, which can thus be cleaved by further retraction of the tip from the surface. As the bond between the molecule and the surface is ruptured, the attractive interaction with the surface aligns the molecule into a configuration perpendicular to the surface,[37,39] in which the molecule hangs from the tip by its oxygen–silver bond as shown in Fig. 1. This configuration has been supported by experiments and force-field simulations,[37,39] together with, as will be seen later, the QD behaviour of the molecule attached to the tip, since any overlap of the molecular π electron system with the metal tip's electronic states would destroy these properties.

In order to keep the molecule stable on the SPM tip the current feedback loop is kept open over the whole course of SQDM experiments. By manually applying voltage to the piezo-actuators with an external power supply [see Fig. 3(a)], the molecule suspended from the tip can be stabilized at any chosen tip–sample separation,[42] where SQDM measurements can subsequently be performed. This then demands a careful z-axis calibration, which is performed according to Ref. 39: a frequency shift $\Delta f(z)$ approach curve measured above the silver substrate with the molecule suspended from the tip [see Fig. 3(b)] is compared with a $\Delta f(z)$ curve obtained from a force-field simulation. The point where $\Delta f(z)$ crosses zero, corresponding to the maximum attractive force between tip and sample, is attributed to the cleavage of the last bond between the molecule and the surface. Simulations show that the cleavage of this bond occurs in a geometry where the diagonal of the molecule is perpendicular to the surface. Since the size of the molecule is well known, the tip–surface distance z_{tip} can be deduced according to the following expression: $z_{tip} = z_{tip-O} + z_{diagonal} + z_{O-surf}$, where $z_{tip-O} = 2.2$ Å is the length of the oxygen–metal bond that binds the molecule to the tip and $z_{diagonal} = 12.4$ Å is the diagonal length of the molecule [see the inset of Fig. 3(b)].[37,39] By aligning the simulation to the experimental curve, it is found that $z_{O-surf} = 2.9 \pm 0.5$ Å at the point of cleavage, with the estimated uncertainty stemming from the fact that the simulation was performed on a Au(111) substrate.

3. Single molecule as a QD

QD properties of the molecule hanging from the silver-covered tip were revealed with transport measurements. This was done by bringing the molecule into tunnelling contact a few ångströms above the surface, as shown in the inset of Fig. 3(b). The tip–surface distance was set such that the maximum current flowing through the tip–molecule-surface junction during the transport measurement never exceeded ~20 pA, as it was found that the molecule's adsorption geometry on the tip was unstable to larger currents. The necessary junction geometry was recognized by a negative frequency shift of several Hertz in the absence of a

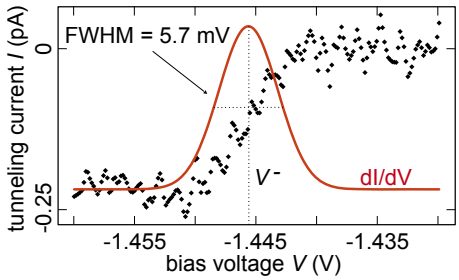

Fig. 4. (Color online) Transport spectrum taken with a PTCDA QD without tuning fork oscillation. The differential conductance is obtained by smoothing and numerically differentiating the tunnelling current spectrum. Taking the thermal broadening of the tip's Fermi energy and the voltage drop in the junction into account, the upper limit of the energy level linewidth Γ is 0.9 meV. V^- refers to the bias voltage at which the QD loses a single electron into the tip.

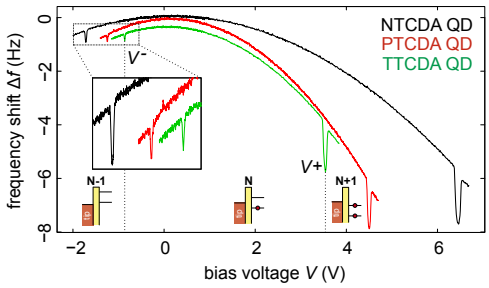

Fig. 5. (Color online) SQDM with a molecular QD and an AFM. Δf spectra recorded with three different QDs, all at $z_{tip} = 38$ Å. The sharp dips in resonant frequency shift where the charge state of the molecular QD is changed are referred to as V^- and V^+. The effect of orbital size and therefore on-site Coulomb repulsion on energy level spacing is reflected in the different $\Delta V = V^+ - V^-$ values for the different molecules. The level occupation diagrams are shown for the case of a TTCDA QD.

measurable tunnelling current at low bias (~10–20 mV). Inspection of Fig. 3(b) suggests that the transport was measured in an asymmetric configuration with the coupling to the tip stronger than the coupling to the surface since $z_{tip-O} = 2.2$ Å and $z_{O-surf} \approx 5$–10 Å.

The transport measurement was performed with tuning fork oscillation deactivated by sweeping the bias voltage applied to the sample. The measurement revealed a feature displayed in Fig. 4: a sharp, sudden step in current, i.e., a narrow peak in the differential conductance. This feature is reminiscent of transport through QDs, which occurs when the applied bias window spans over one of the QD's electronic levels.[43,44] Since in this case negative bias corresponds to the tip being at a positive potential with respect to the surface, the transport feature is interpreted as tunnelling of an electron from the QD into the tip, followed by the tunnelling of an electron from the surface into the QD. The width of the transport feature is thus defined by the hybridization Γ of the QD state with the states of the tip and the thermal broadening of the tip's Fermi energy, equal to $3.52k_BT$ at 5 K. More precisely, a convolution of a Cauchy–Lorentz distribution, with full width at half maximum (FWHM) $= 2\Gamma$, with the derivative of the Fermi–Dirac distribution $f(E)$, describes the experimental lineshape:[45]

$$\frac{dI}{dV}(E) \propto \int_{-\infty}^{\infty} \frac{df}{dE}(E') \frac{\Gamma}{\pi[(E'-E)^2 + \Gamma^2]}\, dE'. \quad (1)$$

Since z_{O-surf} is significantly larger than z_{tip-O}, the hybridization of the QD state with the states in the sample surface is negligible. Additionally, the voltage drop in the junction needs to be taken into account. We introduce α, the "lever arm", as the ratio between the voltage that drops over the tip–molecule bond and the total bias applied to the sample, and in the limiting case of a symmetric junction, $\alpha = 0.5$. To account for α, Eq. (1) is modified to

$$\frac{dI}{dV}(E) \propto \int_{-\infty}^{\infty} \alpha \frac{df}{dE}(\alpha E') \frac{\alpha\Gamma}{\pi[(\alpha E'-E)^2 + \alpha\Gamma^2]}\, dE'. \quad (2)$$

By comparing the expected FWHM from Eq. (2) in the limit of $\alpha = 0.5$ with the experimental FWHM, an upper limit for Γ is obtained: $\Gamma_{\alpha=0.5} = 0.9$ meV. Note that in reality $\alpha < 0.5$ and therefore $\Gamma < 0.9$ meV. This narrow energy linewidth despite the strong chemical bond between molecule and tip is unexpected. More studies are needed to understand this effect in detail. At this moment it might be rationalized by the following arguments: the molecular frontier orbitals have π character with small amplitude at the corner oxygen atoms, and furthermore the orbital lobes extend perpendicularly to the tip–molecule bond, minimizing the overlap with the tip.

The transport-based detection of QD charging discussed above is impractical, mainly since the distance range where detection is possible is very narrow, defined both by the limited stability of the QD's adsorption geometry on the tip and the short distance scale of the tunnelling regime. An FM-AFM-based detection mode proves to be more convenient.[46] There the distance between QD and surface can be far larger than a typical tunnelling gap, so electrons can only enter and leave the molecular QD tunnelling through the tip–QD bond [see Fig. 1(a)]. In the following this detection mode is explained. With tuning fork oscillation activated, the bias voltage is swept and the shift in the tuning fork's resonant frequency Δf is monitored, recording a $\Delta f(V)$ curve with the familiar parabolic shape (see Fig. 5), where the parabolic nature of the curve stems from the electrostatic interaction between the two macroscopic electrodes — the tip and the sample.[47,48]

Charging the molecular QD results in sudden changes of the tip–sample force that are detected by the FM-AFM as sharp dips in the parabolic $\Delta f(V)$ curve.[45,46,49] Denoting the QD charge state at $V = 0$ V as N, two dips observed at positive and negative bias in Fig. 5 are attributed to the transitions between QD states N, $N-1$ and $N+1$, effected by the gating of the QD energy levels through the Fermi level of the tip (see Refs. 50, 51 and references within).

In comparison to a conventional QD the charging features of this molecular QD demonstrate two interesting differences. First of all it is apparent that particle–hole symmetry is broken since $|V^-| < |V^+|$, where V^- (V^+) is the voltage at which the transition from N to $N-1$ (N to $N+1$) state occurs. This asymmetry points towards the existence of a dipolar potential at the tip–molecule bond. The orientation of this dipole is such that its negative end points towards the molecule, thus creating an additional energy barrier for an electron moving from the tip to the QD, while providing an

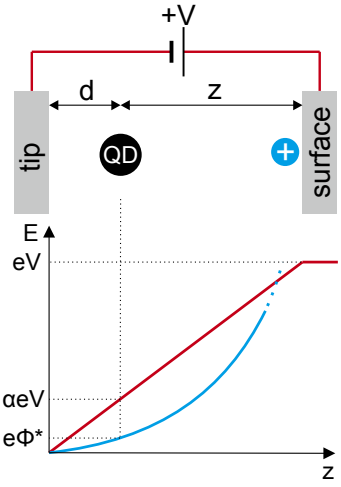

Fig. 6. (Color online) Above: schematic display of the SQDM junction. Below: the electrostatic potential energy for a positive test charge in the junction at an applied bias voltage V. If the tip and surface electrodes are assumed to form a parallel plate capacitor, the voltage drops linearly in the junction. The potential of any local charge distribution decays with distance away from the surface and is detected at the position of the QD (Φ^*). Here the QD is assumed to be a point particle at a distance d from the tip.

energy gain for a hole moving in the same direction. Another interesting feature of the molecular QD is its on-site Coulomb repulsion energy U, which is expected to be significantly larger than that of a larger (e.g., semiconductor) QD.[46] Figure 5 shows that $\Delta V \equiv V^+ - V^- \sim \alpha^{-1}U$ scales inversely with the size of the molecular QD, as to be expected [see Fig. 2(a)].

4. Qualitative mapping of electrostatic potential with SQDM

In order to explain how electric potential is mapped with SQDM, a simple model can be considered. First, the energies of the QD in its different charge states are written down:

$$E(N) \equiv 0, \tag{3}$$

$$E(N-1) = E_{\text{hole}} + \alpha eV + e\Phi^*, \tag{4}$$

$$E(N+1) = E_{\text{el}} - \alpha eV - e\Phi^*, \tag{5}$$

where E_{hole} (E_{el}) is the energy required to add a hole (electron) to the QD in charge state N at zero bias voltage. As has been discussed above E_{hole} and E_{el} are defined by the size of QD and the properties of the tip–molecule bond. $+\alpha eV$ ($-\alpha eV$) is the energy of a hole (electron) in the QD due to the bias voltage applied to the junction (see Fig. 6). Finally, $+e\Phi^*$ ($-e\Phi^*$) is the energy of a hole (electron) in the QD due to the electrostatic potential of a charged structure located on the surface. Φ^* is simply the electrostatic potential of that structure evaluated at the position of the QD in the presence of the SPM tip. Note that the true electrostatic potential of the structure Φ in the absence of the SPM tip will be higher due to the screening properties of the bulk metal tip. Thus for a qualitative picture of the electrostatic potential of a nanostructure it is enough to map the variations of Φ^* along the surface, but for quantitative measurements the potential Φ must be evaluated.

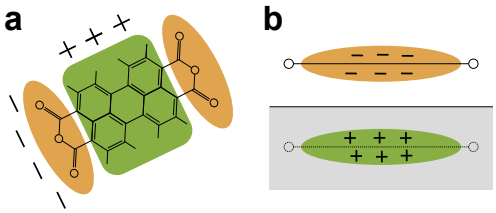

Fig. 7. (Color online) (a) Top view: quadrupolar charge distribution formed by the partial charges of PTCDA, originating from its functional groups. (b) Side view: dipole moment due to the net charge transfer to PTCDA from the Ag(111) surface and the consequently formed image charge distribution in the surface.

Qualitative images of Φ^* are obtained by noting that the QD charge state transitions occur when $E(N) = E(N+1) = 0$ or $E(N) = E(N-1) = 0$. For these conditions a system of linear equations is obtained:

$$E_{\text{hole}} + \alpha eV^- + e\Phi^* = 0, \tag{6}$$

$$E_{\text{el}} - \alpha eV^+ - e\Phi^* = 0. \tag{7}$$

Solving Eqs. (6) and (7) with respect to Φ^*, the following expression is obtained:

$$\Phi^* = -\frac{V^-}{e\Delta V}(E_{\text{hole}} + E_{\text{el}}) - \frac{E_{\text{hole}}}{e}, \tag{8}$$

where $\Delta V \equiv V^+ - V^-$. The expression shows that Φ^* is proportional to the measurable quantity $V^-/\Delta V$. Extracting $V^-/\Delta V$ from experimental spectra like those shown in Fig. 5 measured at different locations over the surface therefore reveals a qualitative map of electrostatic potential.

The ability of SQDM to deliver qualitative maps of Φ^* was demonstrated by imaging the potential of a single PTCDA molecule. Note that the single PTCDA molecule adsorbed flat on the Ag(111) surface was imaged by using another PTCDA molecule hanging on the tip, acting as the QD. The measurement was performed in the form of grid spectroscopy where at every (x, y) coordinate in a grid, at a certain z_{tip}, a single $\Delta f(V)$ spectrum was acquired. From each $\Delta f(V)$ spectrum the values of V^+ and V^- were obtained and consequently the quantity $V^-/\Delta V$ was plotted on the same (x, y) grid.

The electrostatic potential of PTCDA on Ag(111) is expected to have two major components shown in Fig. 7: a quadrupole due to the negatively polarized oxygen atoms and a positively polarized perylene backbone as well as a dipolar contribution stemming from a weak net charge transfer between Ag(111) and PTCDA.[52] The quantity $V^-/\Delta V$ plotted in Figs. 8(a)–8(c) is dominated by the quadrupole potential at $z_{\text{tip}} = 24$ Å and the dipole potential at $z_{\text{tip}} = 36$ Å; to be expected since the quadrupole component decays faster with distance from the surface.

The images of experimentally mapped potentials are corroborated by a comparison to the results of a micro-electrostatic simulation [shown in Figs. 8(d)–8(f)], in which the internal charge distribution of a gas-phase PTCDA molecule, as calculated by density functional theory (DFT), its screening by the image charges located inside the metal surface, and a homogeneous charge transfer from the surface into the molecule were taken into account. The simulated images in Figs. 8(d)–8(f) were obtained by fitting the charge

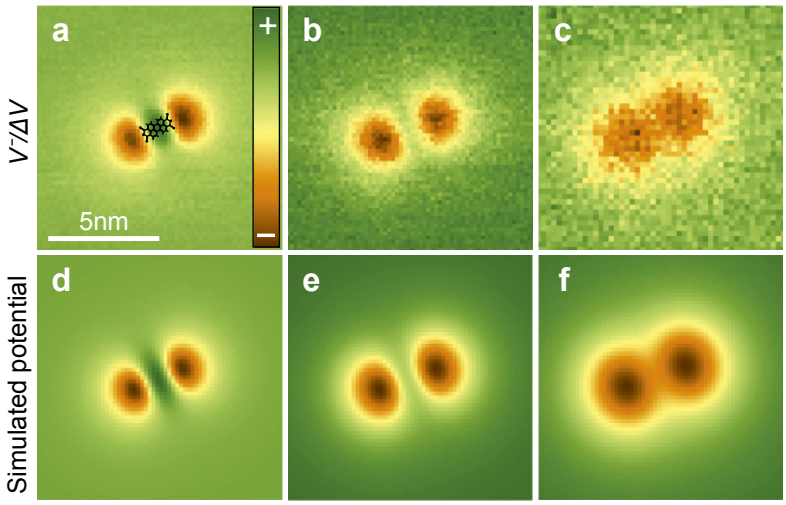

Fig. 8. (Color online) Potential of a single, surface-adsorbed molecule (adapted from Ref. 29). (a–c) The quantity $V^-/\Delta V$, proportional to electric potential, is plotted above a single PTCDA molecule. A 5 nm scale bar is shown; this applies to all images. Image (a) was measured at $z_{tip} = 24$ Å, (b) at 28 Å, and (c) at 36 Å. (d–f) Results of electrostatic simulations as described in the text with $z = 16$ Å (d), 22 Å (e), and 28 Å (f).

transfer from Ag(111) to PTCDA ($q \simeq -0.1e$) and the distance z from the surface at which the simulated potential is plotted.[53] Remarkably, comparing the obtained distances $z = 16$, 22, and 28 Å of Figs. 8(d)–8(f) with the experimental $z_{tip} = 24$, 28, and 36 Å of Figs. 8(a)–8(c), an estimate for d was obtained: $d = \overline{z_{tip}} - \overline{z} = (7 \pm 1)$ Å. This shows that the electrostatic potential is probed at a point approximately 7 Å below the tip apex, hence at the position of the PTCDA QD, as expected from the proposed junction geometry shown in Fig. 1(a).

5. Quantitative measurements of electrostatic potential with SQDM

Returning to the expression given for Φ^* [Eq. (8)], one notes that it contains constants E_{hole} and E_{el} that are however unknown. For quantitative determination of the potential these constants must be eliminated from the formula. This is done by performing a calibration measurement at a position above the clean Ag(111) surface where $\Phi^* = 0$. According to Eqs. (6) and (7) obtained above, $E_{hole} = -\alpha_0 e V_0^-$ and $E_{el} = \alpha_0 e V_0^+$, where α_0, V_0^-, V_0^+ are the values of α, V^-, V^+ above clean Ag(111). This results in a quantitative expression for Φ^*:

$$\Phi^*(x,y,z) = -\alpha_0(z)\left[\frac{V^-(x,y,z)}{\Delta V(x,y,z)}\Delta V_0(z) - V_0^-(z)\right]. \quad (9)$$

Note that to obtain Φ^* at a particular distance from the surface z the calibration values V_0^-, V_0^+ have to be measured at the same z, while $\alpha_0(z)$ can be crudely approximated by the expression $d/(z+d)$, valid for the case of a parallel plate capacitor.

To demonstrate a quantitative SQDM measurement the Smoluchowski dipole potential of a single silver adatom on Ag(111) was characterized. The effect stems from the incomplete screening of the atomic nucleus by the delocalized surface electrons, leading to the formation of a charge dipole, with its positive pole pointing away from the surface.[54] The adatom was produced by gently indenting the clean Ag-terminated tip into the surface.[55] Grid $\Delta f(V)$ spectroscopy was performed above an Ag adatom on the Ag(111) surface at three different tip–surface distances $z_{tip} = 28$, 36, and 44 Å. Calibration measurements of V_0^- and V_0^+ were performed at the same set of three z_{tip} values over clean Ag(111) at a lateral distance of ~100 Å away from the adatom. Φ^* was then obtained from Eq. (9). Finally, the value of the Smoluchowski dipole potential in the absence of the tip Φ was determined by approximating the screening effect of the tip by the presence of an image potential Φ_{image}, with its origin in the bulk of the tip electrode. The measured Φ^* is thus a sum of Φ and Φ_{image}. The screening ratio Φ^*/Φ was determined for the model of a single point charge as well as for a single point dipole in front of an infinite metal surface, an approximation for the tip. The two values of Φ determined in this way, $\Phi_{point\ charge}$ and Φ_{dipole} respectively, are plotted in Fig. 9(d). Although for the precise treatment of the tip influence an infinite series of image potentials from the tip and the sample needs to be taken into account, the correction to the potential that this provides is significantly smaller than the uncertainty in Φ itself.

The obtained maps of Φ_{dipole} are shown in Figs. 9(a)–9(c). Evaluating the maximum of Φ_{dipole} at every measured $z = z_{tip} - d$ [see Fig. 1(a)], the distance dependence $\Phi_{dipole}(z)$ is obtained [see Fig. 9(d)]. $\Phi_{dipole}(z)$ shows excellent agreement to the expected $1/z^2$ decay rate for a dipole potential. Quantitatively, values of Φ_{dipole} come at about 60% of the result of a DFT calculation. This degree of correspondence is outstanding, taking into account the crudeness of the plate capacitor approximation used in determining $\alpha_0(z)$ (see above). Note that the good agreement between $\Phi_{point\ charge}$ and the DFT values is most likely a cancellation of errors, since the dipole model provides a more realistic picture of the actual screening strength.

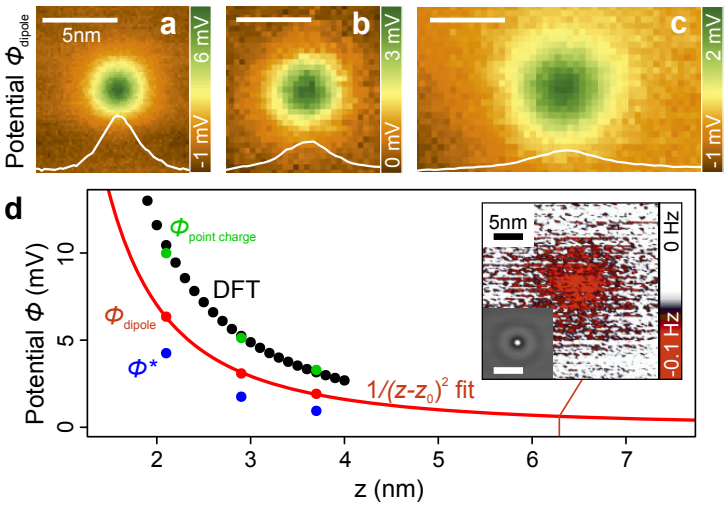

Fig. 9. (Color online) Smoluchowski dipole of a single adatom (reproduced from Ref. 29). (a–c) Potential Φ_{dipole} of Ag adatom on the Ag(111) surface, with the screening effect of the tip accounted for (cf. text), recorded with grid spectroscopy using a PTCDA QD. 5 nm scale bars are again shown and line profiles through the atom are shown in white. Maps recorded at $z = 21$, 29, and 37 Å, respectively. (d) Comparison of the experimental Φ^* (blue), Φ_{dipole} (red), $\Phi_{point\ charge}$ (green) and DFT-calculated (black) potentials vertically above the adatom (for definitions of Φ, Φ^* see text). The red line shows a $1/(z - z_0)^2$ fit of the experimental data, where $z_0 = 1.68$ Å was obtained by fitting the DFT dataset. For the definition of the z scale see the main text. For the DFT results, z is the distance from the surface at which the potential of the adatom was calculated; for details on the DFT calculations see Ref. 29. (Inset) Constant height raw Δf image recorded at $z = 6.3$ nm with an applied bias of $V = 9.6$ V (close to V^+). (Bottom left corner) STM image of the adatom.

6. Constant height SQDM imaging

The high sensitivity of SQDM, originating in the fact that it uses sharp charging transitions of the QD to measure electrostatic potential, helps in locating small surface features quickly and without bringing the tip, functionalized with a molecular QD, too close to the surface. Fast SQDM imaging is done by recording Δf while scanning the surface at constant height with the sample bias set close to either V^+ or V^-. As was explained above, every topographic feature or a perturbation of the surface electrostatic potential shifts V^+ and V^- and therefore creates a contrast in the Δf constant height scan.[29] In the inset of Fig. 9(d), the presence of an adatom is detected by a constant height Δf scan recorded at $z = 6.3$ nm and $V = 9.6$ V.

7. Summary and outlook

In conclusion, we have reviewed the recently developed microscopy technique SQDM which delivers quantitative maps of electrostatic potential in 3D with sub-nanometre resolution. SQDM functionality stems from the introduction of additional electronic and spatial degrees of freedom into the junction, which appear as a result of functionalizing the tip with a nanometre-sized molecular QD.[29] The combination of quantitative, 3D measurement capability and high sensitivity for electrostatic potential measurements makes SQDM a promising new technique for surface analysis. The properties of SQDM could make it suitable for the characterization of samples with larger surface roughness, thus possibly expanding the scope of application beyond that of conventional scanning probe techniques. Importantly, the concept of SQDM is not limited to the molecular realization of a QD discussed here. One could envision SQDM sensors with other types of QDs (e.g., small metal clusters or silicon micro-fabricated QDs), possibly on standard silicon AFM cantilevers. Compared with a molecular SQDM sensor, sensors of this kind could bring the technique beyond the confines of ultrahigh vacuum and cryogenic temperatures. They could also prove to be more robust and help to bring new insights to the studies of chemically complex surfaces and interfaces in chemistry, biology and nanoelectronics.

1) D. M. Eigler and E. K. Schweizer, Nature **344**, 524 (1990).
2) M. F. Crommie, C. P. Lutz, and D. M. Eigler, Nature **363**, 524 (1993).
3) T. R. Albrecht, P. Grütter, D. Horne, and D. Rugar, J. Appl. Phys. **69**, 668 (1991).
4) F. J. Giessibl, Science **267**, 68 (1995).
5) R. Wiesendanger, H.-J. Güntherodt, G. Güntherodt, R. J. Gambino, and R. Ruf, Phys. Rev. Lett. **65**, 247 (1990).
6) M. Nonnenmacher, M. P. O'Boyle, and H. K. Wickramasinghe, Appl. Phys. Lett. **58**, 2921 (1991).
7) R. Berndt, J. K. Gimzewski, and P. Johansson, Phys. Rev. Lett. **67**, 3796 (1991).
8) B. C. Stipe, M. A. Rezaei, and W. Ho, Science **280**, 1732 (1998).
9) M. T. Woodside and P. L. McEuen, Science **296**, 1098 (2002).
10) U. Kaiser, A. Schwarz, and R. Wiesendanger, Nature **446**, 522 (2007).
11) S. Loth, M. Etzkorn, C. P. Lutz, D. M. Eigler, and A. J. Heinrich, Science **329**, 1628 (2010).
12) E. Inami and Y. Sugimoto, Phys. Rev. Lett. **114**, 246102 (2015).
13) L. Bartels, G. Meyer, and K. Rieder, Appl. Phys. Lett. **71**, 213 (1997).
14) R. Temirov, S. Soubatch, O. Neucheva, A. C. Lassise, and F. S. Tautz, New J. Phys. **10**, 053012 (2008).
15) L. Gross, F. Mohn, N. Moll, P. Liljeroth, and G. Meyer, Science **325**, 1110 (2009).
16) G. Kichin, C. Weiss, C. Wagner, F. S. Tautz, and R. Temirov, J. Am. Chem. Soc. **133**, 16847 (2011).
17) C. Weiss, C. Wagner, R. Temirov, and F. S. Tautz, J. Am. Chem. Soc. **132**, 11864 (2010).
18) F. Mohn, L. Gross, N. Moll, and G. Meyer, Nat. Nanotechnol. **7**, 227 (2012).
19) L. Gross, F. Mohn, N. Moll, B. Schuler, A. Criado, E. Guitián, D. Peña, A.

Gourdon, and G. Meyer, Science **337**, 1326 (2012).
20) J. Zhang, P. Chen, B. Yuan, W. Ji, Z. Cheng, and X. Qiu, Science **342**, 611 (2013).
21) G. Kichin, C. Wagner, F. S. Tautz, and R. Temirov, Phys. Rev. B **87**, 081408 (2013).
22) J. Guo, X. Meng, J. Chen, J. Peng, J. Sheng, X.-Z. Li, L. Xu, J.-R. Shi, E. Wang, and Y. Jiang, Nat. Mater. **13**, 184 (2014).
23) C.-l. Chiang, C. Xu, Z. Han, and W. Ho, Science **344**, 885 (2014).
24) P. Hapala, G. Kichin, C. Wagner, F. S. Tautz, R. Temirov, and P. Jelínek, Phys. Rev. B **90**, 085421 (2014).
25) P. Hapala, R. Temirov, F. S. Tautz, and P. Jelínek, Phys. Rev. Lett. **113**, 226101 (2014).
26) S. K. Hämäläinen, N. van der Heijden, J. van der Lit, S. D. Hartog, P. Liljeroth, and I. Swart, Phys. Rev. Lett. **113**, 186102 (2014).
27) R. Temirov and F. S. Tautz, in *Noncontact Atomic Force Microscopy*, ed. S. Morita, F. Giessibl, E. Meyer, and R. Wiesendanger (Springer, Heidelberg, 2015) Vol. 3, Chap. 14.
28) C. Wagner and R. Temirov, Prog. Surf. Sci. **90**, 194 (2015).
29) C. Wagner, M. F. B. Green, P. Leinen, T. Deilmann, P. Krüger, M. Rohlfing, R. Temirov, and F. S. Tautz, Phys. Rev. Lett. **115**, 026101 (2015).
30) A. Schöll, Y. Zou, T. Schmidt, R. Fink, and E. Umbach, J. Phys. Chem. B **108**, 14741 (2004).
31) C. Stadler, S. Hansen, A. Schöll, T. L. Lee, J. Zegenhagen, C. Kumpf, and E. Umbach, New J. Phys. **9**, 50 (2007).
32) M. Rohlfing, R. Temirov, and F. S. Tautz, Phys. Rev. B **76**, 115421 (2007).
33) R. Temirov, A. Lassise, F. B. Anders, and F. S. Tautz, Nanotechnology **19**, 065401 (2008).
34) C. Toher, R. Temirov, A. Greuling, F. Pump, M. Kaczmarski, G. Cuniberti, M. Rohlfing, and F. S. Tautz, Phys. Rev. B **83**, 155402 (2011).
35) N. Fournier, C. Wagner, C. Weiss, R. Temirov, and F. S. Tautz, Phys. Rev. B **84**, 035435 (2011).
36) A. Greuling, M. Rohlfing, R. Temirov, F. S. Tautz, and F. B. Anders, Phys. Rev. B **84**, 125413 (2011).
37) C. Wagner, N. Fournier, F. S. Tautz, and R. Temirov, Phys. Rev. Lett. **109**, 076102 (2012).
38) A. Greuling, R. Temirov, B. Lechtenberg, F. B. Anders, M. Rohlfing, and F. S. Tautz, Phys. Status Solidi B **250**, 2386 (2013).
39) C. Wagner, N. Fournier, V. G. Ruiz, C. Li, K. Müllen, M. Rohlfing, A. Tkatchenko, R. Temirov, and F. S. Tautz, Nat. Commun. **5**, 5568 (2014).
40) F. Giessibl, Rev. Mod. Phys. **75**, 949 (2003).
41) A. Hauschild, K. Karki, B. C. C. Cowie, M. Rohlfing, F. S. Tautz, and M. Sokolowski, Phys. Rev. Lett. **94**, 036106 (2005).
42) M. F. B. Green, T. Esat, C. Wagner, P. Leinen, A. Grötsch, F. S. Tautz, and R. Temirov, Beilstein J. Nanotechnol. **5**, 1926 (2014).
43) P. L. McEuen, E. B. Foxman, U. Meirav, M. A. Kastner, Y. Meir, N. S. Wingreen, and S. J. Wind, Phys. Rev. Lett. **66**, 1926 (1991).
44) H. van Houten, C. W. J. Beenakker, and A. A. M. Staring, in *Single Charge Tunneling: Coulomb Blockade Phenomena in Nanostructures*, ed. H. Grabert and M. H. Devoret (Springer, Heidelberg, 1992) Chap. 5.
45) N. Kocić, P. Weiderer, S. Keller, S. Decurtins, S.-X. Liu, and J. Repp, Nano Lett. **15**, 4406 (2015).
46) R. Stomp, Y. Miyahara, S. Schaer, Q. Sun, H. Guo, P. Grutter, S. Studenikin, P. Poole, and A. Sachrajda, Phys. Rev. Lett. **94**, 056802 (2005).
47) S. Kitamura, K. Suzuki, and M. Iwatsuki, Appl. Surf. Sci. **140**, 265 (1999).
48) M. Guggisberg, M. Bammerlin, C. Loppacher, O. Pfeiffer, A. Abdurixit, V. Barwich, R. Bennewitz, A. Baratoff, E. Meyer, and H.-J. Güntherodt, Phys. Rev. B **61**, 11151 (2000).
49) C. Lotze, Dr. Thesis, Department of Physics, Freie Universität Berlin, Berlin (2013).
50) Y. Azuma, M. Kanehara, T. Teranishi, and Y. Majima, Phys. Rev. Lett. **96**, 016108 (2006).
51) L. Cockins, Y. Miyahara, S. D. Bennett, A. A. Clerk, S. Studenikin, P. Poole, A. Sachrajda, and P. Grutter, Proc. Natl. Acad. Sci. U.S.A. **107**, 9496 (2010).
52) Y. Zou, L. Kilian, A. Schöll, T. Schmidt, R. Fink, and E. Umbach, Surf. Sci. **600**, 1240 (2006).
53) Although the LUMO of PTCDA receives a charge of $-1.8e$ upon adsorption on Ag(111), backdonation from the lower lying orbitals results in a smaller net charge transfer to the molecule.[32)]
54) R. Smoluchowski, Phys. Rev. **60**, 661 (1941).
55) L. Limot, J. Kröger, R. Berndt, A. Garcia-Lekue, and W. A. Hofer, Phys. Rev. Lett. **94**, 126102 (2005).

4

Quantitative modelling of single electron charging events

Introduction

Single electron charging is a fundamental physical phenomenon involving by definition the transfer of the smallest possible quantity of electronic information. Harnessing control over individual electrons is of great importance for next-generation electronics, where quantum dots [68–70], single molecules [13, 14, 71–73] or single atoms [74–77] may form the building blocks for functional design. While it seems natural to employ tunnelling methods for the detection of single electron charging events, force microscopy has in fact emerged as the most versatile and sensitive method for this purpose [78–82], where the force, frequency shift or energy dissipation can make up the output signal. With respect to this thesis, as seen in previous chapters, single electron charging events also form the basis of SQDM.

A prerequisite for the observation of single electron charging of an object is the *Coulomb blockade*, the regime that constrains electronic charging events to occur sequentially, separated by an energy barrier. This occurs due to the Coulombic repulsion of individual electrons — when a single electron enters the object, the next electron has to overcome this repulsion energy before it can enter. In this chapter we introduce the *single electron box model*, an example of the orthodox theory of the Coulomb blockade [70, 83, 84], and apply this to our experimental system. The realization of the Coulomb blockade discussed here is the SQDM tip, introduced in the previous chapters. The single electron box model is then applied to the experimental data and discussed.

Next, the *point charge model*, introduced in the previous chapters, is developed further and used to extract the energy level positions and intramolecular Coulomb repulsion energy of the QD from experimental data. The accuracy of this simple and intuitive model is proved by a comparison to the single electron box model, where the two models are shown to be equivalent in their predictions of the charging features. Moreover, the breakdown of the models as applied to our experiments is revealed and discussed. This result is of significant interest for future investigations of single electron charging, especially for objects with small spatial dimensions.

4.1. Single electron box model

In order to model the single electron charging features in our system, we begin this chapter by explaining the principle of the single electron box (SEB). Due to the Coulomb blockade the SEB is populated by an integer multiple of electronic charge, and the charge state of the SEB can be modified by gating. There is an extensive body of literature on this topic (see Refs. [26, 70, 79, 83–88], references within and citing articles), however we will provide a comprehensive introduction such that the reader grasps the key concepts from this text alone.

An example of a single electron box is a QD situated between two electrodes, with a tunnelling barrier on one side and a vacuum gap on the other side between the QD and the so-called gate electrode. This geometry is depicted in Fig. 4.1(a), where in this case the AFM tip forms the tunnelling electrode and the sample surface the gate electrode. The capacitance between the QD and the tip is referred to as

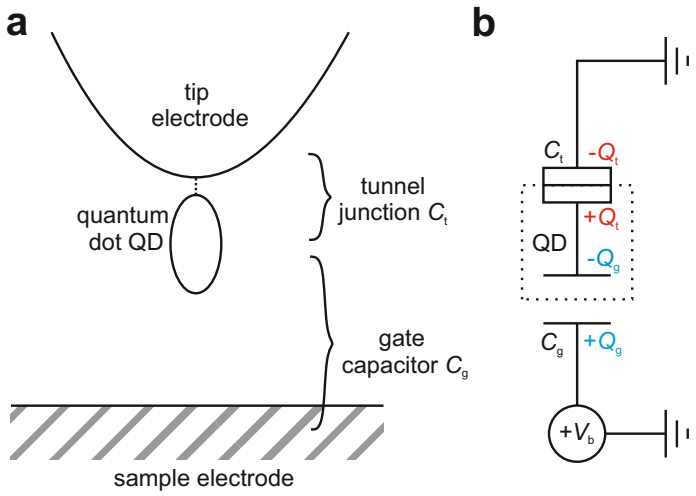

Figure 4.1: (a) Schematic diagram of the tip-QD-sample junction. The QD is attached to the tip via a tunnel barrier with a capacitance C_t, across which electrons can tunnel to and from the QD. The QD interacts (no electronic tunnelling) with the sample via the gate capacitor with capacitance C_g. (b) Circuit diagram of (a). Bias voltage V_b is applied to the sample and polarization charges $Q_{t,g}$ build up on the capacitors due to the rearrangement of charge carriers in the electrodes.

C_t and between the QD and the surface as C_g. There is a residual capacitance between the macroscopic tip and sample electrodes, however this is not relevant to the results in this chapter and we will not discuss it. Note that in this chapter, unless otherwise explicitly stated, we will exclusively discuss the regime where the distance between the gate capacitor plates is large enough such that quantum tunnelling is only possible between the QD and the tip electrode.

Observing the Coulomb blockade

In order to observe Coulomb blockade phenomena in experiment, several conditions must be fulfilled. For the following description we will utilize three representative quantities: (1) a total capacitance C_Σ between the QD and its environment, and the energy required to charge the QD with an electron, e^2/C_Σ, where $e = 1.602 \cdot 10^{-19}$ C is the electronic charge; (2) the difference in energy between two neighbouring quantum states of the QD, ΔE; (3) the thermal energy of the system in equilibrium, $k_B T$. There are in general three possible energy regimes:

1. $k_B T \gg e^2/C_\Sigma$. In this case thermal fluctuations are large enough to charge or discharge the QD and no Coulomb blockade phenomena will be observed. Since all experiments were conducted at 5 K the condition can be written as $C_\Sigma \gg 10^{-16}$ F, while for our QD, $\sim$1 nm in size, the total capacitance is expected to be significantly smaller [89].

2. $e^2/C_\Sigma \gg k_B T \gg \Delta E$. This is known as the *classical limit* of the Coulomb blockade: single electron charging events can be controllably induced, however ΔE is negligible and thermal fluctuations cause many energy levels to be excited.

3. $e^2/C_\Sigma, \Delta E \gg k_B T$. In the *quantum limit* of the Coulomb blockade the QD's single particle energy levels are sequentially populated.

The spacing of our molecular QD's energy levels means that we are certainly in the quantum limit where only one energy level is accessible for the tunnelling electron. In addition, to be able to consider the charge on the QD as an integer multiple of e, the tunnelling resistance between tip and QD must be much greater than the

resistance quantum, i.e. $R_{\mathrm{tun}} \gg h/e^2 \simeq 25.8\ \mathrm{k}\Omega$. This ensures that electrons from the tip electrode have vanishing probability of being on the QD. A very large resistance is equivalent to a very small wave function overlap between the levels of the QD and electronic states in the tip and so the condition can also be expressed as a weak electronic coupling Γ between tip and QD.

4.1.1. Experimental data

Before we apply the SEB model to our QD attached to the AFM tip, we present experimental data in order to gain qualitative understanding of several key points. From simple electrostatics it follows that a change in the charge state of the QD will lead to a modified electrostatic interaction between tip and sample. The interaction of a single electron with the electric field in the tip-sample junction is minimal (fN–pN [78, 79]) compared to the long range forces in the experiment, of which the main contributions at nanometre tip height are the electrostatic and van der Waals interactions between the macroscopic tip and sample electrodes ($>$ nN [34]). However the change in force upon charging occurs over a distance on the order of ~ 0.1 nm, while the electrostatic background forces vary much more slowly. Since FM-AFM is sensitive to the spatial gradient of the force between tip and sample, it is an excellent technique for detecting the charging events. The change in electrostatic force between tip and sample when the QD's charge state is changed therefore forms the basis of our signal.

We have access to two independent parameters that can shift the energy levels of the QD with respect to the electrodes: the bias voltage V_{b} and the tip-sample distance z (defined in the inset of Fig. 4.2(b) and denoted as z_{tip} in the previous chapter). Applying bias voltage to the surface results in a voltage drop between the tip and QD, shifting the QD's levels with respect to the Fermi level of the tip (see Chap. 3). By varying V_{b} while holding z constant, the charging events of the QD can be detected in the frequency shift output, i.e. in a $\Delta f(V_{\mathrm{b}},\ z = c)$ spectrum, where c is a constant.

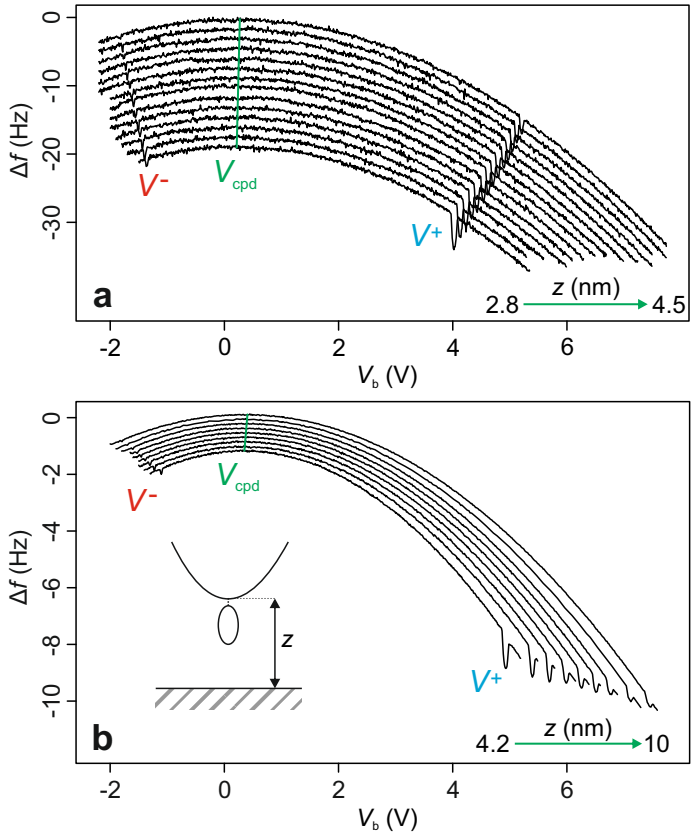

Figure 4.2: Single electron charging events measured by $\Delta f(V_\mathrm{b},\ z = c)$ spectroscopy. (a) and (b) display two separate datasets, spectra close to the surface (a) and far from the surface (b). The change in the QD's charge state is signalled by a sharp dip in $\Delta f(V_\mathrm{b},\ z = c)$, corresponding to a sharp step in the tip-sample force. The QD loses an electron to the tip at V^- and gains a further electron at V^+. Increasing z decreases the fraction of bias that drops across the tip-QD bond α — this has the effect of pushing the charging features to higher absolute bias voltages. The inset of (b) displays the definition of z. The oscillation amplitudes were 0.04 nm (a) and 0.08 nm (b). The curves are vertically shifted for clarity.

Displayed in Fig. 4.2 are $\Delta f(V_\mathrm{b},\ z = c)$ curves from two datasets[†] at a range of different z values, (a) close to the surface and (b) far from the surface. In the absence of the QD, the $\Delta f(V_\mathrm{b},\ z = c)$ curve has a parabolic shape due to the electrostatic interaction between the tip and sample [90, 91]. The position of the maximum of this parabola corresponds to the contact potential difference (V_cpd) between the tip and sample electrodes, stemming from their different work functions. V_cpd is displayed in green in Fig. 4.2 and is seen to depend on z as observed many times before [92–94][‡]. As seen in Chap. 3, when the electron occupation of the QD N is suddenly changed, the additional charge on the QD leads to a sudden change in the electrostatic force between tip and sample. This leads to sharp 'dips' in $\Delta f(V_\mathrm{b},\ z = c)$. We do not observe any considerable dissipation of the tuning fork oscillation energy during the charge state transitions. This is likely since the tunnelling rate between tip and QD is far higher than the oscillation frequency of the tuning fork, leading to a non-hysteretic force-distance relationship [95]. In our experiments we observe two charging features close to zero bias, one at negative bias voltage (V^-) and one at positive bias voltage (V^+), marked in Fig. 4.2. At V^- the electron occupation of the QD N is decreased by one and at V^+ N is increased by one. Here, and in all following experimental data, the z axis was calibrated in the same way as described in Sec. 3.3.

When a bias voltage is applied to the surface, only a certain fraction of it drops across the tip-QD bond, determined by the tip-sample distance z. It follows that by modifying z, this fraction can be altered and the energy levels of the QD gated in this way. To isolate the effect of changing z on the measured frequency shift, we hold V_b constant and therefore acquire $\Delta f(V_\mathrm{b} = c,\ z)$ spectra. This detection scheme will in fact be preferred in this chapter: since the nc-AFM frequency shift signal is proportional to the spatial force gradient (see Eq. 4.1), measuring $\Delta f(V_\mathrm{b} = c,\ z)$ spectra is essential when the reconstruction of absolute forces is desired.

Fig. 4.3(a–b) show examples of data collected in this detection mode at V^+ and V^- respectively. Each trace represents a single spectrum with a different bias volt-

[†] The different datasets were recorded several months apart, with many tip preparations separating them. For this reason the shape of the mesoscopic tip apex was likely very different in both cases.

[‡] This effect stems from the distance dependence of the relative contribution of the macroscopic tip to the signal and will be discussed in more detail in Chap. 5.

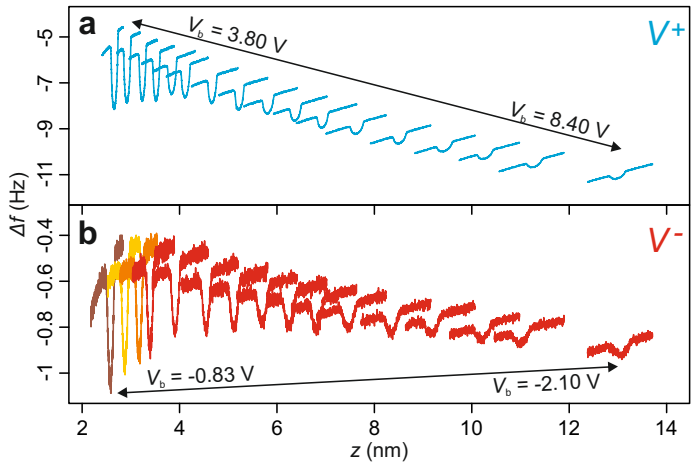

Figure 4.3: Distance dependence of $\Delta f(V_\mathrm{b} = c,\ z)$ spectra. Dips very similar to those in Fig. 4.2 are observed, since instead of bias voltage, z is now the gating parameter. A step in $\Delta f(V_\mathrm{b} = c,\ z)$ after the dip can be seen, especially in spectra measured close to the surface. The shifting of the curves comes from the effect that further away from the surface, more bias voltage must be applied to gate the QD and this increases the electrostatic background force in the junction. In (b), the four curves measured closest to the surface are displayed in differing colours in order to distinguish them more easily from another.

age — the ranges are displayed for the V^+ spectra (a) and the V^- spectra (b). The inclination of the individual spectra comes from the increasing van der Waals attraction between tip and surface as z is decreased. The displacement of the curves relative to each other on the Δf axis is due to the fact that further away from the surface more bias voltage must be applied to gate the QD's levels through the Fermi level of the tip, which increases the electrostatic background force in the junction.

The sudden dip in tip-sample force gradient with respect to distance indicates a change in tip-sample force. Indeed, the area under a $\Delta f(V_\mathrm{b} = c,\ z)$ dip is directly proportional to the associated change in force, as we will show here. We call this force $\Delta F^{\pm}_{\mathrm{t\text{-}s}}$, where $\Delta F^{+}_{\mathrm{t\text{-}s}}$ is the change in tip-sample force at V^+ and $\Delta F^{-}_{\mathrm{t\text{-}s}}$ corresponds to V^-. Zoomed in examples of $\Delta f(V_\mathrm{b} = c,\ z)$ spectra are exhibited in Fig. 4.4, the charging feature at V^+ in (a) and the feature at V^- in (b). Giessibl [96] showed that

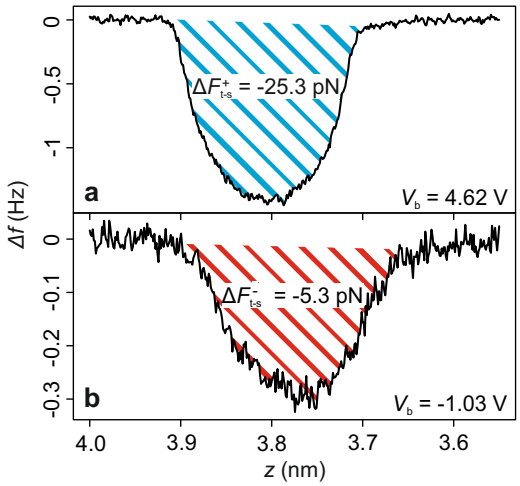

Figure 4.4: $\Delta f(V_\mathrm{b} = c,\ z)$ spectroscopy for extraction of the charging force. Solid black lines: typical $\Delta f(V_\mathrm{b} = c,\ z)$ dips at V^+ (a) and V^- (b) respectively. The shaded area under the dip represents the change in tip-sample force $\Delta F^{\pm}_{\text{t-s}}$. $\Delta F^{\pm}_{\text{t-s}}$ are defined to be negative since the change in force going from charge state N to $N \pm 1$ is negative, i.e. it becomes more attractive. The background frequency shift contributions from longer range electrostatic and van der Waals forces have been subtracted from the spectra. Both spectra were measured with an oscillation amplitude of $\sim$0.08 nm. The differing shapes in the $\Delta f(V_\mathrm{b} = c,\ z)$ curves can be explained by the fact that a small change in tip-sample separation, provided by the oscillating tuning fork, alters the voltage drop across the tip-molecule bond by an amount proportional to the applied bias voltage. At a higher absolute bias voltage (i.e. at V^+ as opposed to V^-), the lineshape is then much closer to the semi-circular weight function that the tuning fork oscillation imposes (see Eq. 4.60).

in the limit of small oscillation amplitude, where the tip-sample interaction does not vary during the oscillation cycle, a simple expression for Δf results:

$$\Delta f \simeq \frac{f_0}{2k_0} k_{\text{t-s}} = \frac{f_0}{2k_0} \frac{dF_{\text{t-s}}}{dz} \tag{4.1}$$

If the oscillation amplitude of the tuning fork is small enough such that $k_{\text{t-s}}$ does not appreciably change during the oscillation cycle, Δf and $k_{\text{t-s}}$ have the same line profile and are simply scaled by $f_0/2k_0$. However in our case the oscillation amplitude

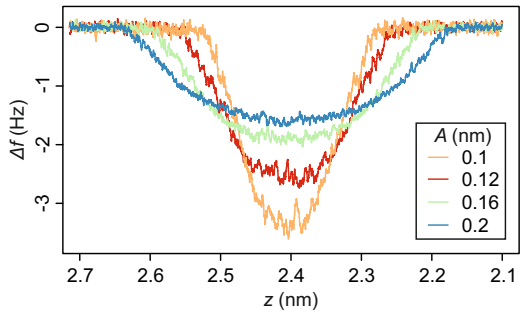

Figure 4.5: Oscillation amplitude dependence of $\Delta f(V_\mathrm{b} = c,\ z)$ dip shape. While the dip shape changes with amplitude, the area underneath it remains constant, i.e. the step in force remains constant. The spectra were all recorded at $V_\mathrm{b} = 4.2$ V.

is not necessarily this small: Fig. 4.5 shows how oscillation amplitude affects the dip shape and at large oscillation amplitudes the dip shape is close to the semi-circular weight function imposed by the oscillation (see Eq. 4.60). Nevertheless, the area under the dip remains constant regardless of amplitude, since the amplitude cannot affect the size of the force. It is then clear that while the lineshapes of frequency shift and stiffness differ, integrating over the area of the dip leads to the same force independent of the oscillation amplitude, with the inclusion of the scaling factor $f_0/2k_0$ to translate between frequency shift and force.

$\Delta f(V_\mathrm{b} = c,\ z)$ spectra therefore provide us with the means to analyze both $V^\pm$ and $\Delta F^\pm_\mathrm{t\text{-}s}$ as functions of z. In the coming sections this will help us gain considerable insight into the system.

4.1.2. Free energy of the system

We now turn to a theoretical description of the system, based on the SEB model. The starting point for this is the free energy of the system. The definition of free energy is the available energy in the system to do work, and as such it consists of the total energy in the system $E_\mathrm{s}(N)$ subtracted by the work done by the voltage source in charging the QD with N electrons $W(N)$:

$$A(N) = E_\mathrm{s}(N) - W(N) \tag{4.2}$$

Referring to Fig. 4.1(b), the electrostatic contribution to $E_{\mathrm{s}}(N)$, $E_{\mathrm{el}}(N)$, is

$$E_{\mathrm{el}}(N) = \frac{Q_{\mathrm{t}}^2}{2C_{\mathrm{t}}} + \frac{Q_{\mathrm{g}}^2}{2C_{\mathrm{g}}} \tag{4.3}$$

where $Q_{\mathrm{t,g}}$ are the polarization charges on the plates of the capacitors due to the applied bias voltage V_{b}. In the case that the QD is neutral, it is clear that $Q_{\mathrm{t}} = Q_{\mathrm{g}}$, since otherwise an electric field would exist between the inside plates of the two capacitors, i.e. where the QD is situated. However if confined, integer charge Ne is located on the QD, this is expelled to its surface, i.e. the inner capacitor plates in Fig. 4.1(b), where it adds to the polarization charges induced by the control charge Q_g that is located on the sample surface, i.e. the outer plate of the gate capacitor. For the total charges on the inner (and consequently outer) capacitor plates we therefore have

$$Q_{\mathrm{t}} - Q_{\mathrm{g}} = -Ne. \tag{4.4}$$

Q_g on the outer plate of the gate capacitor acts as the control charge of the quantum dot, because by moving this charge from ground, i.e. the tip electrode, through the voltage source to this plate all other charges are controlled, either by gating the QD (Ne) or by polarization (Q_t). The voltage drop in the SEB can be written as follows[†]:

$$\frac{Q_{\mathrm{t}}}{C_{\mathrm{t}}} + \frac{Q_{\mathrm{g}}}{C_{\mathrm{g}}} = V_{\mathrm{b}} \tag{4.5}$$

With this, we now express Eq. 4.3 in a more useful form. Starting at Eq. 4.5:

$$V_{\mathrm{b}} = \frac{Q_{\mathrm{g}} - Ne}{C_{\mathrm{t}}} + \frac{Q_{\mathrm{g}}}{C_{\mathrm{g}}}$$

$$Q_{\mathrm{g}} = \frac{NeC_{\mathrm{g}}}{C_{\Sigma}} + \frac{C_{\mathrm{t}}C_{\mathrm{g}}V_{\mathrm{b}}}{C_{\Sigma}} \tag{4.6}$$

$$\Rightarrow E_{\mathrm{el}}(N) = \frac{(Ne)^2}{2C_{\Sigma}} + \frac{C_{\mathrm{t}}C_{\mathrm{g}}V_{\mathrm{b}}^2}{2C_{\Sigma}} \tag{4.7}$$

$$\text{where} \quad C_{\Sigma} = C_{\mathrm{t}} + C_{\mathrm{g}} \tag{4.8}$$

[†] The right-hand side of Eq.4.5 should include V_{cpd}, however it is irrelevant to the results presented in this chapter and thus we exclude it for simplicity.

C_Σ represents the total capacitance of the QD with its environment[†]. The work done in charging the QD is the integral of the power output of the source over time, i.e. the time integral of the current drawn multiplied by the voltage supplied. Because in the present case Q_g acts as the control charge, $W(N)$ can also be written as

$$\begin{aligned} W(N) &= Q_\mathrm{g} V_\mathrm{b} \\ &= Ne\frac{C_\mathrm{g}}{C_\Sigma}V_\mathrm{b} + \frac{C_\mathrm{t}C_\mathrm{g}V_\mathrm{b}^2}{C_\Sigma} \end{aligned} \tag{4.9}$$

If the system were classical, combining Eqs. 4.7 and 4.9 would provide us with $A(N)$. However since we are in the quantum limit of the Coulomb blockade, a further term enters E_s to account for the QD's discrete energy levels. This takes the form of a sum of single particle energies E_n of all occupied quantum levels relative to the Fermi level of the tip, resulting in a final expression for $A(N)$:

$$A(N) = \sum_{n=0}^{N} E_\mathrm{n} + \frac{(Ne)^2}{2C_\Sigma} - Ne\frac{C_\mathrm{g}}{C_\Sigma}V_\mathrm{b} - \frac{C_\mathrm{t}C_\mathrm{g}V_\mathrm{b}^2}{2C_\Sigma} \tag{4.10}$$

This expression forms the basis of the derivations in the following sections, where we will discuss the individual terms in Eq. 4.10 in further detail.

4.1.3. Charging events of the QD

Voltage drop

As mentioned in Sec. 4.1.1, only a certain fraction of the applied bias voltage drops across the tip-QD bond, while the rest drops in the vacuum between the QD and the sample. Without charging effects this fraction would simply depend on the junction capacitances, but here it also depends on N. Utilizing Eqs. 4.5–4.6:

[†] There is in principle a contribution to the total capacitance of the QD with its environment C_Σ from the self-capacitance of the QD, i.e. the capacitance between the QD and ground at infinity, which scales with the size of the QD [97]. The close presence of the electrodes however reduces this contribution significantly [89]. Furthermore, the QDs discussed here are $\sim$1 nm in length, thus we expect the self-capacitance to be negligibly small as seen in similar systems [89].

$$
\begin{aligned}
V_\mathrm{t} &= V_\mathrm{b} - V_\mathrm{g} \\
&= V_\mathrm{b} - \frac{Q_\mathrm{g}}{C_\mathrm{g}} \\
&= V_\mathrm{b}\left(1 - \frac{C_\mathrm{t}}{C_\Sigma}\right) - \frac{Ne}{C_\Sigma} \\
V_\mathrm{t} &= \frac{C_\mathrm{g}}{C_\Sigma} V_\mathrm{b} - \frac{Ne}{C_\Sigma} \\
&= \alpha V_\mathrm{b} - \frac{Ne}{C_\Sigma} \qquad (4.11a) \\
\& \qquad V_\mathrm{g} &= \frac{C_\mathrm{t}}{C_\Sigma} V_\mathrm{b} + \frac{Ne}{C_\Sigma} \\
&= (1-\alpha) V_\mathrm{b} + \frac{Ne}{C_\Sigma} \qquad (4.11b)
\end{aligned}
$$

Here we have defined

$$\alpha \equiv \frac{C_\mathrm{g}}{C_\Sigma}. \qquad (4.12)$$

According to Eqs. 4.11(a–b), α represents the voltage drop fraction across the tip-QD bond in the absence of charging effects. α is a parameter of great importance and will be discussed at length later in the chapter. Fig. 4.6(c) displays Eqs. 4.11(a–b) as functions of V_b, where the sharp jumps in $V_{\mathrm{t/g}}$ upon changes in N are apparent.

Electrochemical potential

The Fermi level of the tip, i.e. the electrochemical potential of the electrons in the tip, is the quantity that determines at which energies the QD charging events occur. As the electrochemical potential of the QD crosses that of the tip, it becomes energetically favourable for an electron to hop either on or off the QD. By analyzing the QD's electrochemical potential we can therefore gain further insight into the charging events.

From thermodynamics, the electrochemical potential of a QD with N electrons $\mu(N)$ is defined as the partial derivative of the free energy A with respect to particle number N, evaluated at constant volume V and temperature T. Due to its first term, Eq. 4.10 is however discontinuous in N, taken as an element of $\mathbb{R}$, so instead we use a finite difference approximation:

$$\begin{aligned}\mu(N) &= \left.\frac{\Delta A}{\Delta N}\right|_N \\ &= \frac{A(N) - A(N-1)}{N - (N-1)} \\ &= E_\mathrm{N} + \frac{(N - \frac{1}{2})e^2}{C_\Sigma} - \frac{C_\mathrm{g}}{C_\Sigma} eV_\mathrm{b} \\ &= E_\mathrm{N} + \frac{(N - \frac{1}{2})e^2}{C_\Sigma} - e\alpha V_\mathrm{b} \end{aligned} \tag{4.13}$$

Fig. 4.6(b) shows $\mu(N)$ for $N = 0$, $N = 1$, $N = 2$ and $N = 3$ as a function of V_b, as in Eq. 4.13. $\mu(0)$, $\mu(1)$, $\mu(2)$ and $\mu(3)$ are seen to continually decrease with positive bias voltage, where the slope is described by α — the fraction of bias voltage that drops between the tip and the QD at $N = 0$ is naturally responsible for shifting the QD's electrochemical potential. At $V^{(N)}$ the chemical potential of the QD charged with N electrons drops below the chemical potential μ_tip of the tip. At this point, an additional electron hops onto the quantum dot, raising its charge from $N - 1$ to N. V^+ and V^- as defined in Sec. 4.1.1 correspond to $V^+ = V^{(2)}$ and $V^- = V^{(1)}$, as shown in the figure. As Fig. 4.6(b) shows, for any bias voltage V_b the actual chemical potential of the QD is the one given by the largest $\mu(N)$ for which $\mu(N) < \mu_\mathrm{tip}$. This yields the sawtooth variation of the QD's chemical potential as a function of the bias voltage [bold line in Fig. 4.6(b)]. The size of the jump in $\mu(N)$ at $V^{(N)}$ can be determined as follows:

$$\mu(N+1) - \mu(N) = E_{\mathrm{N}+1} - E_\mathrm{N} + \frac{e^2}{C_\Sigma} \tag{4.14}$$

The third RHS term in Eq. 4.14 is known as the *charging energy* $E_\mathrm{c} = {}^{e^2}/_{C_\Sigma}$, as asserted in Sec. 4.1, and represents the minimum quantity of energy required to add an additional electron to the QD. Since for a molecule, single-particle energies E_N are pairwise equal, i.e. $E_1 = E_2$, $E_3 = E_4$ etc., the jump in $\mu(N)$ will alternate between the minimum and a larger value (note that the larger values are not unique) as the QD's energy levels are sequentially filled, with a respective maximum population of two electrons; this is exhibited in Fig. 4.6(b). Similarly, the bias voltage difference between successive charging events will alternate; for example, the difference $V^{(1)} - V^{(0)}$ will be larger than $V^{(2)} - V^{(1)}$, since in this example $E_1 - E_0 \neq 0$. Similarly, the

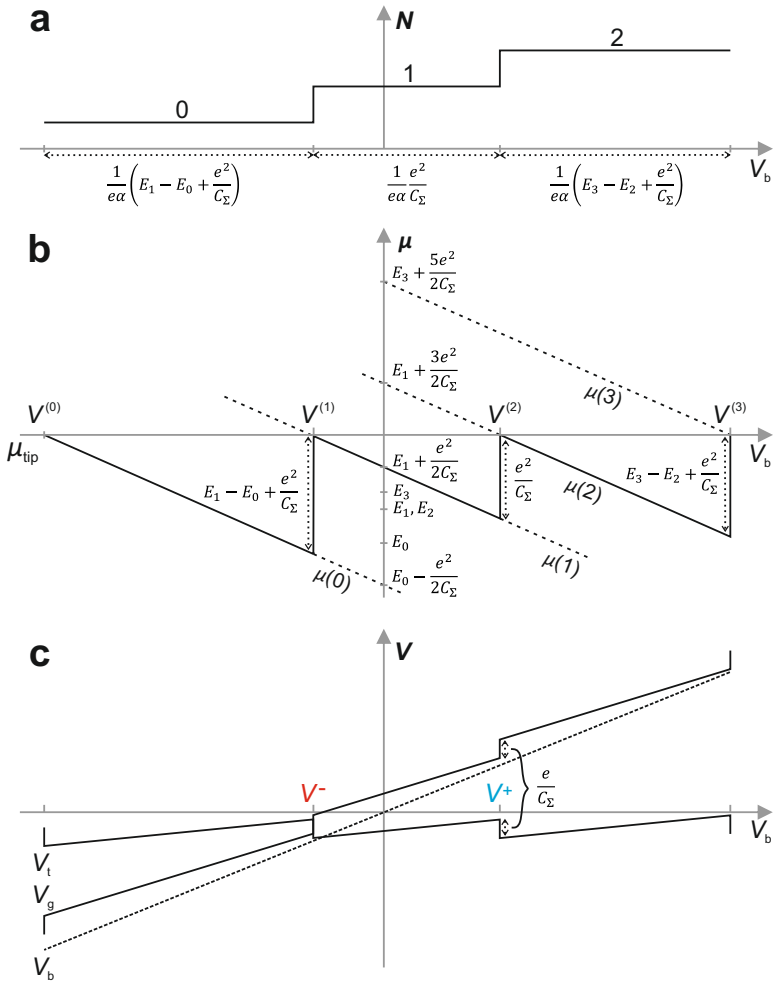

Figure 4.6: (a) The electron occupation of the QD as a function of V_b is shown schematically. (b) The QD's corresponding electrochemical potential μ. The step in $\mu(N)$ at the charging features consists of the difference in single particle energies as well as the charging energy E_c. Since every second electron to occupy the QD fills an orbital, the following electron must enter a new orbital and the step in $\mu(N)$ will alternate between the minimum and a non-unique larger value. For example if $N = 1$ at $V_b = 0$, there would be a large step in $\mu(N)$ at $V^{(1)}$ and $V^{(3)}$ and the minimum step at $V^{(2)}$. (c) The voltage across the tunnel and gate capacitors as functions of V_b [see Eqs. 4.11(a–b)]. As V_b is increased the voltage across V_g increases faster than V_t since a larger fraction of V_b drops across the gate capacitor. At $V^\pm$ the voltage across the capacitors jumps by an equal and opposite value, e/C_Σ.

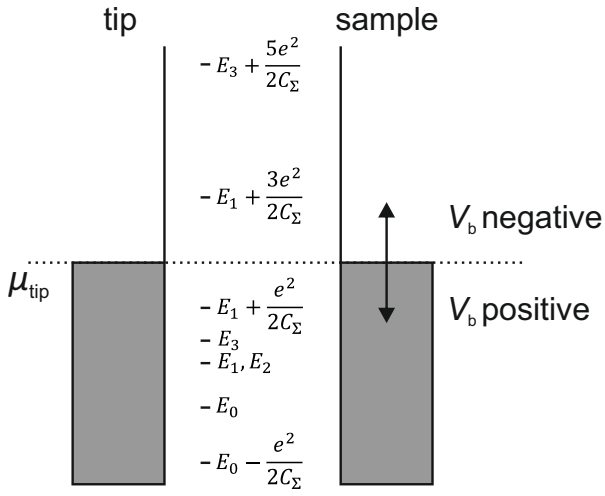

Figure 4.7: Schematic of molecular energy levels and charging energies close to the Fermi level of the tip.

bias voltage difference between successive charging events will alternate. A schematic of the molecular energy levels and charging energies is shown in Fig. 4.7.

Voltage and free energy at charge transitions

We now determine analytical expressions for the bias voltages at which the charge transitions occur, i.e. $V^{\pm}$. Fig. 4.8(a) shows example free energy curves: Eq. 4.10 plotted as a function of V_b for $N = 0, 1, 2$. The reason for these values of N is our assertion that $N = 1$ at $V_\mathrm{b} = 0$. We will qualify this assertion later in the chapter. The points at which the curves cross are the points at which the charge transitions occur. Since they represent the lowest energy states, the bold curves portray the states in which the system is in at any given bias voltage. The fourth term in Eq. 4.10, quadratic in V_b, is responsible for the parabolic shape of the curves in Fig. 4.8(a). However it is not dependent on N, and omitting this term should result in the 'linearized' free energy curves crossing at the same V_b values. Fig. 4.8(b) demonstrates that this is indeed true; the relevance of this aside will become clear later in the chapter.

We can find expressions for $V^{\pm}$ by comparing $A(1)$ to $A(1 \pm 1)$ using Eq. 4.10:

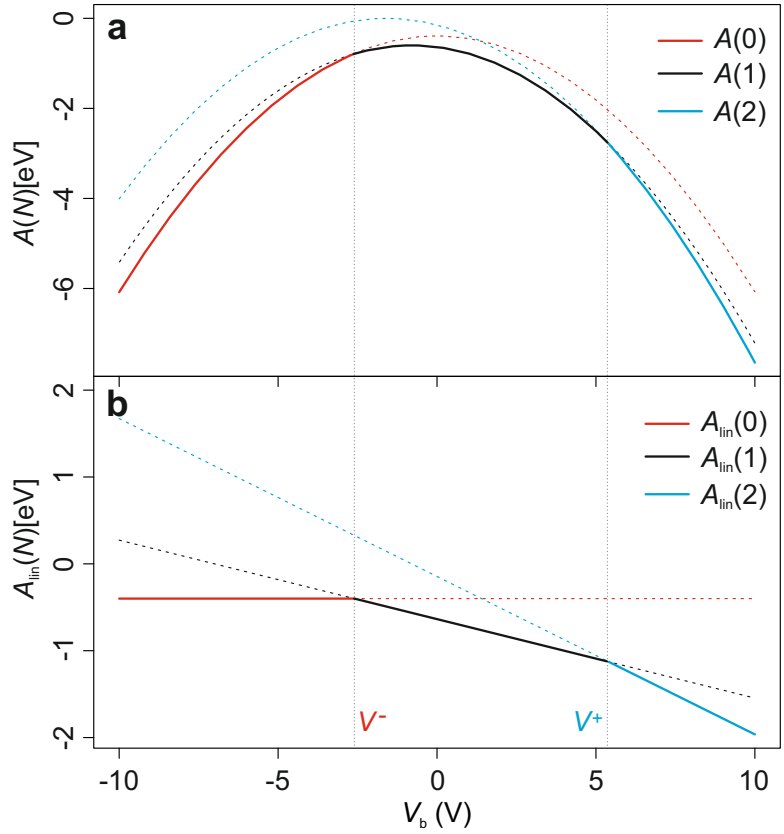

Figure 4.8: Free energy of the QD. (a) $A(0)$, $A(1)$ and $A(2)$ according to Eq. 4.10. Since the QD always remains in the lowest energy state, electrons tunnel to and from the QD at $V^{\pm}$; bold lines represent the favoured charge state at that particular bias voltage. The parabolic shape of A comes from the fourth term in Eq. 4.10. (b) Eq. 4.10 plotted without its fourth term, i.e. 'linearized' free energy A_{lin}. The plotting parameters, chosen to approximately match our experimental data, were: $C_{\mathrm{t}} = 0.2$ aF, $C_{\mathrm{g}} = 0.02$ aF, $E_0 = -0.4$ eV, $E_1 = -0.6$ eV and $E_2 = -0.6$ eV.

$$
\begin{aligned}
A(0,\ V^-) &= A(1,\ V^-) \\
E_0 - \frac{C_\mathrm{t}C_\mathrm{g}(V^-)^2}{2C_\Sigma} &= E_0 + E_1 + \frac{e^2}{2C_\Sigma} - \frac{C_\mathrm{g}}{C_\Sigma}eV^- \\
&\quad - \frac{C_\mathrm{t}C_\mathrm{g}(V^-)^2}{2C_\Sigma} \\
V^- &= \frac{1}{e\alpha}\left(E_1 + \frac{e^2}{2C_\Sigma}\right) \qquad (4.15a)
\end{aligned}
$$

Performing the same analysis for V^+:

$$
\begin{aligned}
A(1,\ V^+) &= A(2,\ V^+) \\
E_0 + E_1 + \frac{e^2}{2C_\Sigma} - \frac{C_\mathrm{g}}{C_\Sigma}eV^- - \frac{C_\mathrm{t}C_\mathrm{g}(V^-)^2}{2C_\Sigma} &= E_0 + E_1 + E_2 + \frac{4e^2}{2C_\Sigma} - 2\frac{C_\mathrm{g}}{C_\Sigma}eV^+ \\
&\quad - \frac{C_\mathrm{t}C_\mathrm{g}(V^+)^2}{2C_\Sigma} \\
V^+ &= \frac{1}{e\alpha}\left(E_2 + \frac{3e^2}{2C_\Sigma}\right) \qquad (4.15b)
\end{aligned}
$$

At this point we can in fact prove that $E_1 = E_2$ is by far the most likely scenario. As discussed above in Sec. 4.1, we are in the quantum limit of the Coulomb blockade. This can be seen from the characteristic energy level spacings of the QD, in the eV range, and the charging energy for a QD of this size, also in the eV range [98–101]. For this reason there are two options as to the value of $\Delta E = E_2 - E_1$: ~ 1 eV or 0. We now argue that the case $\Delta E = 0$ is highly probable. We can construct the difference between the charging features, $\Delta V = V^+ - V^-$, using Eqs. 4.15(a–b):

$$
\Delta V = \frac{1}{e\alpha}\left(\Delta E + \frac{e^2}{C_\Sigma}\right) \qquad (4.16)
$$

If the tip and sample electrodes formed a parallel plate capacitor, then the voltage would drop linearly between them. Although this is certainly an over-simplification, we do not expect our situation to deviate too far from this. We can also assume that to first order, our QD does not affect this potential distribution. In this case the voltage drop fraction α can be described geometrically as d/z, where d is the effective distance between the point charge QD and the tip. In Sec. 3.1, d was shown to be equal to ~ 0.7 nm for a PTCDA QD. The innermost curve in Fig. 4.2 was measured

at $z = 4.2$ nm and displayed a value for ΔV of $\simeq 6$ V. From our simple geometric expression we see that $\alpha \simeq 0.15$, meaning that

$$\Delta E + \frac{e^2}{C_\Sigma} \simeq 0.15 \cdot 6 \text{ eV} \simeq 1 \text{ eV} \tag{4.17}$$

Since e^2/C_Σ must be on the order of 1 eV, the only possible conclusion is that $\Delta E = 0$, i.e. that the charging features at V^- and V^+ correspond to the first and second electrons entering the *same* molecular orbital. In this case we see that $V^\pm$ are separated by $\frac{1}{e\alpha}\frac{e^2}{C_\Sigma}$, corresponding to the charging energy of the QD scaled by $e\alpha$. We also observe from Eqs. 4.15(a–b) that $V^\pm$ are offset on the bias voltage axis by $E_1 = E_2$. If the charging energy were to dwarf the single particle energy levels, the charging events would be symmetric around zero bias voltage, as demonstrated in other systems [79]. We can simplify Eq. 4.16 further:

$$\begin{aligned} \Delta V &= \frac{1}{e\alpha}\frac{e^2}{C_\Sigma} \\ &= \frac{C_\Sigma}{C_\text{g}}\frac{e}{C_\Sigma} \\ &= \frac{e}{C_\text{g}} \end{aligned} \tag{4.18}$$

This illustrates the interesting situation that if $E_1 = E_2$, the gate capacitance alone determines the bias voltage spacing of the charging features, regardless of the capacitance between the tip and the QD.

4.1.4. Charging force

As Stomp et al. [79] stated, the force acting between the single electron box and the sample is $-\partial A/\partial z$. Before the differentiation is performed, we must determine which quantities are dependent on z. Since the QD is several nanometres above the surface, we assume that the nature of its bond to the tip is not dependent on distance and therefore C_t is constant. It is however clear that $C_\text{g} = C_\text{g}(z)$, since the interaction between the QD and the surface does depend on the tip-sample separation. Computing the derivative and recalling Eq. 4.11(b):

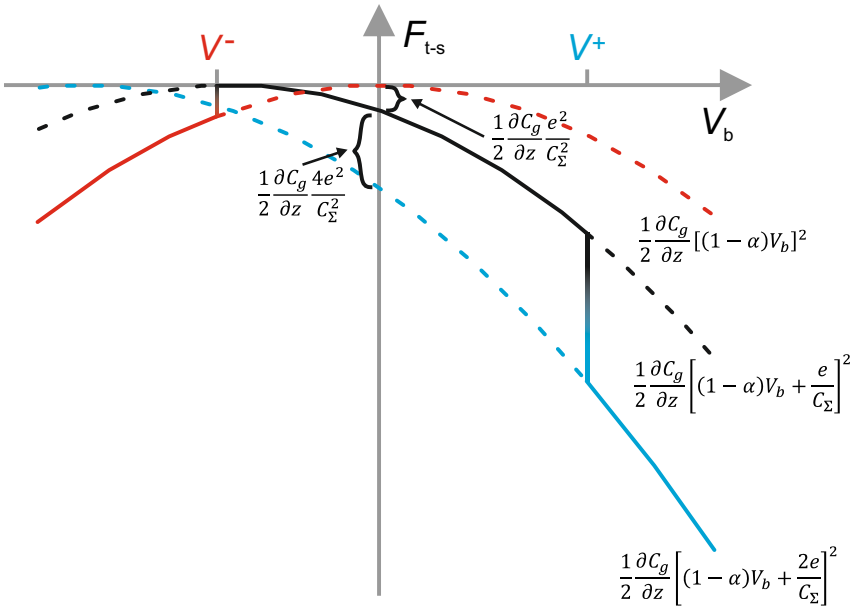

Figure 4.9: Schematic diagram of the total force between tip and sample as a function of V_b and N and at constant z. The solid line represents the charge state that the QD is in and therefore the force that acts between tip and sample in experiment. It is important to note that the charge transitions are of course not infinitely sharp in experiment; see Sec. 4.A.2 for more details.

$$\begin{aligned} F_\mathrm{t\text{-}s}(N,\ V_\mathrm{b},\ z) &= -\frac{\partial A}{\partial z} \\ &= -\frac{\partial}{\partial z}\left[\sum_{n=0}^{N} E_\mathrm{n} + \frac{(Ne)^2}{2C_\Sigma} - Ne\frac{C_\mathrm{g}}{C_\Sigma}V_\mathrm{b} - \frac{C_\mathrm{t}C_\mathrm{g}V_\mathrm{b}^2}{2C_\Sigma}\right] \\ &= \frac{1}{2C_\Sigma^2}\frac{\partial C_\mathrm{g}}{\partial z}\left[(Ne)^2 + 2NeV_\mathrm{b}C_\mathrm{t} + V_\mathrm{b}^2C_\mathrm{t}^2\right] \\ &= \frac{1}{2}\frac{\partial C_\mathrm{g}}{\partial z}V_\mathrm{g}^2 \end{aligned} \tag{4.19}$$

We note that because of the steps in V_g at the charging events [see Fig. 4.6(c)], $F_\mathrm{t\text{-}s}$ also has steps, as indicated schematically in Fig. 4.9. Eq. 4.19 provides us with the entire force acting between the QD and the sample, but as shown in Sec. 4.1.1, the

quantity accessible in experiment is $\Delta F^{\pm}_{\text{t-s}}$, i.e. the change in tip-sample force when the QD's charge state is changed. However we can use Eq. 4.19, Eqs. 4.15(a–b) and Eq. 4.11(b) to obtain expressions for $\Delta F^{\pm}_{\text{t-s}}$:

$$\begin{aligned}
\Delta F^{-}_{\text{t-s}} &= F_{\text{t-s}}(0,\ V^-,\ z) - F_{\text{t-s}}(1,\ V^-,\ z) \\
&= \frac{1}{2}\frac{\partial C_{\text{g}}}{\partial z}\left\{(1-\alpha)^2(V^-)^2 - \left[(1-\alpha)V^- + \frac{e}{C_\Sigma}\right]^2\right\} \\
&= -\frac{e}{C_\Sigma}\frac{\partial C_{\text{g}}}{\partial z}\left[(1-\alpha)V^- + \frac{e}{2C_\Sigma}\right] \\
&= -\frac{1}{\alpha C_\Sigma}\frac{\partial C_{\text{g}}}{\partial z}\left[(1-\alpha)E_1 + \frac{e^2}{2C_\Sigma}\right] \qquad (4.20a) \\
\&\quad \Delta F^{+}_{\text{t-s}} &= F_{\text{t-s}}(2,\ V^+,\ z) - F_{\text{t-s}}(1,\ V^+,\ z) \\
&= \frac{1}{2}\frac{\partial C_{\text{g}}}{\partial z}\left\{\left[(1-\alpha)V^+ + 2\frac{e}{C_\Sigma}\right]^2 - \left[(1-\alpha)V^+ + \frac{e}{C_\Sigma}\right]^2\right\} \\
&= \frac{e}{C_\Sigma}\frac{\partial C_{\text{g}}}{\partial z}\left[(1-\alpha)V^+ + \frac{3e}{2C_\Sigma}\right] \\
&= \frac{1}{\alpha C_\Sigma}\frac{\partial C_{\text{g}}}{\partial z}\left[(1-\alpha)E_2 + \frac{3e^2}{2C_\Sigma}\right] \qquad (4.20b)
\end{aligned}$$

We can obtain two independent expressions for $\partial C_{\text{g}}/\partial z$ in terms of $\partial V^{\pm}/\partial z$, which are experimentally accessible:

$$\begin{aligned}
\frac{\partial V^-}{\partial z} &= \frac{\partial}{\partial z}\left[\frac{1}{e\alpha}\left(E_1 + \frac{e^2}{2C_\Sigma}\right)\right] \\
&= -\frac{1}{e}\frac{\partial C_{\text{g}}}{\partial z}\frac{C_{\text{t}}}{C_{\text{g}}^2}\left(E_1 + \frac{e^2}{2C_\Sigma}\right) - \frac{1}{e}\frac{C_\Sigma}{C_{\text{g}}}\frac{e^2}{2}\frac{1}{C_\Sigma^2}\frac{\partial C_{\text{g}}}{\partial z} \\
\frac{\partial C_{\text{g}}}{\partial z} &= -\frac{e\alpha C_{\text{g}}}{(1-\alpha)E_1 + \frac{e^2}{2C_\Sigma}}\frac{\partial V^-}{\partial z} \qquad (4.21a) \\
\&\quad \frac{\partial V^+}{\partial z} &= \frac{\partial}{\partial z}\left[\frac{1}{e\alpha}\left(E_2 + \frac{3e^2}{2C_\Sigma}\right)\right] \\
&= -\frac{1}{e}\frac{\partial C_{\text{g}}}{\partial z}\frac{C_{\text{t}}}{C_{\text{g}}^2}\left(E_2 + \frac{3e^2}{2C_\Sigma}\right) - \frac{1}{e}\frac{C_\Sigma}{C_{\text{g}}}\frac{3e^2}{2}\frac{1}{C_\Sigma^2}\frac{\partial C_{\text{g}}}{\partial z} \\
\frac{\partial C_{\text{g}}}{\partial z} &= -\frac{e\alpha C_{\text{g}}}{(1-\alpha)E_2 + \frac{3e^2}{2C_\Sigma}}\frac{\partial V^+}{\partial z} \qquad (4.21b)
\end{aligned}$$

We then substitute Eqs. 4.21(a–b) into Eqs. 4.20(a–b) respectively and arrive at the following system of equations:

$$V^- = \frac{1}{e\alpha}\left(E_1 + \frac{e^2}{2C_\Sigma}\right) \tag{4.22a}$$

$$V^+ = \frac{1}{e\alpha}\left(E_2 + \frac{3e^2}{2C_\Sigma}\right) \tag{4.22b}$$

$$\Delta F^-_{\text{t-s}} = e\alpha\frac{\partial V^-}{\partial z} \tag{4.22c}$$

$$\Delta F^+_{\text{t-s}} = e\alpha\frac{\partial V^+}{\partial z} \tag{4.22d}$$

This system of four equations connects the four independent model parameters E_1, E_2, C_g and C_t to the measurable quantities V^+, V^-, $\Delta F^+_{\text{t-s}}$, $\Delta F^-_{\text{t-s}}$, $\partial V^+/\partial z$ and $\partial V^-/\partial z$. In principle, this system is sufficient to determine E_1, E_2, C_g and C_t. However, since we know from experiment that $E_1 = E_2$, the system is overdetermined. Furthermore, Eqs. 4.22(c–d) provide us with two independent results for α:

$$\alpha = \mp\frac{\Delta F^\pm_{\text{t-s}}}{e\frac{\partial V^\pm}{\partial z}} \tag{4.23}$$

If our assumptions so far are correct, the two expressions for α in Eq. 4.23 will be equivalent[†]. The testing of this prediction using experimental data will be carried out in the following section.

4.1.5. Applying the theory to experimental data

In Sec. 4.1.1 we showed how $\Delta f(V_\text{b} = c,\ z)$ spectroscopy can provide us with $V^\pm$ as well as $\Delta F^\pm_{\text{t-s}}$ as functions of z. In this section we therefore employ this detection mode in order to extract the two quantities required to determine α: $\Delta F^\pm_{\text{t-s}}$ and $\partial V^\pm/\partial z$ (see Eq. 4.23). Fig. 4.10 displays the result of four $\Delta f(V_\text{b} = c,\ z)$ datasets, represented by different colours. Three of the datasets were measured

[†] Note the sign in Eq. 4.23: in experiment, $\Delta F^\pm_{\text{t-s}}$ is always negative, whereas $\partial V^+/\partial z$ is always positive and $\partial V^-/\partial z$ always negative. As a result α is positive in both cases, as it must be.

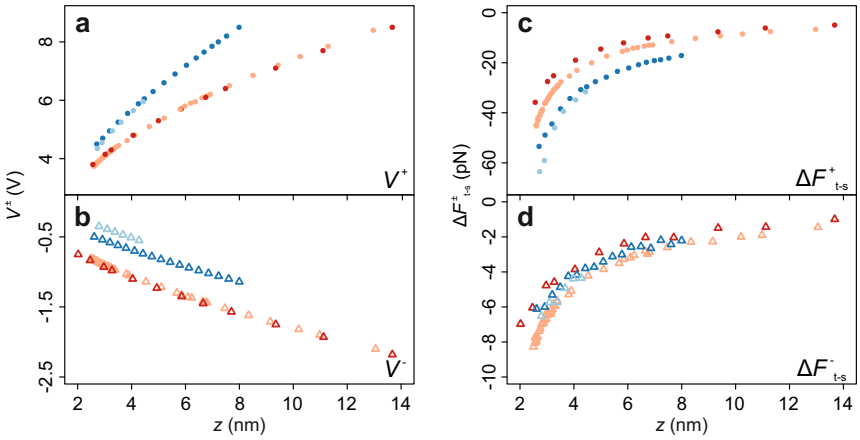

Figure 4.10: Dip positions and forces from four separate $\Delta f(V_\text{b} = c,\ z)$ spectroscopy datasets. (a–b) V^+ and V^- respectively, which in $\Delta f(V_\text{b} = c,\ z)$ spectra correspond to the value of V_b held constant while z is swept. As shown, the absolute values of $V^\pm$ can vary strongly between datasets due to differences in the adsorption characteristics of the QD on the tip. (c–d) $\Delta F^+_{\text{t-s}}$ and $\Delta F^-_{\text{t-s}}$ respectively, determined by integrating $\Delta f(V_\text{b} = c,\ z)$ spectra as demonstrated in Fig. 4.4. The colours represent the same datasets in the remainder of this section.

above clean Ag(111), while the dataset represented by light blue symbols was measured above PTCDA/Ag(111). The light and dark red datasets were measured with the same QD, however the light red dataset was recorded four days after the dark red dataset. The liquid nitrogen and helium cryostats were in fact refilled between the two datasets, i.e. the QD remained attached to the tip during this procedure and afterwards the sample surface was re-approached and the z-axis re-calibrated according to the procedure described in Sec. 3.3. Nevertheless the two datasets are non-identical, suggesting that the adsorption characteristics of the QD on the tip were modified in the time between the recording of the datasets. The light and dark blue datasets were also measured with the same QD (although different from the QD used in the red datasets); the difference between these two datasets is discussed further later in the section. In each case, the bias voltage was set to a specific value and the tip-sample distance set to a certain value such that a distance sweep of a few ångströms would be sufficient to detect the dip. In (a) and (c) the filled circles

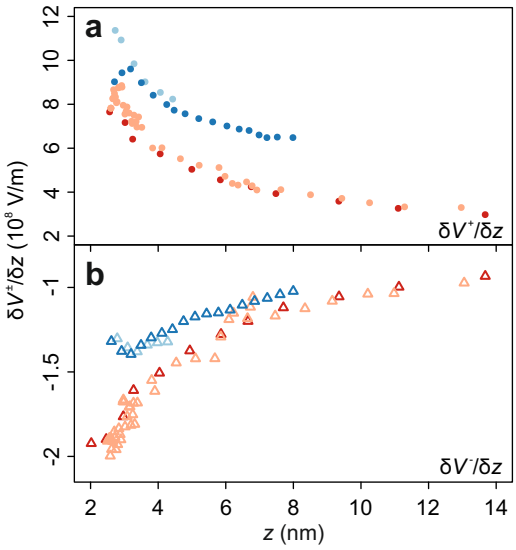

Figure 4.11: $\partial V^{\pm}/\partial z$ computed numerically from the $V^{\pm}$ data in Fig. 4.10(a–b). Nearest neighbours on each side were used to compute the derivatives except for the dataset represented by light red symbols — in dense graph regions all points within 1 nm on either side of each point were used to determine the derivative and in sparse graph regions the nearest neighbour method was employed.

represent the V^+ values and the size of the corresponding force step $\Delta F^+_{\text{t-s}}$ respectively. In (b) and (d) the unfilled triangles represent the V^- values and the size of the corresponding force step $\Delta F^-_{\text{t-s}}$. In the rest of this section the colours represent the same datasets and the filled circles and unfilled triangles represent data derived from spectra at V^+ and V^- respectively. $\Delta F^{\pm}_{\text{t-s}}$ were determined by integrating over the measured $\Delta f(V_{\text{b}} = c,\ z)$ spectra as in Fig. 4.4. The size of the force step increases monotonically as the surface is approached, since the interaction between the QD and the polarization charge in the surface as well as the attractive image force between QD and surface increases. We observe variation between datasets in both dip position and force due to differing tip-QD bonding characteristics between experiments as mentioned in Sec. 4.1.1, however the distance dependence for both quantities remains similar in both cases.

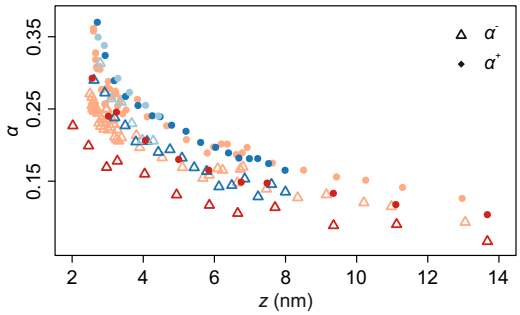

Figure 4.12: The fraction of bias voltage drop without charging effects, α, determined according to Eq. 4.23. Since the interaction between the surface and the QD decreases as z increases, α decreases. The same z trend is observed for all datasets with small variations in absolute values. The discrepancy between the two branches, consistent across the datasets, may be due to a different value of α for different charge states. The values of α in the dataset displayed by red symbols differ strongly from those in the other three datasets; this again points to differing tip-QD adsorption characteristics. Note that the QD in the light blue dataset, measured above PTCDA/Ag(111), displays a slightly larger α than the same QD above plain silver (dark blue). This can be understood by recalling Eq. 4.12 — the presence of the dielectric PTCDA layer increases the gate capacitance C_g, leading to an increase in α.

Besides $\Delta F^{+}_{\text{t-s}}$, the second piece of experimental information that is required to determine α is the derivatives of $V^{\pm}$ with respect to distance. These derivatives can be computed numerically from Fig. 4.10(a–b) and are shown in Fig. 4.11(a–b). The data were determined using the method of finite differences. In graph regions where the data were dense with respect to z, using only nearest neighbour differences results in large noise. For the dataset represented by light red symbols, we therefore used all points within 1 nm on either side of each point to determine the derivative, while assuming that the curve is linear in that region. 1 nm was found empirically to be the best compromise between noise reduction and oversmoothing, i.e. distortion of the true shape of the derivative. In sparse graph regions and all other datasets the nearest neighbour on each side was used to compute the derivatives.

Since $\Delta F^{\pm}_{\text{t-s}}$ and $\partial V^{\pm}/\partial z$ have been determined, it is now possible to evaluate α. Fig. 4.12 shows α with both branches displayed. We observe a systematic discrepancy: α computed from $\Delta F^{-}_{\text{t-s}}$ and $\partial V^{-}/\partial z$ is always smaller than from the branch

derived from $\Delta F^{+}_{\text{t-s}}$ and $\partial V^{+}/\partial z$. To the best of our knowledge, this is the first time that a discrepancy in α has been observed in such a system. This could point towards a breakdown in the SEB model and the systematic discrepancy suggests that there is a physical effect responsible, especially since the size of the discrepancy is very similar for all datasets.

More precisely, the data suggest that the bias voltage fraction α depends on the electron population of the QD, contradicting the assumptions of the SEB model, where C_{g}/C_{Σ} is assumed to be uniform regardless of the number of electrons on the QD. Within the framework of the SEB model this corresponds to capacitances that are dependent on N, i.e. $C_{\text{t,g}} = C_{\text{t,g}}(N)$. In fact the problem of nanoscale capacitance in small systems has been treated both quantum mechanically, considering the electrochemical potential of the system as above [102–104] and classically, by considering direct Coulomb and polarization interactions in few-electron systems [105]. Both approaches can be shown to produce an equivalent result, that the difference in electrochemical potential between the state with $N+1$ electrons and that with N electrons determines the capacitance of state N, $C_{\Sigma}(N)$:

$$\frac{e^2}{C_{\Sigma}(N)} = \mu(N+1) - \mu(N) \tag{4.24}$$

The constant interaction model then goes on to assume that $C_{\Sigma}(N)$ is constant as a function of N, leading to Eq. 4.14, i.e. that the electrochemical potential changes by the same amount every time an electron is added to the system. However numerical simulations have shown this not to be a good assumption for systems with only a few electrons [102, 105], which when considered on the level of interelectronic Coulombic interactions is intuitively expected. It is therefore worthwhile to investigate the consequences of deriving the results in this section with $C_{\Sigma} = C_{\Sigma}(N)$, i.e. $\alpha = \alpha(N)$. As will be seen in the next section, this is best carried out with the point charge model.

4.2. Point charge model

In this section we describe how the model introduced in Chap. 3 can also be used to understand the tip-QD-sample junction. The single electron box model in the previous section can be applied without modification to a system in the classical limit of the Coulomb blockade; including the single particle energies allowed it to be applicable in the quantum limit as well (Eq. 4.10). However we saw at the end of the previous section that in our case the SEB model seems to break down. The model described in this section on the other hand is empirically inspired by the SQDM experiments described in this thesis. The degree of control we exercise over the junction allows us to construct the model based on a very well defined geometry: the QD is modelled as a point at a certain location beneath the tip. For this reason we refer to this model from here on as the point charge (PC) model. As we will see, experimental information is combined in the PC model such that the electronic properties of the QD can be obtained directly. More precisely, the energy level positions and interelectronic Coulomb repulsion of the QD are the free parameters in the model and applying the model to experimental data helps us reconstruct these fundamentally important quantities. However most importantly, in the present section the model is extended to deal with the case that $\alpha = \alpha(N)$, and the results of this presented and discussed.

4.2.1. Predictions of the point charge model

Energy of the system

The system energy with N electrons in the PC model requires an expression for every single charge state of interest of the QD. The energy equations expressed in general terms are then as follows:

$$E(N-1) = \sum_{n=0}^{N-1} E_{\mathrm{n}} + E_{\mathrm{r}}(N-1) - \alpha(z)(N-1)eV_{\mathrm{b}} \tag{4.25a}$$

$$E(N) = \sum_{n=0}^{N} E_{\mathrm{n}} + E_{\mathrm{r}}(N) - \alpha(z)NeV_{\mathrm{b}} \tag{4.25b}$$

$$E(N+1) = \sum_{n=0}^{N+1} E_{\mathrm{n}} + E_{\mathrm{r}}(N+1) - \alpha(z)(N+1)eV_{\mathrm{b}} \tag{4.25c}$$

The first term in each equation is the sum of single particle energies as seen earlier in the chapter. $E_\mathrm{r}(N)$ is the total intramolecular, Coulombic repulsion energy due to the presence of N electrons. $\alpha(z)$ is the fraction of V_b that drops across the tip-QD bond as in Eq. 4.12. $\alpha(z)NeV_\mathrm{b}$ is then the electrostatic energy of a QD occupied by N electrons in the electric field between tip and sample at bias voltage V_b.

We can further simplify Eqs. 4.25(a–c) by considering which molecular orbital(s) are involved in the charging features. In the following we argue that the LUMO of the molecular QD is the orbital involved in both charging features. The LUMO of PTCDA adsorbed flat on Ag(111) has an occupation of $\sim 1.8\ e^-$, and loses one electron as the QD is lifted from the surface, which is signalled by a Kondo-like transport resonance during retraction [106, 107]. This leads us to believe that the LUMO is singly occupied when the molecular QD is hanging from the tip; this has also been predicted in a DFT-LDA-based calculation [107]. We cannot categorically exclude that a second electron leaves the QD when the tunnelling current is already too small to detect; the absence of any experimental signatures however provides us with confidence that this does not occur. We therefore assert that the charging feature at V^- is the singly occupied LUMO becoming fully depopulated. We define the position in energy of the LUMO relative to the Fermi level of the tip as ε_0, where $\varepsilon_0 < 0$ since the LUMO is below the Fermi level of the tip. In Sec. 4.1.3 we also argued that the energy level separation between the features at V^- and V^+ was zero, i.e. $\Delta E = 0$. This therefore means that the feature at V^+ corresponds to the LUMO of the QD gaining a second electron and thereby becoming fully occupied. The second electron possesses the same single particle energy as the first, ε_0, but the intramolecular Coulomb repulsion between the first and second electrons also affects the energy of this charge state. We describe this repulsion as U. The result of this is that the LUMO of the QD is singly occupied at zero bias voltage, i.e. that the QD is neutral when the LUMO is singly occupied. We can disregard the electrons in lower lying orbitals due to the positive ionic cores of the QD's atoms and therefore state that due to the singly occupied LUMO, $N = 1$, as asserted earlier in the chapter. Incorporating this information into Eqs. 4.25(a–c) and setting $E(0) = 0$ for simplicity, while recognizing that $E_1 = E_2 \equiv \varepsilon_0$ as explained above and that $E_\mathrm{r}(0) = E_\mathrm{r}(1) = 0$, we come to our final energy equations

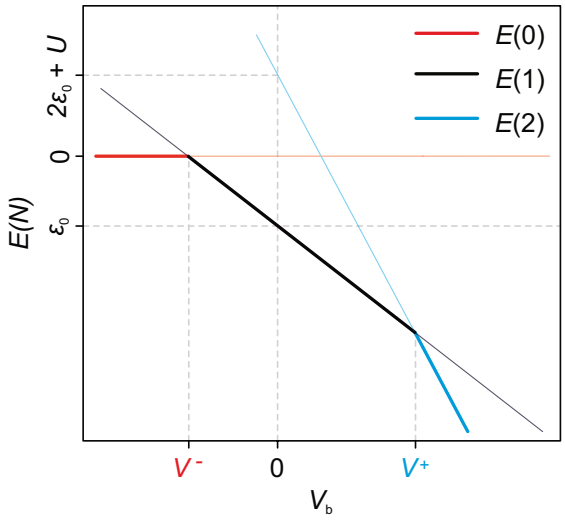

Figure 4.13: Energy diagram of the QD's accessible charge states in the PC model. The electrostatic energy of the QD in the electric field is proportional to V_b and the proportionality constant changes depending on the electron number N [see Eqs. 4.26(a–c)]. Again the bold lines represent the favoured charge state at that particular bias voltage; note the similarity to Fig. 4.8(b). Here, the N-independent constant offset to the energies, present in Fig. 4.8(b), has been set to zero for simplicity.

$$E(0) = 0 \tag{4.26a}$$

$$E(1) = \varepsilon_0 - \alpha e V_\mathrm{b} \tag{4.26b}$$

$$E(2) = 2\varepsilon_0 + U - 2\alpha e V_\mathrm{b} \ , \tag{4.26c}$$

where the z dependence of α is implicit.

Voltage at the charging features

Eqs. 4.26(a–c) are visualized in Fig. 4.13 as functions of V_b; note the similarity to Fig. 4.8(b). As discussed, the lowest energy state at zero bias is $E(1)$. Since the system will always be in the state of least energy, at the intersections between $E(1)$

and $E(0)$ and $E(2)$ the charge state will be changed — the bold lines indicate which state the QD is in, dependent on V_b. The voltages at which these changes in charge state occur are simply $V^\pm$, the voltage values at which the frequency shift dips are observed. ε_0 and U are also graphically defined in the y-intercepts of the QD's energies. As in Sec. 4.1.3 we can deduce the voltages at which the charge transitions occur by equating the respective equations from Eqs. 4.26(a–c):

$$\begin{aligned} E(1,\ V^-) &= E(0,\ V^-) \\ \varepsilon_0 - \alpha e V^- &= 0 \\ V^- &= \frac{\varepsilon_0}{e\alpha} \end{aligned} \tag{4.27a}$$

Again performing the same analysis for V^+:

$$\begin{aligned} E(1,\ V^+) &= E(2,\ V^+) \\ \varepsilon_0 - \alpha e V^+ &= 2\varepsilon_0 + U - 2\alpha e V^+ \\ V^+ &= \frac{\varepsilon_0 + U}{e\alpha} \end{aligned} \tag{4.27b}$$

Eqs. 4.27(a–b) show us that if we can access α, we can utilize the experimental values of $V^\pm$ to obtain ε_0 and U.

Force in the point charge model

The PC model can also provide us with expressions for the change in tip-sample force at a charge state transition $\Delta F^\pm_{\text{t-s}}(z)$. Although the overall force acting between tip and sample has several contributions, $\Delta F^\pm_{\text{t-s}}(z)$ stem solely from the modified electrostatic interaction due to the change in charge state of the QD. For this reason we can use the energies described in Eqs. 4.26(a–c) to predict $\Delta F^\pm_{\text{t-s}}(z)$. To this end we assert that

$$\Delta F^\pm_{\text{t-s}}(z) = \left[-\frac{\partial E(1 \pm 1)}{\partial z}(z) + \frac{\partial E(1)}{\partial z}(z) \right] \Bigg|_{V^\pm} \tag{4.28}$$

The only ostensible z-dependence in Eqs. 4.26(a–c) is $\alpha(z)$. However in principle the binding energy ε_0 and Coulomb repulsion U can also change with z, due to the change

in image charge interactions with the surface. For this reason the differentiation is performed allowing ε_0 and U to be functions of z:

$$\begin{aligned}\Delta F^{-}_{\text{t-s}} &= \left[-\frac{\partial E(0)}{dz}(z) + \frac{\partial E(1)}{dz}(z)\right]\Big|_{V^-} \\ &= 0 - \frac{\partial \alpha}{\partial z} eV^- + \frac{\partial \varepsilon_0}{\partial z} \\ &= -\frac{\partial \alpha}{\partial z}\frac{\varepsilon_0}{\alpha} + \frac{\partial \varepsilon_0}{\partial z} \qquad (4.29a)\end{aligned}$$

$$\begin{aligned}\&\qquad \Delta F^{+}_{\text{t-s}} &= \left[-\frac{\partial E(2)}{\partial z}(z) + \frac{\partial E(1)}{\partial z}(z)\right]\Big|_{V^+} \\ &= 2\frac{\partial \alpha}{\partial z} eV^+ - 2\frac{\partial \varepsilon_0}{\partial z} - \frac{\partial U}{\partial z} - \frac{\partial \alpha}{\partial z} eV^+ + \frac{\partial \varepsilon_0}{\partial z} \\ &= \frac{\partial \alpha}{\partial z}\frac{\varepsilon_0 + U}{\alpha} - \frac{\partial \varepsilon_0}{\partial z} - \frac{\partial U}{\partial z} \qquad (4.29b)\end{aligned}$$

As before, we compute the derivatives of Eqs. 4.27(a–b):

$$\frac{\partial V^-}{\partial z} = \frac{1}{e\alpha}\left(-\frac{\partial \alpha}{\partial z}\frac{\varepsilon_0}{\alpha} + \frac{\partial \varepsilon_0}{\partial z}\right) \qquad (4.30a)$$

$$\frac{\partial V^+}{\partial z} = \frac{-1}{e\alpha}\left(\frac{\partial \alpha}{\partial z}\frac{U + \varepsilon_0}{\alpha} - \frac{\partial \varepsilon_0}{\partial z} - \frac{\partial U}{\partial z}\right) \qquad (4.30b)$$

Comparing these equations to Eqs. 4.29(a–b):

$$\begin{aligned}\frac{\partial V^{\pm}}{\partial z} &= \mp \frac{\Delta F^{\pm}_{\text{t-s}}}{e\alpha} \\ \alpha &= \mp \frac{\Delta F^{\pm}_{\text{t-s}}}{e\frac{\partial V^{\pm}}{\partial z}} \qquad (4.31)\end{aligned}$$

This equation, identical to Eq. 4.23, remarkably shows us that the SEB and PC models are, in their predictions of the charging features, entirely equivalent. This equivalence became apparent from the comparison between Fig. 4.8(b) and Fig. 4.13 — the PC model is in fact a 'linearized' version of the SEB model. However because of this, the PC model in this form also fails to account for the discrepancy in α (see Fig. 4.12). As mentioned in the previous section, it is likely that the discrepancy stems from an N-dependence in α. In the following section we therefore investigate an extension of the point charge model to account for this.

4.2.2. Discrepancy in α

We begin by modifying Eqs. 4.26(a–c) for the general case, where $\alpha = \alpha(N)$ and $E_1 \neq E_2$, i.e. $\varepsilon_0(1) \neq \varepsilon_0(2)$:

$$E'(0) = 0 \tag{4.32a}$$
$$E'(1) = \varepsilon_0(1) - \alpha(1)eV_\mathrm{b} \tag{4.32b}$$
$$E'(2) = \varepsilon_0(1) + \varepsilon_0(2) + U - 2\alpha(2)eV_\mathrm{b} \tag{4.32c}$$

Determining $V^\pm$ from these equations:

$$\begin{aligned} E'(1,\ V^-) &= E'(0,\ V^-) \\ \varepsilon_0(1) - \alpha(1)eV^- &= 0 \\ V^- &= \frac{\varepsilon_0(1)}{e\alpha(1)} \end{aligned} \tag{4.33a}$$

$$\begin{aligned} \&\qquad E'(1,\ V^+) &= E'(2,\ V^+) \\ \varepsilon_0(1) - \alpha(1)eV^+ &= \varepsilon_0(1) + \varepsilon_0(2) + U - 2\alpha(2)eV^+ \\ V^+ &= \frac{\varepsilon_0(2) + U}{e[2\alpha(2) - \alpha(1)]} \end{aligned} \tag{4.33b}$$

Utilizing Eq. 4.28 we can again determine expressions for the change in tip-sample force at the charging features:

$$\begin{aligned} \Delta F^-_{\text{t-s}} &= \left[-\frac{\partial E'(0)}{\partial z} + \frac{\partial E'(1)}{\partial z}\right]\Bigg|_{V^-} \\ &= 0 - \frac{\partial \alpha(1)}{\partial z} eV^- + \frac{\partial \varepsilon_0(1)}{\partial z} \\ &= -\frac{\partial \alpha(1)}{\partial z}\frac{\varepsilon_0(1)}{\alpha(1)} + \frac{\partial \varepsilon_0(1)}{\partial z} \end{aligned} \tag{4.34a}$$

$$\begin{aligned} \&\qquad \Delta F^+_{\text{t-s}} &= \left[-\frac{\partial E'(2)}{\partial z} + \frac{\partial E'(1)}{\partial z}\right]\Bigg|_{V^+} \\ &= 2\frac{\partial \alpha(2)}{\partial z} eV^+ - \frac{\partial \varepsilon_0(1)}{\partial z} - \frac{\partial \varepsilon_0(2)}{\partial z} - \frac{\partial U}{\partial z} - \frac{\partial \alpha(1)}{\partial z} eV^+ + \frac{\partial \varepsilon_0(1)}{\partial z} \\ &= \left[2\frac{\partial \alpha(2)}{\partial z} - \frac{\partial \alpha(1)}{\partial z}\right]\frac{\varepsilon_0(2) + U}{e[2\alpha(2) - \alpha(1)]} - \frac{\partial \varepsilon_0(2)}{\partial z} - \frac{\partial U}{\partial z} \end{aligned} \tag{4.34b}$$

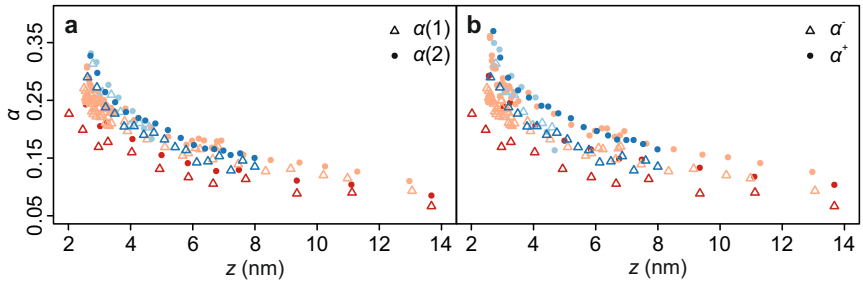

Figure 4.14: (a) $\alpha(2)$ and $\alpha(1)$, determined with Eqs. 4.36(a–b). Interestingly, compared with (b) (taken from Fig. 4.12), the two sets of points for each dataset are closer together, meaning that the discrepancy in α may not be as large as Fig. 4.12 suggests. However a systematic difference between the two branches $[\alpha(2) > \alpha(1)]$ still remains.

As before we can calculate the spatial derivatives of Eqs. 4.33(a–b):

$$\frac{\partial V^-}{\partial z} = \frac{1}{e\alpha(1)}\left[-\frac{\partial \alpha(1)}{\partial z}\frac{\varepsilon_0(1)}{\alpha(1)} + \frac{\partial \varepsilon_0(1)}{\partial z}\right] \tag{4.35a}$$

$$\frac{\partial V^+}{\partial z} = -\frac{1}{e[2\alpha(2)-\alpha(1)]}\left\{\left[2\frac{\partial \alpha(2)}{\partial z} - \frac{\partial \alpha(1)}{\partial z}\right]\frac{\varepsilon_0(2)+U}{e[2\alpha(2)-\alpha(1)]} - \frac{\partial \varepsilon_0(2)}{\partial z} - \frac{\partial U}{\partial z}\right\} \tag{4.35b}$$

Finally, we again notice a correspondence between Eqs. 4.34(a–b) and Eqs. 4.35(a–b):

$$\Delta F^-_{\text{t-s}} = e\alpha(1)\frac{\partial V^-}{\partial z} \tag{4.36a}$$

$$\Delta F^+_{\text{t-s}} = -2\alpha(2)e\frac{\partial V^+}{\partial z} + \alpha(1)e\frac{\partial V^+}{\partial z} \tag{4.36b}$$

Hence we again arrive at a system of 4 equations:

$$
\begin{aligned}
V^- &= \frac{\varepsilon_0(1)}{e\alpha(1)} \\
V^+ &= \frac{\varepsilon_0(2)+U}{e[2\alpha(2)-\alpha(1)]} \\
\Delta F^- &= e\alpha(1)\frac{\partial V^-}{\partial z} \\
\Delta F^+ &= -2\alpha(2)e\frac{\partial V^+}{\partial z} + \alpha(1)e\frac{\partial V^+}{\partial z}
\end{aligned}
$$

This system of equations can be solved for the model parameters $\alpha(1)$, $\alpha(2)$, $\epsilon_0(1)$ and $\epsilon_0(2)+U$:

$$\alpha(1) = \frac{1}{e}\frac{\Delta F^-_{\text{t-s}}}{\frac{\partial V^-}{\partial z}} \tag{4.37}$$

$$\alpha(2) = \frac{1}{2e}\left[\frac{\Delta F^-_{\text{t-s}}}{\frac{\partial V^-}{\partial z}} - \frac{\Delta F^+_{\text{t-s}}}{\frac{\partial V^+}{\partial z}}\right] \tag{4.38}$$

$$\epsilon_0(1) = V^+\frac{\Delta F^-_{\text{t-s}}}{\frac{\partial V^-}{\partial z}} \tag{4.39}$$

$$\epsilon_0(2)+U = V^-\frac{\Delta F^+_{\text{t-s}}}{\frac{\partial V^+}{\partial z}} \tag{4.40}$$

Fig. 4.14(a) shows Eqs. 4.37–4.38 plotted as functions of z. Note that for all datasets $\alpha(2) > \alpha(1)$ by a constant factor of approximately 0.01. Intriguingly, $\alpha(2)$ is closer to $\alpha(1)$ than the two branches of α in Fig. 4.12. The physical significance of this observation can be seen in the framework of the SEB model. In Fig. 4.15(a) we have plotted the total charges on the capacitor plates according to Eqs. 4.4 and 4.6 for the cases $N = 0$, $N = 1$, and $N = 2$, and in Fig. 4.15(b) the corresponding voltages V_{t} and V_{g} [Eqs. 4.11(a–b)] are shown. For $N = 0$, only the polarization charges $\pm V_{\text{b}}C_{\text{series}}$ are present, where $C_{\text{series}} = \frac{C_{\text{t}}C_{\text{g}}}{C_{\text{t}}+C_{\text{g}}}$ is the total capacitance of the gate and tip capacitor in series. As soon as charge is present on the QD [shown in orange in Fig. 4.15(a)], it moves to the surfaces of the QD (the inner plates), from where it induces screening charges on tip and the substrate surface [shown in teal in Fig. 4.15(a)]. Note that the sum of the surfaces charges on the QD is $-Ne$, as it must be according to Eqs. 4.6. Comparing the cases $N = 1$ and $N = 2$, Fig. 4.15(a) shows that if two electrons are present on the QD, the per-electron screening charge in the

substrate surface is larger than when only one electron is present [$\alpha(2) > \alpha(1)$]. In other words, for the doubly charged QD the charges move away from the tip. While such a movement is intuitively clear from the strong confinement of the charges in the nanoscale quantum dot, formally this is a consequence of a decreased tip capacitance relative to the gate capacitance when $N = 2$. As Fig. 4.15(b) shows, this corresponds to a larger voltage drop over the tip-QD bond, since less screening takes place there. In the following section we present an explanation for this possible N-dependence based on the breakdown of Koopmans' approximation, where the geometry of the QD is no longer fixed.

Non-rigid QD

So far in this chapter we have considered a 'rigid' QD, i.e. the confinement potential of the QD is independent of its electron population. However it is conceivable that when interelectronic repulsion is strong, e.g. in few electron structures, this potential could be affected. This modification was discussed as a 'contraction correction' to orbital energies by Koopmans in his seminal work [108], and later mentioned in several investigations of small QDs [70, 81, 102, 109, 110]. In this section we show how a modification of this kind could explain the N-dependence of α we may be observing in experiment.

Fig. 4.16(a) illustrates the situation. The repulsion between the first and second electrons on the QD causes the confinement potential, or orbital shape, to change, as discussed in connection with Fig. 4.15. Assuming for simplicity a spherical orbital, the mean positions of the electrons move away from the tip as the size of the orbital increases, leading to an increased value of α. Note that since the orbital size has increased U is also lower than it otherwise would be and that $\varepsilon_0(2) > \varepsilon_0(1)$.

Eqs. 4.32(a–c) are the applicable energy equations here, and Eqs. 4.36(a–b) describe the difference in α depending on the electron population of the QD. However by applying several simplifying approximations, we can relate $\alpha(1)$ and $\alpha(2)$ to each other and gain further physical insight. We define $\alpha(1) = \alpha(z,\ x)$, where x is the mean distance between the electrons on the QD and the tip, as shown in Fig. 4.16(a). If x is changed by a small amount Δx as in Fig. 4.16(a), α becomes $\alpha(2) = \alpha(z,\ x + \Delta x)$. We perform a Taylor expansion:

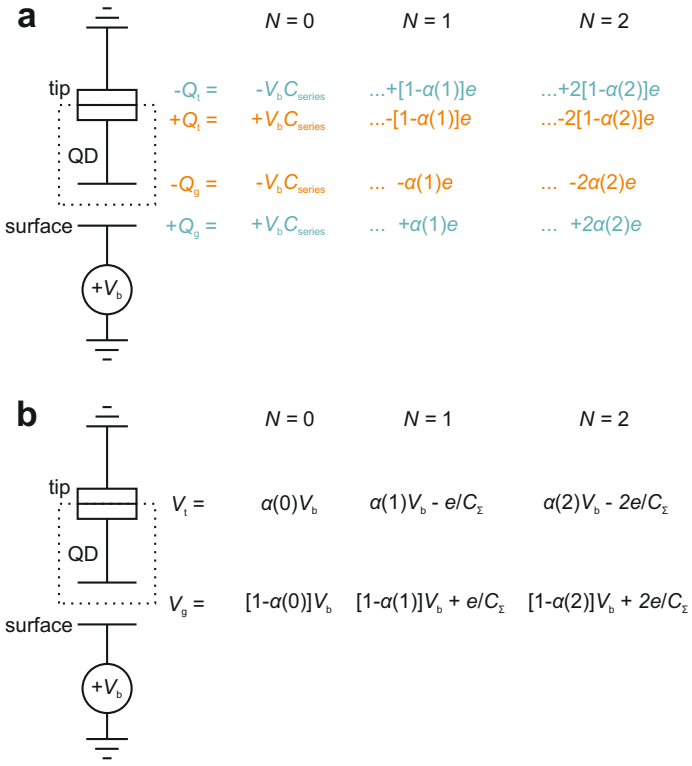

Figure 4.15: The charges and voltage drops in the junction as functions of N. In (a) the polarization charges of the two capacitors are shown; the additional charge on the surface of the QD when $N = 1$ or $N = 2$ is shown in orange and the induced charge on the tip and surface when $N = 1$ or $N = 2$ in teal. In (b) the voltage drops in the tip and gate capacitors are displayed. Since $\alpha(2) > \alpha(1)$ [see Fig. 4.14(a)], the figure shows that the induced screening charge per electron is larger for $N = 2$ than that when $N = 1$.

$$\alpha(z,\ x + \Delta x) \simeq \alpha(z,\ x) + \left(\frac{\partial \alpha}{\partial x}\right)_z \Delta x$$
$$\Delta x \simeq \frac{\alpha(2) - \alpha(1)}{\left(\frac{\partial \alpha}{\partial x}\right)_z} \tag{4.41}$$

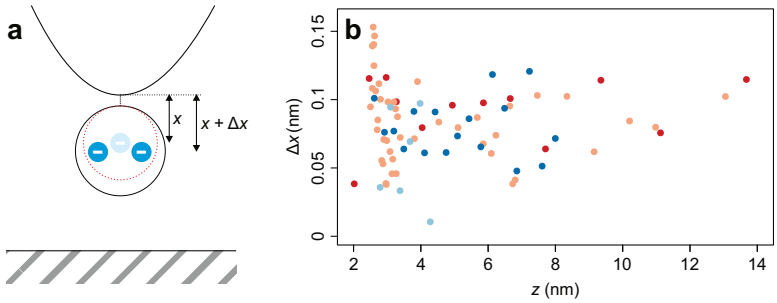

Figure 4.16: An explanation for the measured discrepancy in α. (a) Sketch of how a breakdown in Koopmans' approximation can explain the discrepancy. Adding the second electron to the QD alters the confinement potential of the QD, leading to a modified mean distance between the electrons and the tip. (b) Δx as determined from Eq. 4.41. Its value is seen to be essentially constant across the experimental distance range in all datasets.

We can therefore determine Δx using $\alpha(2)$ and $\alpha(1)$ from experiment. Performing a straight line fit on the logarithm of the data shown in Fig. 4.14, one sees that $\alpha(1) \propto z^{-y}$, where $y = 0.5 \pm 0.1$ for the four datasets. As an approximation, we thus assume that $\alpha \propto 1/\sqrt{z}$. However α is also dependent on x. When it comes to the form of α, we have three boundary conditions: (1) $\alpha \to 0$ as $z \to \infty$, (2) $\alpha \to 0$ as $x \to 0$ and (3) $\alpha \to 1$ as $z \to x$. Considering these conditions, we come to

$$\alpha(z,\ x) = \sqrt{\frac{x}{z}} \tag{4.42}$$

$$\& \qquad \frac{\partial \alpha}{\partial x}(z,\ x) = \frac{1}{2\sqrt{xz}}. \tag{4.43}$$

Naturally we have no experimental access to x, however for the set of experiments in Sec. 3.1 x was determined to be 0.7 nm. Fig. 4.16(b) displays the result of Eq. 4.41, plotted using Eqs. 4.36(a–b) and Eq. 4.43 with $x = 0.7$ nm. Δx is seen to take on a similar value across the datasets between 0.05 and 0.15 nm. This value is a small fraction of the size of the QD and could be a realistic approximation for the change in electronic structure of the QD upon a change in charge state. The detection of a possible breakdown in Koopmans' approximation is highly interesting and certainly merits future investigation.

4.2.3. Energy level position and Coulomb repulsion

As mentioned in Sec. 4.2.1, with knowledge of α we can reconstruct ε_0 and U. Utilizing Eqs. 4.33(a–b) and Eqs. 4.36(a–b):

$$\varepsilon_0(1) = \frac{\Delta F^{-}_{\text{t-s}}}{\frac{dV^-}{dz}} V^- \tag{4.44}$$

$$U = -\frac{\Delta F^{+}_{\text{t-s}}}{\frac{dV^+}{dz}} V^+ - \varepsilon_0(2) \tag{4.45}$$

Although an explanation where $\alpha = \alpha(N)$ has been shown to be more viable than $\alpha = \text{const.}$, it can be seen from Eqs. 4.44–4.45 that $\varepsilon_0(2)$ and U are in this case not uniquely determinable. Fig. 4.17(a) displays $\varepsilon_0(2) + U$ as according to Eq. 4.45 and Fig. 4.17(b) displays $\varepsilon_0(1)$ from Eq. 4.44, which represents the energy of the LUMO of the molecular QD relative to the Fermi level of the tip. For all four datasets $\varepsilon_0(1)$ was between -0.15 eV and -0.3 eV. There also appears to be a slight tendency towards more negative binding energies as the surface is approached, which can be expected as the surface image charge attraction increases [111]. The trend is however weak and may simply be experimental noise. However from our data we cannot distinguish $\varepsilon_0(2)$ and U. Nevertheless, if we assume that $\varepsilon_0(1) = \varepsilon_0(2)$, Eqs. 4.44–4.45 become identical to those derived in the case of constant α. While the use of a uniform ε_0 as opposed to $\varepsilon_0(N)$ may lead to an uncertainty in U of several hundred millielectronvolts, we nevertheless proceed with this assumption, since from it we can gain further insights into the behaviour of U.

In Fig. 4.18(a) we see a plot of the intramolecular Coulomb repulsion U between two electrons on the QD according to Eqs. 4.44–4.45 with $\varepsilon_0(1) = \varepsilon_0(2)$. Intriguingly, U displays a slight increase close to the surface, which is very unlikely since the screening effect of the surface should lead to a lower value of U. As mentioned in the previous section, if the Koopmans breakdown were to be implemented, the resulting single particle energy of the electrons in the doubly filled orbital $\varepsilon_0(2)$ would be higher than that in a singly occupied orbital $\varepsilon_0(1)$. This would have the effect of reducing U, possibly by several hundred meV [as exemplified in Fig. 4.17(a)]. While this point of contention increases the uncertainty on the accuracy of the values of U, the dependence of U on z would be unlikely to change, since $\varepsilon_0(2)$ would have a similar z-dependence to $\varepsilon_0(1)$.

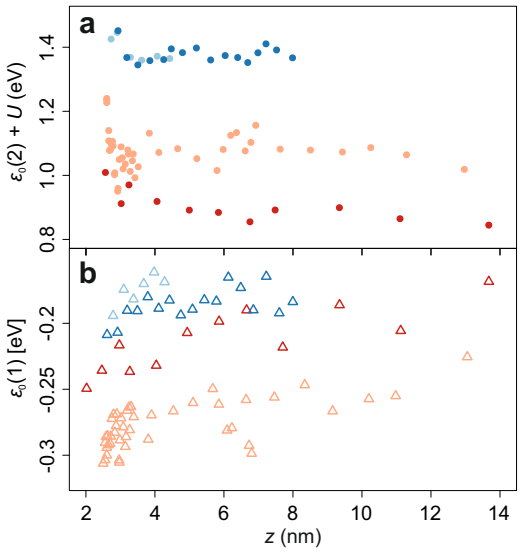

Figure 4.17: $\varepsilon_0(1)$ and $\varepsilon_0(2) + U$ as determined from Eqs. 4.44–4.45. $\varepsilon_0(1)$ appears to become more negative close to the surface as the orbital is stabilized further by image forces. We observe variations between experiments of up to ∼100 meV in $\varepsilon_0(1)$.

The mean value of U from the four datasets is $\sim$ 1.35 eV, which compares favourably to a value from a DFT calculation by Greuling et al. [98], where U was calculated during the retraction of the PTCDA molecule from the Ag(111) surface ($U \geq 1.4$ eV). Our measured value of U is also significantly smaller than the gas phase PTCDA value of 3 eV quoted in [98], indicating the strong screening effect of the metal tip. Both ε_0 and U display scattering of several hundred millielectronvolts between datasets, again most likely due to differing tip structures and therefore screening and adsorption characteristics. This is an interesting finding in itself, since it reveals the range in which changes of the precise geometry affect the model parameters ε_0 and U.

In this section we have exhibited an intuitive approach to modelling the single electron charging events present in our experiment that does not require any fit parameters to extract the desired information from the data. We also showed the remarkable fact that the SEB and PC models are fully equivalent in their predictions

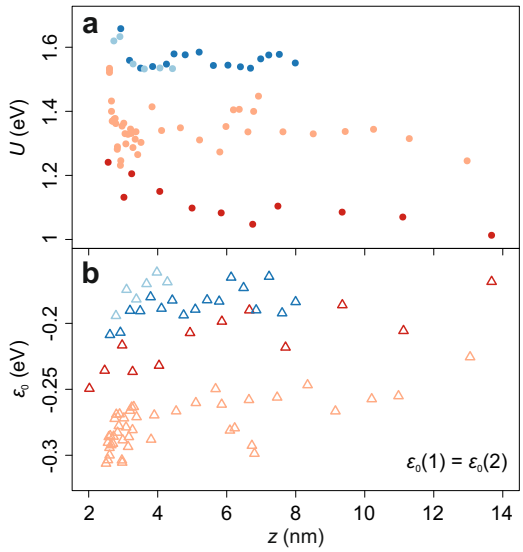

Figure 4.18: ε_0 and U as determined from Eqs. 4.44–4.45 with $\varepsilon_0(1) = \varepsilon_0(2)$. Across the distance range accessible in experiment, U remains at essentially a constant value. There is a hint of a slight upturn in U close to the surface, which would be highly surprising since the renormalization due to surface screening should in fact lower U. We observe variations in U of several hundred millielectronvolts between experiments. U is significantly smaller than the gas phase value for PTCDA of 3 eV given by Greuling et al. [98] due to the screening effect of the metallic tip.

of α. In the following discussion we continue the comparison between the models in order to gain further insights into the results from both models.

4.3. Discussion

The most natural starting point for a comparison between the SEB and the PC models is at their energy equations. The free energy in the SEB is calculated as

$$E_{\mathrm{SEB}}(N) = \sum_{n=0}^{N} E_{\mathrm{n}} + \frac{Q_{\mathrm{t}}^2}{2C_{\mathrm{t}}} + \frac{Q_{\mathrm{g}}^2}{2C_{\mathrm{g}}} - W(N).$$

Here

$$\frac{Q_{\mathrm{t}}^2}{2C_{\mathrm{t}}} + \frac{Q_{\mathrm{g}}^2}{2C_{\mathrm{g}}} = E_{\mathrm{el}}(N)$$

is the electrical energy of the charged tip and gate capacitors and $W(N) = V_{\mathrm{b}}Q_{\mathrm{g}}$ the work done by the voltage source to charge them. As shown in Eq. 4.10, this is equivalent to

$$E_{\mathrm{SEB}}(N) = \sum_{n=0}^{N} E_{\mathrm{n}} + \frac{(Ne)^2}{2C_\Sigma} - Ne\frac{C_{\mathrm{g}}}{C_\Sigma}V_{\mathrm{b}} - \frac{C_{\mathrm{t}}C_{\mathrm{g}}V_{\mathrm{b}}^2}{2C_\Sigma}. \tag{4.46}$$

This can be compared to the energy expression for the QD in the point charge model

$$E_{\mathrm{PC}}(N) = \sum_{n=0}^{N} E_{\mathrm{n}} + E_{\mathrm{r}}(N) - Ne\alpha V_{\mathrm{b}}. \tag{4.47}$$

The first terms in Eqs. 4.46–4.47 are clearly equivalent. The second term in Eq. 4.47 represents the electrostatic energy of the QD due to the Coulomb repulsion between the electrons. We notice that this is precisely what the second term in Eq. 4.46 also represents, i.e. $E_{\mathrm{r}}(N) = \frac{(Ne)^2}{2C_\Sigma}$. This can be seen in the following argument. The chemical potential specifies the change in internal energy when one particle is added to the system, keeping entropy and volume constant. According to Eq. 4.13, this is given by

$$\mu(N) = E_{\mathrm{N}} + \frac{(N - \frac{1}{2})e^2}{C_\Sigma} - e\alpha V_{\mathrm{b}}.$$

Clearly, only the second term originates from interparticle repulsions. Since each new electron on the quantum dot is repelled by all existing ones, this term is essentially linear in N. The total repulsion energy is obtained by integrating this repulsion term over N:

$$\begin{aligned} E_{\mathrm{r}}(N) &= \int_0^N \frac{(n-1/2)e^2}{C_\Sigma}\mathrm{d}n \\ &= \frac{(Ne)^2}{2C_\Sigma} - \frac{Ne^2}{2C_\Sigma}. \end{aligned} \tag{4.48}$$

In the thermodynamic limit, i.e. for $N \to \infty$, we can ignore the second term. We will do this for now and turn back to it at the end of the chapter. The third terms in Eqs. 4.46–4.47 are also equivalent, since as shown in Eq. 4.12, $\alpha = C_{\mathrm{g}}/C_\Sigma$. Hereafter we refer to these terms as field terms $E_{\mathrm{field}} = -Ne\frac{C_{\mathrm{g}}}{C_\Sigma}V_{\mathrm{b}}$. Thus the only ostensible difference between the two models appears in the fourth term of Eq. 4.46, since Eq. 4.47 only contains three terms. We recognize this term as a subtraction of the energy stored in the equivalent series capacitor C_{series} of C_{t} and C_{g} at V_{b}:

$$\begin{aligned} \frac{1}{C_{\mathrm{series}}} &= \frac{1}{C_{\mathrm{t}}} + \frac{1}{C_{\mathrm{g}}} \\ &= \frac{C_{\mathrm{t}} + C_{\mathrm{g}}}{C_{\mathrm{t}}C_{\mathrm{g}}} \\ C_{\mathrm{series}} &= \frac{C_{\mathrm{t}}C_{\mathrm{g}}}{C_\Sigma} \end{aligned} \tag{4.49}$$

$$\begin{aligned} \& \qquad E_{\mathrm{series}} &= \frac{1}{2}C_{\mathrm{series}}V_{\mathrm{b}}^2 \\ &= E_{\mathrm{el}}(0) \end{aligned} \tag{4.50}$$

where we have referred to E_{series} as the electrostatic energy of the uncharged ($N = 0$) system $E_{\mathrm{el}}(0)$. The two models therefore differ only by $E_{\mathrm{el}}(0)$:

$$\begin{aligned} E_{\mathrm{SEB}}(N) &= \sum_{n=0}^{N} E_{\mathrm{n}} + E_{\mathrm{el}}(N) - W(N) \\ &= \sum_{n=0}^{N} E_{\mathrm{n}} + \frac{N^2e^2}{2C_\Sigma} - Ne\frac{C_{\mathrm{g}}}{C_\Sigma}V_{\mathrm{b}} - \frac{C_{\mathrm{t}}C_{\mathrm{g}}V_{\mathrm{b}}^2}{2C_\Sigma} \\ &= \sum_{n=0}^{N} E_{\mathrm{n}} + E_{\mathrm{r}}(N) + E_{\mathrm{field}} - E_{\mathrm{el}}(0) \\ &= E_{\mathrm{PC}}(N) - E_{\mathrm{el}}(0) \end{aligned} \tag{4.51}$$

We now recast the energy equation of the PC model to illustrate the implications of this. Recognizing that from Eq. 4.9, $W(N) = -E_{\mathrm{field}} + 2E_{\mathrm{el}}(0)$, we find from Eq. 4.51:

$$
\begin{aligned}
E_{\mathrm{PC}}(N) &= E_{\mathrm{SEB}}(N) + E_{\mathrm{el}}(0) \\
&= \sum_{n=0}^{N} E_{\mathrm{n}} + E_{\mathrm{el}}(N) - W(N) + E_{\mathrm{el}}(0) \\
&= \sum_{n=0}^{N} E_{\mathrm{n}} + E_{\mathrm{el}}(N) + E_{\mathrm{field}} - 2E_{\mathrm{el}}(0) + E_{\mathrm{el}}(0) \\
&= \sum_{n=0}^{N} E_{\mathrm{n}} + [E_{\mathrm{el}}(N) - E_{\mathrm{el}}(0)] + E_{\mathrm{field}}
\end{aligned} \tag{4.52}
$$

Comparing Eq. 4.52 to Eq. 4.47, we see, rather intuitively, that the repulsion energy is $E_{\mathrm{r}}(N) = E_{\mathrm{el}}(N) - E_{\mathrm{el}}(0)$. We can understand these equations as follows: the PC model does not take the uncharged system energy into account and only includes the change in energy upon charging, i.e. E_{r}, the energy of the electrons in the electric field and the single particle energies. As such, it in fact ignores all polarization energies in the system, whereas the semi-classical SEB model includes them by construction. However, this importantly does not affect the predictions of the positions of the charging features as presented in this thesis, since we have seen in Fig. 4.8(b) that the linearized version of the SEB (which is equivalent to the PC) yields the same charging voltages as the full SEB. Nevertheless, it must be noted that polarization as such (not the polarization energy) is implicitly contained in the linearized version of the SEB and the PC model through the parameter $\alpha = {}^{C_{\mathrm{g}}}/_{C_{\Sigma}}$, because the capacitances C_{g} and C_{t} are immediate consequences of the polarizability of tip, QD and sample. This is also the reason we employed the mathematically simpler PC model to derive the expressions for $\alpha = \alpha(N)$; the PC model offers the possibility to include the effect of charging on the polarizabilities which affect the charging voltages, without having to worry about the polarization energies, irrelevant for the voltages.

There is a further, crucial difference between the models when it comes to the charging energy of the QD. Returning to Eq. 4.46 and evaluating the expression for $N = 0$, $N = 1$ and $N = 2$:

$$E_{\mathrm{SEB}}(0) = E_0 - \frac{C_\mathrm{t} C_\mathrm{g} V_\mathrm{b}^2}{2C_\Sigma} \tag{4.53a}$$

$$E_{\mathrm{SEB}}(1) = E_0 + E_1 + \frac{e^2}{2C_\Sigma} - e\alpha V_\mathrm{b} - \frac{C_\mathrm{t} C_\mathrm{g} V_\mathrm{b}^2}{2C_\Sigma} \tag{4.53b}$$

$$E_{\mathrm{SEB}}(2) = E_0 + E_1 + E_2 + \frac{4e^2}{2C_\Sigma} - 2e\alpha V_\mathrm{b} - \frac{C_\mathrm{t} C_\mathrm{g} V_\mathrm{b}^2}{2C_\Sigma} \tag{4.53c}$$

If we set $E_0 - \frac{C_\mathrm{t} C_\mathrm{g} V_\mathrm{b}^2}{2C_\Sigma} = 0$, i.e. linearize the SEB model, and $E_1 = E_2$ as before then we obtain:

$$E_{\mathrm{SEB}}(0) = 0 \tag{4.54a}$$

$$E_{\mathrm{SEB}}(1) = E_1 + \frac{e^2}{2C_\Sigma} - e\alpha V_\mathrm{b} \tag{4.54b}$$

$$\begin{aligned} E_{\mathrm{SEB}}(2) &= 2E_1 + \frac{4e^2}{2C_\Sigma} - 2e\alpha V_\mathrm{b} \\ &= 2\left(E_1 + \frac{e^2}{2C_\Sigma}\right) + \frac{e^2}{C_\Sigma} - 2e\alpha V_\mathrm{b} \end{aligned} \tag{4.54c}$$

By identifying

$$E_1 + \frac{e^2}{2C_\Sigma} \equiv \varepsilon_0 \tag{4.55}$$

$$\& \qquad \frac{e^2}{C_\Sigma} \equiv U \tag{4.56}$$

we see that the SEB energy equations [Eqs. 4.53(a–c)] are fully equivalent to the PC energy equations [Eqs. 4.26(a–c)]. Eq. 4.56 displays the intuitive result that the Coulombic charging energies of the two models are equal. However in Sec. 4.2.1 we asserted that $E_1 \equiv \varepsilon_0$, which is contradicted by Eq. 4.55. The reason for this inconsistency can be seen in Tab. 4.1. The values for $E_\mathrm{r}(N)$ in the second column follow when we make the transition from the general expressions for the PC model in Eqs. 4.25(a–c) to the ones for $N = 0$, $N = 1$, and $N = 2$ [Eqs. 4.26(a–c)]. The entries in the third column follow from Eq. 4.10 for $N = 0, 1, 2$. Given that the repulsive interaction between two electrons is e^2/C_Σ, when calculating $E_\mathrm{r}(N)$ with the formula $\frac{(Ne)^2}{2C_\Sigma}$ every electron interacts with all electrons including itself. The factor $1/2$, which

E_r	PC	SEB with $\frac{(Ne)^2}{2C_\Sigma}$	SEB with $\frac{N(N-1)e^2}{2C_\Sigma}$
$E_\mathrm{r}(0)$	0	0	0
$E_\mathrm{r}(1)$	0	$\frac{e^2}{2C_\Sigma}$	0
$E_\mathrm{r}(2)$	U	$\frac{4e^2}{2C_\Sigma}$	$\frac{e^2}{C_\Sigma}$

Table 4.1: Expressions for the electronic repulsion energy in the SEB and PC models as a function of N.

corrects for double counting, does not correct for this self-interaction. As the fourth column in Tab. 4.1. shows, there is a formulation of the SEB that avoids the self-interaction, which becomes particularly severe for small N (in the thermodynamic limit of infinite N self-interaction is clearly negligible). The expression $\frac{N(N-1)e^2}{2C_\Sigma}$ was suggested by Averin et al. [112]. It can be motivated by noticing that $\frac{N(N-1)}{2} = \binom{N}{2}$ is the number of electron pairs if the QD contains N electrons, or alternatively by starting at the expression for the chemical potential in Eq. 4.13 and integrating from zero to N, as was mentioned at the beginning of this section. Referring to Eq. 4.56, with this formulation the repulsion terms in the two models match exactly.

Conclusion and outlook

This chapter provided a comprehensive overview of the single electron box model, the conventional model employed when interpreting single electron charging, i.e. Coulomb blockade phenomena. We showed that the SEB model within the constant interaction approximation breaks down when applied to our experimental data. The alternative, intuitive point charge model was thereafter introduced and shown to be equivalent to the SEB model in its predictions of the charging features. The PC model was then extended to facilitate an explanation for the breakdown based on the premise that $\alpha = \alpha(N)$. To the best of our knowledge, the experimental evidence presented here for the breakdown of the SEB and constant interaction models in a single QD is the first of its kind, and is significant for the understanding of single electron charging effects in small molecules.

The work presented here opens opportunities for the investigation of N-dependence in such systems. It may be possible to determine capacitances that are dependent on N and utilize these in the classical electrostatic theory of the SEB; in order to do this a full quantum mechanical solution of the system could be required. If the capacitance between the QD and its environment were dependent on N, the voltage drop profile in the junction would also be dependent on N, which could help to explain the discrepancy observed between the two branches of α. This is therefore an avenue well worth exploring. However as mentioned, there are many unknown parameters in the SEB model that play a role, leading to an ambiguity which may be hard to conquer.

For this reason, developing the PC model further to account for dependence on N may prove to be the more fruitful option. Since the PC model does not express the problem in terms of capacitance, a new framework must be developed. One instance of this was introduced in this chapter with the breakdown of Koopmans' approximation. This approach does not however deal with the lack of polarization energies in the PC model. Instead, a promising idea is to allow α to be dependent on the polarizability of the molecular QD in the PC model. By allowing α, itself a result of the polarizability of the molecule, to be dependent on polarizability, we would obtain a natural N-dependence in α and would have a framework to include the polarization energies in the model. This may be the avenue to further

understanding of this particular application of the Coulomb blockade and ultimately a stepping stone to optimizing the SQDM technique.

4.A. Appendix

4.A.1. Interplay of frequency shift and tunnelling current

As we have seen in Secs. 3.2 and 3.3, it is also possible to detect the charging features with tunnelling spectroscopy. In this case a double barrier tunnel junction forms and the Coulomb blockade is lifted when the electrochemical potential of the QD is situated between that of the tip and the sample. An electron can then tunnel from the sample onto the QD and to the tip or in the opposite direction. Since the tuning fork oscillation amplitudes used are small, it is possible to acquire both tunnelling and frequency shift data simultaneously — the tunnelling current spectrum however becomes smeared. Fig. 4.A.1(a) shows $\Delta f(V_\mathrm{b},\ z = c)$ data in black with the charging feature at V^- displayed. The parabolic backgrounds of the spectra have been subtracted and the spectra vertically offset for clarity. In this dataset the data were measured down to the smallest possible z values, within the regime of tunnelling. It is important to note that measuring the V^+ charging feature near the tunnelling regime is impossible without destroying the SQDM tip — it is likely that the high current flowing through the QD destabilizes its adsorption geometry on the tip. During the four spectra close to the surface, a tunnelling current becomes detectable at the moment that the QD's charge state is changed. We also notice that as the size of the step in tunnelling current ΔI_t increases, the size of the $\Delta f(V_\mathrm{b},\ z = c)$ dip decreases.

This is quantified in Figs. 4.A.1(b–c): (b) shows the size of ΔI_t dependent on z and (c) shows the area under the frequency shift dip. The current step was fitted by a cumulative Gaussian distribution function and the area under the frequency shift dips was determined by numerical integration. A clear trend is observed: the step in tunnelling grows exponentially with decreasing z as the wave function overlap between the electronic states of the QD and surface increases. This coincides with a decrease [highlighted by the red oval in Fig. 4.A.1(c)] in the area under the dip in frequency shift. The frequency shift is related to spatial force gradient which means that the integral over voltage does not result directly in the force. For this a conversion factor between the two gating mechanisms (by changing either z or V_b) is required, which is unknown. However the area under the dip is related to the change in tip-sample force upon charging, which decreases as the size of ΔI_t increases. The

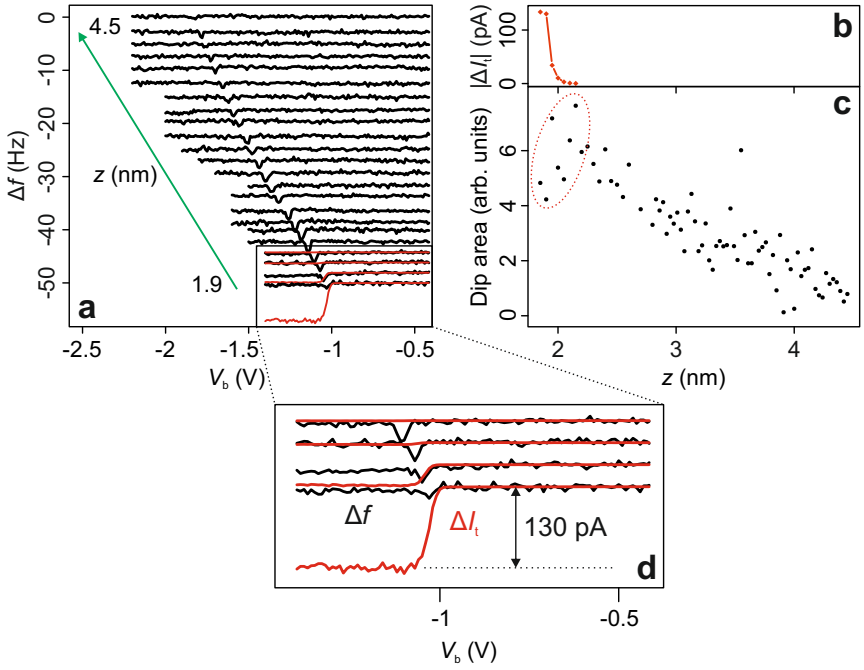

Figure 4.A.1: Interplay of frequency shift and tunnelling current. (a) Black: parabolic-background-subtracted $\Delta f(V_\mathrm{b},\ z = c)$ spectra displaying the charging feature at V^-. The range of z values is displayed. The curves are vertically shifted for clarity. Red: the step in tunnelling current ΔI_t that occurs close to the surface at V^-. The scale is arbitrary. (b) Size of ΔI_t, extracted by a cumulative Gaussian fit to the experimental data. The expected exponential increase with decreasing z is apparent. (c) The area under the $\Delta f(V_\mathrm{b},\ z = c)$ dip, integrated numerically. A decrease in the area, coinciding with the tunnelling current onset, is observed. The results of the full dataset is shown in (c), whereas (a) shows a sample for clarity. (d) Zoom of ΔI_t and corresponding $\Delta f(V_\mathrm{b},\ z = c)$ curves, with the size of the step closest to the surface displayed.

most likely explanation for this is the decrease in time spent by the electron on the QD. The electronic coupling between the states of the QD and those in the tip and surface is inversely proportional to the lifetime of electrons on the QD. The lifetime thus decreases as the surface is approached, however the probability of tunnelling increases, seen in the rise in ΔI_t. Although close to the surface more electrons hop onto the QD in unit time, it is apparent that the time integral of the QD's occupation is lower than immediately outside the tunnelling regime. This aspect of the data is intriguing and merits future investigation.

4.A.2. Determining the electronic coupling between tip and QD

In this section we discuss the coupling between the states in the QD and those in the tip. So far we have treated the charge state transitions of the QD as if they were infinitely sharp, whereas in reality the transitions are of course broadened. As discussed by Kocić et al. [82] and in Sec. 3.3, the two critical factors in the broadening are the Fermi-Dirac distribution of electrons in the tip and the lifetime broadening of the QD energy levels.

Broadening mechanisms

A change in the QD's charge state becomes possible when an energy level of the QD aligns with the Fermi level of the tip. Once the energy barrier for charging has been overcome, tunnelling to and from the QD however still remains a stochastic process. However as discussed in Sec. 4.1.1, the tunnelling rate is far larger than the time resolution of our experiment, and as such we always observe the average occupation of the QD. Fig. 4.A.2 is a schematic diagram of the tip and QD electronic states, where the i^{th} energy level of the QD is aligned with the Fermi level of the tip. The Fermi level of the tip is broadened according to Fermi-Dirac fermion statistics. The natural line shape of the QD's i^{th} electronic energy level has a Cauchy-Lorentz form, where the full width at half maximum (FWHM) is $2\Gamma_i$, Γ_i being the hybridization between the QD state i and the states in the tip. The occupation of ε_i can then be written as a convolution of these two contributions [82]:

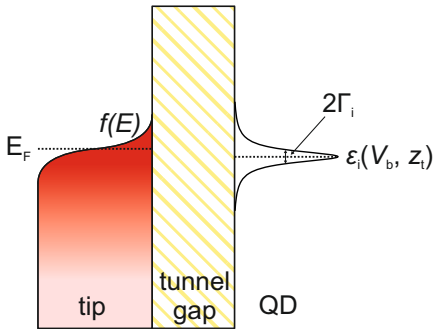

Figure 4.A.2: Energy diagram highlighting the broadening mechanisms present in the experiment. By changing the tip-sample distance or bias voltage applied to the sample, the energy level position ε_i with a natural linewidth of $2\Gamma_\mathrm{i}$ can be aligned with the temperature-broadened Fermi-Dirac distribution of electronic states in the tip. The overlap between the QD's energy level and the distribution in the tip defines the probability of the level being occupied or unoccupied.

$$n_\mathrm{i}(V_\mathrm{b}, z) = \int_{-\infty}^{\infty} f(E') \frac{\Gamma}{\pi \left\{ [E' - \varepsilon(V_\mathrm{b}, z)]^2 + \Gamma^2 \right\}} dE' \tag{4.57}$$

$$\& \qquad N(V_\mathrm{b}, z) = \sum_i n_\mathrm{i}(V_\mathrm{b}, z) \tag{4.58}$$

Note that since $n_\mathrm{i}(V_\mathrm{b}, z)$ is the probability of occupation, it can take a fractional value. By substituting Eq. 4.58 into Eq. 4.19 we obtain the full expression for tip-sample force as a function of tip-sample distance and bias voltage. The expressions show us that if a QD energy level crosses the tip's Fermi level during the tuning fork oscillation at the current (V_b, z) values, we expect a sudden change in tip-sample force.

Determining the tip-QD coupling

In order to obtain frequency shift from tip-sample force $F_\mathrm{t\text{-}s}$ a weighted average of the force over the oscillation amplitude A is necessary [42]:

$$\Delta f(V_\mathrm{b}, z) = -\frac{f_0}{2k_0} \frac{2}{\pi A^2} \int_{-A}^{A} F_\mathrm{t\text{-}s}(V_\mathrm{b}, z - z') \frac{z'}{\sqrt{A^2 - z'^2}} dz' \tag{4.59}$$

f_0 is the resonant frequency of the tuning fork and k_0 the spring constant of the tuning fork in the absence of tip-sample interactions. It is informative to express the equation in terms of the tip-sample stiffness $k_{\text{t-s}}$:

$$\Delta f(V_\text{b}, z) = \frac{f_0}{2k_0}\frac{2}{\pi A^2}\int_{-A}^{A} k_{\text{t-s}}(V_\text{b}, z - z')\sqrt{A^2 - z'^2}dz' \tag{4.60}$$

This approach avoids the singularities present in the force integral. The stiffness $k_{\text{t-s}}$ can be obtained by differentiating Eq. 4.19 with respect to distance:

$$k_{\text{t-s}} = \frac{1}{2}\frac{\partial^2 C_\text{g}}{\partial z^2}V_\text{g}^2 + \frac{\partial C_\text{g}}{\partial z}V_\text{g}\frac{\partial V_\text{g}}{\partial z} \tag{4.61}$$

The first term is simply the parabolic background of the interaction. The second term is the one critical to the charging features and has been discussed before [113, 114]: it describes the tip-sample stiffness *during* the charge state transition. At constant bias voltage and away from a charge transition, $\partial V_\text{g}/\partial z$ is close to zero and only changes minimally due to the z-dependence of C_g. If the mean electron occupation of the QD however changes during the oscillation cycle of the tuning fork, $\partial V_\text{g}/\partial z$ is no longer close to zero and the term becomes significant — it is the origin of the dips in Δf observed in experiment.

With knowledge of the relevant parameters, Eq. 4.60 makes it possible to compute Δf, both as a function of V_b and z. In the simplest model of our situation there are 6 free fit parameters: the tip-QD capacitance C_t, the distance between the QD and the surface d_g, the single particle energy E_1, the tip-QD electronic coupling Γ, and two parameters for C_g, assuming it can be expressed as a distance-dependent power law. This is unfortunately too many for an unambiguous fit, however as we saw in Sec. 4.1.5, the model in this form breaks down in any case. Nevertheless, we can still use this framework to determine the tip-QD coupling Γ, by tuning the simulation such that Γ is the only decisive parameter to the fit quality. In order to carry out the simulation we need an expression for α. For this we take a value from Fig. 4.12 and assume that α changes linearly with z within the oscillation amplitude of the tuning fork, which, since in the following example $z = 2.8$ nm and $A = 0.07$ nm, is a good approximation. The result is shown in Fig. 4.A.3 for the example of the feature at V^+, where the black curve is experimental data and red the simulation. The position of the simulated Δf dip and the size of the force step have been artificially

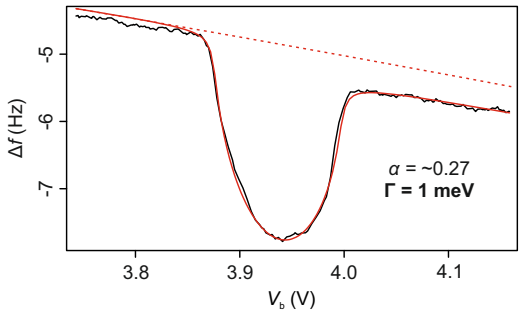

Figure 4.A.3: Determination of the tip-QD electronic coupling. Black: experimental $\Delta f(V_\mathrm{b},\ z = c)$ data, measured at $z = 2.8$ nm. Solid red: simulated $\Delta f(V_\mathrm{b},\ z = c)$ curve with $\alpha = 0.27 \pm \delta$, where δ is linearly dependent on distance and takes a maximum value of 0.005 at $\pm A$. The lineshapes match best when $\Gamma = 1$ meV (see Eq. 4.58). Dashed red: same as solid red without the change in the QD's charge state; this highlights the shift in the parabolic background due to the charge transition.

adjusted to match the data. Inputting the experimental temperature of 5 K, we obtain a best lineshape match at $\Gamma = 1$ meV. Although in Sec. 3.3 an upper limit on Γ of 0.9 meV was determined, the value obtained here is of the same order of magnitude and could differ from that in Sec. 3.3 due to differing tip-QD bonding characteristics. This analysis confirms that the electronic coupling of the QD to the tip is very weak.

5

Accurate work function changes measured with scanning quantum dot microscopy

Introduction

Einstein's seminal work on the photoelectric effect [115] was based on the idea that the energy of light was not only quantized, as Planck had hypothesized [116], but that the light itself was made up of quantized particles. These were later named photons and this in fact heralded the beginning of quantum mechanics as we now know it. Einstein confirmed experimental results of Lenard [117] with the idea that a photoelectron emitted from a body has a kinetic energy equal to the energy of the photon subtracted by an amount of work, characteristic of the body: the work function.

The work function, the minimum energy required to remove an electron from the material to the vacuum near to the surface at 0 K, is arguably the most influential property of a metal surface. It determines to a large extent how the surface interacts with its environment and other objects. The size of the work function influences, to list a few key examples, catalytic activity [118], energy level alignment [119] and organic optoelectronic properties [120]. The negative surface dipole, stemming from the exponential decay of the electronic wavefunction into the vacuum (also known as electron spillout), and the chemical potential of the electrons within the metal are the two quantities that determine the work function, therefore e.g. the surface roughness can strongly affect the work function.

In this chapter we demonstrate how SQDM can be used to measure the change in work function of a metal surface after being covered by a flat, extended surface structure. Here we briefly review the most common methods used for measuring either absolute work functions or changes in work functions and describe their strengths and weaknesses with respect to various situations. Photoemission spectroscopy (PES) can be used to directly determine the work function by noticing that the difference between the Fermi edge, where emission sets in, and the inelastic cutoff energy, where the photon energy has been exhausted, is $h\nu - \phi$, where ν is the photon frequency and ϕ the work function. The advantage of this method is the simple interpretation of the data, while the disadvantages are the lack of lateral resolution and possibility to characterize the cleanness of the surface. For example, the work function of the Ag(111) surface measured by PES has been quoted at many different values throughout the years [121–123]. Probably the most widely used technique for work-function-related measurements today is Kelvin probe force microscopy [124],

based on the contact potential difference (CPD) that exists between two metallic electrodes. When two electrodes with differing work functions are brought into electrical contact, electrons flow towards the electrode with the higher work function until equilibrium is reached and their Fermi levels are aligned. This results in surface charges on the electrodes, leading to a constant potential difference between them, referred to as the CPD. This technique has proved very successful for measuring the work function change induced by extended structures due to its high energy resolution (usually ± 20 meV) and ability to gain topographic information simultaneously. However when measuring smaller structures the macroscopic tip can affect the signal by including contributions away from the structure [125–127]. When it comes to small structures, a further method is photoelectron spectroscopy of adsorbed xenon (PAX), which utilizes the weak physisorption of Xe atoms to directly link photoemission peaks to surface potential [128]. Multiple peaks reveal different adsorption sites and corresponding local work functions and the lateral resolution is on the order of 1 nm, however there is no direct topographical information available. Another interesting method with high lateral resolution is the use of field emission resonances (FERs) within a scanning probe microscopy setup to determine local changes in work function [129–131]. Topographic information can also be used here to monitor the cleanness of the sample and the lateral resolution is also on the order of nanometres, however due to the short lifetimes of the FERs the energy resolution ($\sim$0.1 eV) is inferior to that of KPFM for example.

As we shall show, scanning quantum dot microscopy can be used to accurately determine the change in work function $\Delta\phi$ due to surface structures with an energy resolution of $\sim$10 meV. Crucially, by considering the voltage drop in the tip-sample junction we show that the knowledge of the exact shape of the tip is no longer required for a quantitative result. This leads to an effective lateral resolution of ~ 20 nm, which is weakly dependent on the tip height. This high lateral resolution is shown to be a consequence of a 'focusing' effect present in SQDM, whereby electrostatic contributions from laterally displaced surface structures are reduced by the screening effect of the tip. This measurement technique could prove especially useful for the measurement of small adsorbate islands, particularly important for nanocatalysis [132, 133] and as templates for organic electronics [134–136].

5.1. Point charge model to obtain change in work function

5.1.1. An expression for local potential

As introduced in previous chapters, an expression for the electrostatic potential of a surface nanostructure measured with SQDM can be deduced by applying the point charge model[†]:

$$E(N-1) = \sum_{n=0}^{N-1} E_\mathrm{n} + E_\mathrm{r}(N-1) - \alpha(N-1)e(V_\mathrm{b} - V_\mathrm{cpd}) - (N-1)e\Phi^* \quad (5.1a)$$

$$E(N) = \sum_{n=0}^{N} E_\mathrm{n} + E_\mathrm{r}(N) - \alpha N e(V_\mathrm{b} - V_\mathrm{cpd}) - N e\Phi^* \quad (5.1b)$$

$$E(N+1) = \sum_{n=0}^{N+1} E_\mathrm{n} + E_\mathrm{r}(N+1) - \alpha(N+1)e(V_\mathrm{b} - V_\mathrm{cpd}) - (N+1)e\Phi^* \quad (5.1c)$$

These equations are similar to Eqs. 4.25(a–c) with two differences: the inclusion of V_cpd and the Φ^* term. It is important to note that here V_cpd refers to the CPD above the clean silver surface. A change in local potential will of course affect the measured CPD, however this effect is entirely encapsulated by Φ^*. Since we again model the QD as a single point below the tip, occupied by a certain number of electrons N, the energy gain is the electronic charge Ne multiplied by the potential Φ^*. Again we substitute $N = 1$ into the equations:

$$E(0) = 0 \quad (5.2a)$$

$$E(1) = \varepsilon_0 - \alpha e(V_\mathrm{b} - V_\mathrm{cpd}) - e\Phi^* \quad (5.2b)$$

$$E(2) = 2\varepsilon_0 + U - 2\alpha e(V_\mathrm{b} - V_\mathrm{cpd}) - 2e\Phi^* \quad (5.2c)$$

Note that in this case we assume that $\alpha(1) = \alpha(2)$ and $\varepsilon_0(1) = \varepsilon_0(2)$. As discussed previously, the QD changes its average electron occupation when the energy for a

[†] We note here that the following analysis does not depend on the two charging features corresponding to the same molecular orbital. However due to our conviction that the LUMO is the orbital being (de-)populated at the two features as discussed in Sec. 4.2.1, we continue with this nomenclature.

different charge state drops below the energy of its current state. We can then solve these equations for the two possible transitions:

$$-\varepsilon_0 + \alpha e(V^- - V_{\mathrm{cpd}}) + e\Phi^* = 0 \tag{5.3a}$$

$$U + \varepsilon_0 - \alpha e(V^+ - V_{\mathrm{cpd}}) - e\Phi^* = 0 \tag{5.3b}$$

where $V^{\pm}$ take their usual meanings. We solve Eqs. 5.3(a–b) for both α and Φ^*:

$$\alpha = \frac{U}{e\Delta V} \tag{5.4}$$

$$\Phi^* = -U\frac{V^- - V_{\mathrm{cpd}}}{e\Delta V} + \frac{\varepsilon_0}{e} \tag{5.5}$$

where $\Delta V = V^+ - V^-$. Eq. 5.4 describes why the charging features shift with changing tip-sample separation; the fractional voltage drop across the tip-QD bond (α) changes while U remains essentially constant. Without performing a set of measurements to determine ε_0 and U as in the previous chapter, we cannot yet access Φ^* directly from Eq. 5.5. In any case, in the following we will in fact see that the influence of ε_0 and U is removed entirely. By setting $\Phi^* = 0$ in Eqs. 5.3(a–b), we retrieve expressions for ε_0 and U:

$$\varepsilon_0 = \alpha_0 e(V_0^- - V_{\mathrm{cpd}}) \tag{5.6}$$

$$U = \alpha_0 e(V_0^+ - V_{\mathrm{cpd}}) - \varepsilon_0 \tag{5.7}$$

where α_0, V_0^+ and V_0^- refer to the respective quantities at $\Phi^* = 0$. This can be achieved in an experiment by recording a $\Delta f(V_{\mathrm{b}},\ z_{\mathrm{t}} = c)$ spectrum such as in Fig. 4.2 at a location where the potential at the position of the QD due to any surface nanostructure is negligible. By substituting these equations into Eq. 5.5 we reach an expression for Φ^*:

$$\Phi^* = -\alpha_0\Xi = -\alpha_0\left[\frac{V^-}{\Delta V}\Delta V_0 - V_0^- + V_{\mathrm{cpd}}\left(1 - \frac{\Delta V_0}{\Delta V}\right)\right] \tag{5.8}$$

For brevity we refer to the quantity in square brackets as Ξ from this point onwards. The third, CPD-dependent term in Ξ is worth a short discussion. If the surface

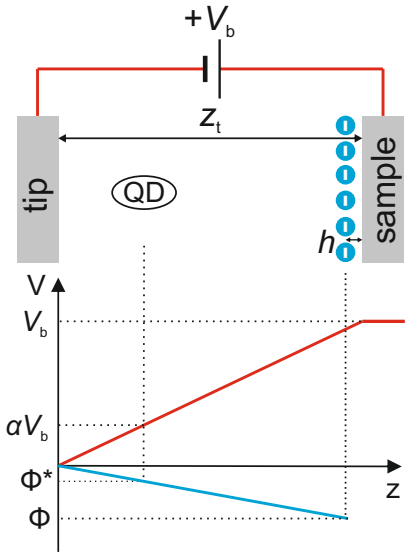

Figure 5.1: Schematic diagram of the electric potential present in the tip-QD-sample junction with an infinitely extended charge layer parallel to the surface at an adsorption height h. The QD is again treated as a single point here. The applied bias voltage V_b drops between tip and sample and the proportion of V_b that drops across the tip-QD bond is α. The potential due to the infinitely extended layer of charge Φ must also decrease to zero at the grounded tip, and we refer to the fraction of Φ that is present between tip and QD as Φ^*. From the diagram it becomes clear that when $z_\mathrm{t} \gg h$, $\alpha \simeq {}^{\Phi^*}/_{\Phi}$.

nanostructure does not change ΔV considerably from ΔV_0, then $\Delta V \simeq \Delta V_0$, this term is close to zero and the CPD does not play a large role. However if the surface nanostructure protrudes significantly from the surface, and/or appreciably alters the capacitance in the junction, then the CPD can become an important factor. In the limit of no topographical change, i.e. $\Delta V = \Delta V_0$, Eq. 5.8 condenses to $\Phi^* = -\alpha_0 \left(V^- - V_0^-\right)$; the shift of the charging features in bias voltage is solely due to Φ^*.

5.1.2. Removing the influence of the tip's properties

At this point it becomes clear that, assuming knowledge of α_0, we can reconstruct the potential Φ^*. α_0 is however *a priori* unknown, and without additional information its form would have to be estimated, for example by assuming that tip and sample are both flat and infinitely extended as in Chap. 3. Furthermore, Φ^* is not the true potential of the nanostructure, since the grounded metal tip reduces the electric potential at the position of the QD compared to what it would be in the absence of the tip. Since the exact screening properties of the tip are also inaccessible, this affects the nanostructure's potential in an unknown way and we must remove this effect to retrieve the absent-tip potential, which we call Φ. Fig. 5.1 displays the tip-QD-sample junction schematically, where a negatively-charged layer is present at a height h above the sample surface and a bias voltage V_b is applied to the sample. This diagram exhibits the example that the tip and sample are infinitely extended planes; the voltage drops linearly between them, shown in red. The fraction of bias voltage α that drops across the tip-QD bond is displayed graphically. The blue curve represents the potential due to the layer of negative charge, which in this example is also infinitely extended in the plane parallel to the surface, meaning that the potential difference between the layer and the tip is also a linear function of distance. The fraction of the potential Φ that is present at the position of the QD is simply Φ^*/Φ. As long as $z_\mathrm{t} \gg h$ we see that $\alpha_0 \simeq \Phi^*/\Phi$. The significance of this can be seen by rearranging Eq. 5.8:

$$\Phi = -\Xi \frac{\alpha_0}{\Phi^*/\Phi} \simeq -\Xi \tag{5.9}$$

In the case that $\alpha_0 \simeq \Phi^*/\Phi$, the change in surface potential due to the infinite charged layer Φ is essentially equal to the experimental quantity Ξ. It follows that by determining Ξ for a given structure, for which an infinitely extended layer is a good approximation, one can determine the change in surface potential, i.e. the change in work function due to the layer $\Delta\phi$, with high accuracy and without knowledge of the voltage drop profile or exact screening properties of the junction.

Importantly, it is noted that this is true for an infinitely extended charged layer even if the tip deviates from planar geometry. In the absence of the tip, the change in surface potential due to the charged layer is constant above the layer, since no electric field can exist in the half space above the layer. This is an equivalent effect to

applying bias voltage to the sample. The presence of the grounded tip describes the voltage drop profile in the junction, and this profile is then the same for the applied bias voltage and the infinite charged layer. It should also be noted that if the nanostructure cannot be approximated as an infinitely extended planar structure, this approach breaks down. The tip then affects the measured potential due to the nanostructure in a different way and the ratio Φ^*/Φ deviates from α_0.

5.2. Change in work function of Ag(111) after PTCDA adsorption

We choose to determine the change in work function of Ag(111) due to PTCDA adsorption, $\Delta\phi$, as a proof of concept. PTCDA molecules form self-assembled islands when deposited onto Ag(111) while accepting electronic charge from the substrate. The negatively charged molecules form a dipole layer oriented in the same direction as the pre-existing surface dipole of the metal, leading to an increase in the work function [137, 138]. There is however significant disagreement in the literature on the precise value of $\Delta\phi$ for this system, with values provided by photoemission spectroscopy as well as several DFT-based methods between -0.1 and 0.27 eV [123, 139–141]. It is likely that due to differing levels of impurities, the difficulty in detecting such impurities and the inherent averaging effect present in photoemission spectroscopy, variations in the measured work functions of the silver substrate have so far been the cause of this disagreement. In these studies the absolute values for the work function of PTCDA/Ag(111) were more narrowly spread (4.7–4.9 eV) than the work function of Ag(111) itself (4.24–4.9 eV), suggesting that exactly the above conjecture is true: surface impurities are either forced away or desorbed when PTCDA adsorbs, and the only remaining factor in the discrepancy is the flatness of the substrate. For this reason and the importance of PTCDA/Ag(111) as a prototypal system for metal-organic adsorption, it is of great interest to precisely determine $\Delta\phi$.

5.2.1. Constant height KPFM results

Before performing SQDM on the layer to determine Ξ and therefore $\Delta\phi$, we employed KPFM to provide a reference value. An STM image of a large PTCDA island is shown in Fig. 5.1(a), where an island border is visible as well as a step edge between silver terraces. We used a bare metal tip to measure $\Delta f(V_\mathrm{b},\ z_\mathrm{t} = c)$ spectra at many points and at several tip heights along the white line in Fig. 5.1(a) to determine the change in V_cpd (see Fig. 4.2) going from Ag(111) to PTCDA/Ag(111). The spectra were measured in constant height mode, where the tip height was set by adding an additional Δz_t to the height defined by the tunnelling setpoint of 50 pA and 0.35 V. The results are shown in Fig. 5.1(b). The spectra were measured at four

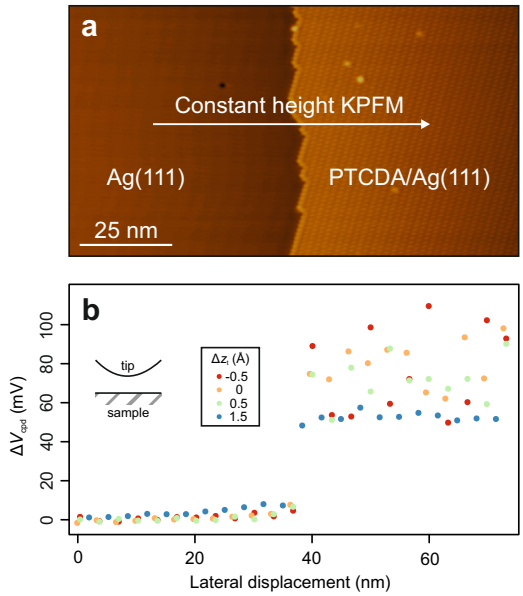

Figure 5.1: Constant height KPFM of PTCDA/Ag(111). (a) An STM image of a self-assembled PTCDA monolayer adsorbed on Ag(111), recorded at 50 pA and 0.35 V. The white line signifies where the KPFM spectra were measured. (b) The change in V_{cpd} from KPFM spectra measured along the white line in (a), taken with a clean metal tip. Δz_{t} refers to the vertical offset added to z_{t}, which was defined by the tunnelling parameters in (a). A strong distance dependence is observed and local tip-sample interactions distort the signal close to the surface.

different distances Δz_{t} from the tunnelling setpoint, represented by different colours. We observe a strong distance dependence whereby the signal quickly diminishes with increasing tip height. This effect is inherent to the KPFM technique; the decay rate of electrostatic forces means that with increasing distance, an ever larger portion of the tip plays a role in the CPD [94, 126, 127]. It is however surprising that changes of only a few ångströms induce such a large effect considering that the island is several hundred nanometres in width. This in fact suggests that the section of the tip that determines the CPD is very broad, since parts of the sample surface away from the PTCDA layer become relevant to the CPD as the tip-sample separation increases. It is therefore also unclear if the value of $\Delta\phi$ retrieved from

this measurement corresponds to the true shift induced by the molecular layer. The effect of coming too close to the surface is also apparent in the data - large local variations in the measured potential, likely due to tip-sample interactions, reduce the method's ability to deliver a reliable result. Nevertheless, the data allow us to set a lower limit on the value of $\Delta\phi$ of $\sim$80 mV.

5.2.2. SQDM results

The SQDM experiments were set up by functionalizing the tip of the nc-AFM/STM with a single PTCDA molecule using single molecule manipulation, as described in Secs. 2.1, 3.1 and 3.3. $\Delta f(V_\mathrm{b},\ z_\mathrm{t} = c)$ spectra as in Fig. 4.2 were measured while moving laterally from above Ag(111) to PTCDA/Ag(111). The changes in position of $V^\pm$ were used to determine Ξ and therefore $\Delta\phi$ (see Eq. 5.8). $V_0^\pm$ values were taken from the first spectrum on the line above clean Ag(111). The striking result is displayed in Fig. 5.2. Three different datasets are exhibited, wherein spectra at five different z_t values were recorded. These datasets were recorded several months apart, with many tip forming procedures in between them, possibly leading to large variations in the mesoscopic tip structure. Remarkably, across the different datasets and tip heights, the measured value of Ξ was (145 ± 10) mV. According to Eq. 5.9, this corresponds directly to a $\Delta\phi$ value of (145 ± 10) meV. This high level of precision is astonishing since the adsorption properties of the QD on the tip that affect α_0 and Φ^*/Φ can vary strongly between experiments, and the same value of $\Delta\phi$ is nonetheless reproduced. This is a further vindication of the point charge model for SQDM developed in this thesis. Note that at the z_t values in this experiment, 3–5 nm, the adsorption height of PTCDA (2.86 Å [142]) means that the approximation that $\alpha_0 = \Phi^*/\Phi$ holds; the small uncertainty is within the random error of the experiment itself. Although experimental values for $\Delta\phi$ in the literature disagree with one another, 145 meV corresponds very well to a DFT-based study, where (150 ± 50) meV was obtained [123]. However there the LDA functional was used to determine the molecule's adsorption geometry, and although LDA performs relatively well for this system [137], its poor treatment of van der Waals interactions mean that this value is not entirely reliable.

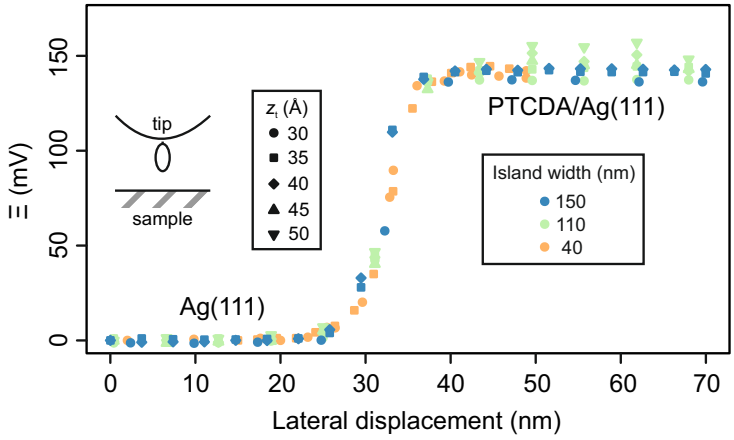

Figure 5.2: Work function change of PTCDA/Ag(111) measured with SQDM and a PTCDA QD attached to the tip. Ξ (see Eq. 5.8) from three different datasets on different PTCDA islands is displayed. From the three datasets a value for $\Delta\phi$ of PTCDA/Ag(111) of (145 ± 10) meV is obtained. Tip heights are coded by shape and molecular island size by colour.

5.2.3. Discussion

Looking at Fig. 5.2, a slight distance dependence is noticeable: Ξ in fact *increases* as a function of distance. We note that the distance dependence of the green points in Fig. 5.2 is not monotonic; random error in the SQDM experiment was responsible for a substantial proportion of the scattering. Although the distance dependence in general is marginal, it is present in all datasets and so we discuss two possible reasons for it:

(1) The approximation that $z_t \gg h$ does not hold. By visually inspecting Fig. 5.1, one can see that the ratio Φ^*/Φ will always be larger than α_0, since $h > 0$. This means that close to the surface, Ξ will be larger than Φ, overestimating the potential that is present at the position of the QD. This is opposite to the trend that we observe in the experiment, so we do not expect it to produce a large effect in the data.

(2) An artefactual distance dependence of the CPD over silver causes a distance dependence in Ξ (see Eq. 5.8). As discussed in Sec. 5.2.1, although V_{cpd} in principle has a constant value, in practice it is most often distance dependent due to the

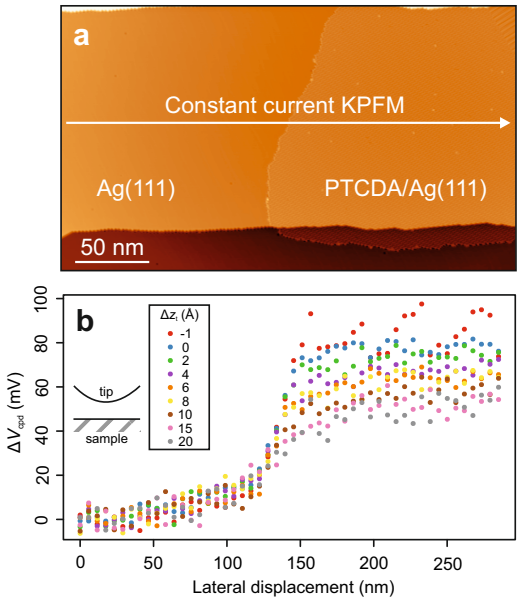

Figure 5.3: Constant current KPFM of PTCDA/Ag(111) measured with a clean metal tip. (a) An STM image of a PTCDA monolayer adsorbed on Ag(111) with a width of $\sim$150 nm, recorded at 50 pA and 0.35 V. The white line indicates where the KPFM spectra were measured. (b) Change in V_{cpd} derived from constant current KPFM spectra. The tip height was defined by the tunnelling setpoint of 50 pA and 0.35 V and an additional offset Δz_{t} by which the tip was retracted. We again obtain a $\Delta\phi$ value of $\sim$80 meV from KPFM.

contributing tip section changing with distance. To obtain Fig. 5.2 we took this into account by using the measured V_{cpd} values over silver at each tip height. It is however unlikely that the real electric field profile in the vicinity of the QD corresponds exactly to these values, since a much larger tip area corresponds to the measured V_{cpd}. Assuming that the relevant part of the CPD is more strongly affected by the tip-sample distance than the measured value would cause the slight distance dependence of Ξ in Fig. 5.2 to disappear. We therefore believe that the uncertainty over the exact electric field profile due to the CPD between tip and QD is the most plausible explanation for the perturbation of our results.

A further point for discussion is the large discrepancy between the SQDM value for $\Delta\phi$ of 145 mV and the lower limit set by KPFM of $\sim$80 mV. To understand if island size and lateral tip position played a role in the determination of $\Delta\phi$ with KPFM, we measured spectra above the largest molecular islands found on our sample. The results of constant current KPFM spectra are shown in Fig. 5.3. The spectra closest to the surface again produce a $\Delta\phi$ value of $\sim$80 meV. The measured island has a width of $\sim$150 nm and even in this case a marked distance dependence is observed in ΔV_{cpd}. Constant current operation was necessary to avoid large changes in tip height due to sample tilt; this however results in vertical lifting of the tip when above the PTCDA layer. Nevertheless, this cannot explain the $\sim$70 mV discrepancy between KPFM and SQDM present here. We are thus led to believe that our tip — a PtIr wire with a 15 µm radius, cut by focussed ion beam milling — is mesoscopically very flat, and that a very large section influences the measured CPD value. This makes our tip unsuitable for KPFM measurements of adsorbed islands where other KPFM setups perform better [94]. However the key advantage of SQDM is that it almost completely removes the influence of the mesoscopic tip and automatically provides a precise and quantitatively correct result.

Finally, we turn to the lateral resolution of the measurement. Interestingly, in the three datasets the sharpness of the step, when traversing from clean Ag(111) to the PTCDA-covered substrate, is essentially equal at $\sim$20 nm. Although our modelling approach views the QD as a point-sized object, the observed lateral resolution is intrinsically limited by the size of the QD. However since the PTCDA QD is approximately one nanometre in length, and the subnanometre resolution capability of SQDM has been demonstrated in Secs. 3.1 and 3.3, it is doubtful that this is the limiting factor in the measurement. The lateral change in the local potential itself in fact defines the sharpness of the measured step. While the analysis performed here treats the molecular monolayer as an infinitely extended plane, away from the layer in the experiment the electrostatic potential due to the layer must of course decay to zero and this is what is observed; the unscreened potential, i.e. in the absence of the tip, simply has a certain profile. However there is a third effect that in fact *increases* the lateral resolution: a 'focusing' effect stemming from the screening effect of the metallic tip. To explain this we introduce a model that considers discrete charges, rather than a layer of charge as has been discussed so far in this chapter. The reason

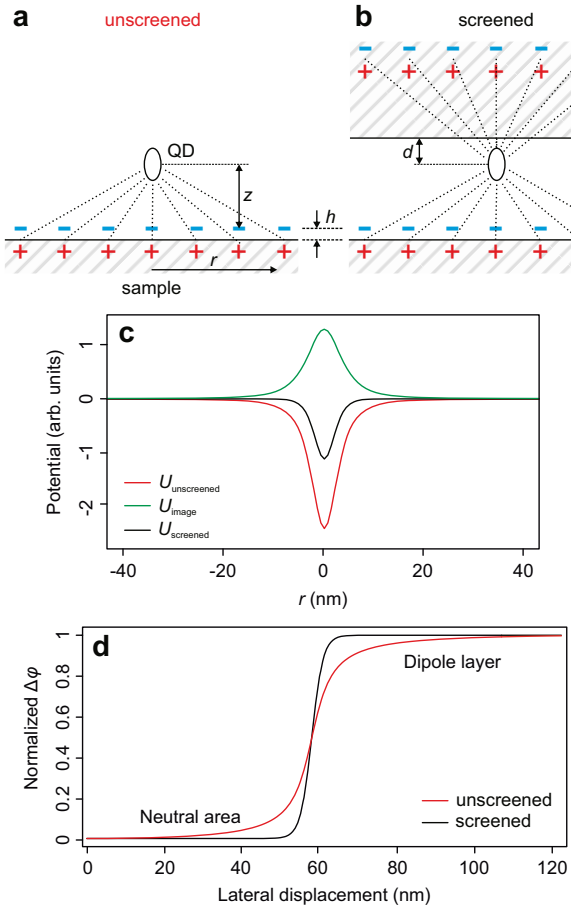

Figure 5.4: The focusing effect of SQDM. (a) Schematic diagram of free-standing QD situated above a series of point charges at a distance h above a metallic surface, induce oppositely polarized image charges in the surface. (b) Introducing the tip, modelled as a flat, infinite plane, reduces the total potential at the position of the QD due to the image potentials from tip and sample. (c) Red: the contribution to the unscreened potential at the position of the QD in (a) as a function of lateral dipole displacement. Green: the contribution to the image potential at the position of the QD in (b). Black: the sum of all potentials at the position of the QD in (b). (d) Step in potential at the position of the QD when traversing from an electrostatically neutral area to above a layer of dipoles as in (b). The screened value displays a sharper transition than the unscreened value.

for this is to utilize the method of images as shall be seen. Fig. 5.4(a) shows a free-standing QD above many point charges, located at a distance h from the sample surface. Image charges arise in the sample, which together with the original charges form dipoles. The electrostatic potential $U_{\text{unscreened}}$ at the position of the QD due to any one dipole at a vertical distance $z+h$ from the QD can be written as follows:

$$U_{\text{unscreened}} = \frac{1}{4\pi\epsilon_0}\left[-\frac{1}{\sqrt{z^2+r^2}} + \frac{1}{\sqrt{(z+2h)^2+r^2}}\right] \tag{5.10}$$

where r is the lateral displacement between the dipole and the sample position directly below the QD. The electrostatic potential at the position of the QD is dominated by the dipoles that are directly beneath it, since the contributions from more distant dipoles quickly fall towards zero as the displacement vector between QD and dipole approaches the perpendicular asymptote. The unscreened potential contribution from the dipole at r is displayed in red in Fig. 5.4(c). Fig. 5.4(b) shows the same QD and series of dipoles, with the addition of a flat, infinitely extended conductor at a distance d above the QD, representing the tip. In this case the electrostatic potential at the position of the QD is also affected by the image potential induced by the tip, as described in Secs. 3.1 and 3.3. Due to the presence of the two conducting electrodes, an infinite series of image dipoles will arise in the electrodes. In the schematic diagram of Fig. 5.4(b) we show only one set of image dipoles, however in computing the potential at the position of the QD we have considered 300 image charges in both tip and surface, a quantity determined empirically to allow the potential to converge. The image potential due to any one dipole can then be expressed as follows:

$$\begin{aligned} U_{\text{image}} = \frac{1}{4\pi\epsilon_0}\sum_{i=1}^{300}\Bigg\{ &-\frac{1}{\sqrt{(z+2iz_{\text{t}})^2+r^2}} + \frac{1}{\sqrt{(z+2h+2iz_{\text{t}})^2+r^2}} + \\ &+\frac{1}{\sqrt{[z+2d+2(i-1)z_{\text{t}}]^2+r^2}} - \frac{1}{\sqrt{[z+2h+2d+2(i-1)z_{\text{t}}]^2+r^2}}\Bigg\} \end{aligned} \tag{5.11}$$

Fig. 5.4(c) shows in green the additional potential from the 300 image charges, excluding the dipoles shown in Fig. 5.4(a), again referring to the contribution to the potential from image dipoles at the particular value of r. In black the sum of the unscreened potential $U_{\text{unscreened}}$ and the image potential U_{image} is displayed;

$U_{\text{screened}} = U_{\text{unscreened}} + U_{\text{image}}$. The presence of the tip reduces the absolute size of the potential at the position of the QD, resulting in U_{screened}, however U_{screened} decays *faster* with r than $U_{\text{unscreened}}$. $U_{\text{unscreened}}$ decays roughly as r^{-2} according to Eq. 5.10. U_{screened} on the other hand can be shown to decay roughly *exponentially* with r[†]. This surprising effect is due to the contribution of dipole potentials with opposite signs, which at larger lateral displacements cancel each other out faster than a single dipole potential would decay to zero. Fig. 5.4(d) is a simulation of a step in surface potential measured by SQDM that demonstrates this effect. The unscreened potential at the position of the QD over a step from a neutral area to a layer of dipoles is shown in red. To simulate an infinitely extended dipole layer after the step we have considered a grid of 10^4 nm^2, where dipoles with a spacing of 1 nm are squarely packed. The screened potential, the quantity measured in an SQDM experiment, is shown in black. Both potentials are normalized to their saturated value over the dipole layer. The screened potential saturates approximately 5 times faster than the unscreened potential, meaning that SQDM detects a *sharper* step than the unscreened step in potential itself. The simulated sharpness of the step is at ~ 15 nm approximately equal to the experimental sharpness of ~ 20 nm. The difference likely comes from the intrinsic SQDM resolution of ~ 1 nm as well as the approximation of the tip as a flat, infinite plane not being perfectly accurate and therefore screening the potential less effectively.

[†] There is a certain analogy here to electromagnetic radiation in waveguides — at frequencies below the waveguide's cut-off frequency, the radiation amplitude decays exponentially and cannot propagate.

Conclusion and outlook

To summarize, we have demonstrated a precise and accurate measurement of the change in work function due to a PTCDA island adsorbed on Ag(111) using SQDM. We hope that the value of $\Delta\phi = (145 \pm 10)$ meV obtained in this study goes some way to clearing up the disagreement that exists in the literature regarding this system. Although we were unable to reproduce the same value using KPFM, we believe this was largely due to our tip being suboptimally blunt for that purpose, and with an experimental setup better suited to the task we expect that the result could be improved.

Since KPFM is the most widely-used scanning probe method to determine the work function difference induced by surface structures it is natural to compare it to SQDM. The advantage of KPFM is that at the current moment it is easier to implement for most AFM setups, since there is no necessity to create an SQDM tip. However the high precision of SQDM combined with its superior energy resolution and tip-independent spatial resolution makes it in our opinion better suited to the truly quantitative analysis of nanostructures, where below a certain size KPFM is no longer able to produce quantitative results. Moreover, as shown in Sec. 5.2.3, when used to measure a step in potential, SQDM achieves a lateral resolution *better* than defined by the unscreened potential through the focusing effect of the tip's screening. A further crucial point is the fact that SQDM, when used to measure islands for which an infinitely extended plane is a good approximation, essentially removes the influence of the tip properties, and due to the focusing effect this condition is realized even for rather small structures. Achieving an experiment where the probe tip no longer influences the result is something of a holy grail in the scanning probe microscopy community, and the results presented here form one of the best realizations of this so far. It is our hope that this inherent robustness attracts further attention to the development of the technique.

The most intriguing next step will be to find the point at which the infinite plane approximation breaks down; how small is too small? What is however possible is that before this occurs, the surface potential of the small adsorbate island no longer represents the full value of the extended layer. It remains to be seen if these two cases can be distinguished from each other, since both would likely lead to a distance dependent Ξ that is larger close to the surface. Considering that the

effective smearing of the surface potential measured here was $\sim$20 nm, it could be that the second case is reached first since at an island width of 40 nm the infinite plane approximation was still intact.

Summary

This thesis has presented the creation and characterization of a single molecule device. A new microscopy method, SQDM, was developed and shown to be capable of measuring local electrostatic potential in a truly quantitative fashion. The nature of the single molecule sensor itself was investigated in-depth and unexpected results were achieved, contradicting the predictions of the highly successful orthodox theory of the Coulomb blockade.

The single molecule device was constructed with the use of atomically precise single molecule manipulation detailed in Chap. 2. Approaching the microscope tip towards a single molecule, a covalent bond was formed between the apex atom of the tip and one of the double-bonded corner oxygen atoms of the molecule. This bond was empirically found to be strong enough to remove the molecule not only from its chemisorbed state on the surface, but from its hydrogen-bonded molecular layer. The removals were made possible by the augmentation of the SPM setup with a three-dimensional motion tracking device, which was used to explore custom removal trajectories by selective variation. Since the molecule's geometry was controlled throughout the manipulation process, it was thereafter possible to re-deposit the molecule to the surface by re-approaching and applying a voltage pulse. Using this protocol, the word 'JÜLICH' was patterned into a PTCDA monolayer by removing molecules one by one. The correction of a mistake in the patterning was also demonstrated by lowering a molecule into a previously created vacancy. Currently work is underway to further the understanding of the key parameters involved in successful removal trajectories.

Next, the functionality of the single molecule device was exhibited in Chap. 3 with the development of SQDM. It was shown that the molecular QD was sufficiently electronically decoupled from the tip's electronic states that integer charge could be stabilized on it: the presence of resonant tunnelling features as well as sudden changes in the tip-sample force were the signals of single electron charging. The

effect of local electrostatic potential on the QD's charging features was illustrated with the help of a simple model. The validity of the approach, which modelled the QD as a single point charge, was proved by comparing the measured potential of a single, surface adsorbed PTCDA molecule to the result of a microelectrostatic simulation. This also resulted in an estimate of the position of the point charge: (7 ± 1) Å below the apex of the metal tip, precisely in the middle of the PTCDA QD. A quantitative measurement of the Smoluchowski dipole potential of a single adatom was then presented and shown to follow a z^{-2} power law as expected. The remarkable sensitivity of the method was demonstrated by its detection of the Smoluchowski potential $\sim$7 nm from its source.

The orthodox theory of the Coulomb blockade was applied to the single electron charging events integral to the SQDM method in Chap. 4. This consisted of modelling the system as a capacitor network, in conjunction with the constant interaction model, which states that the capacitances are independent of the QD electron occupation N. An expression for the bias drop in the junction based on experimental data was developed, however the theory was unable to fully explain the data. Subsequently the point charge model introduced in Chap. 3 was expanded upon. This model produced expressions based purely on experimental data for the energy level alignment and interelectronic Coulomb repulsion of the QD. The two models were then compared, revealing the full equivalence between them. The comparison helped to show that the models break down for the system presented here, after a non-negligible dependence on the electron population of the QD was revealed. Further studies will be necessary to determine if the predictions made in Chap. 4 are indeed true.

In Chap. 5 a robust and truly quantitative SQDM experiment was realized, where the structural properties of the tip were rendered essentially irrelevant. By considering the point charge model for a flat, extended nanostructure, it was shown that the remaining proportion of surface potential due to the screening effect of the tip was approximately equal to the voltage drop fraction α. This meant that the SQDM signal could be directly interpreted as a change in the surface potential and therefore a change in the work function of the surface. The change in the work function ϕ of Ag(111) after PTCDA adsorption was thus determined to be $\Delta\phi = (145 \pm 10)$ meV. To our knowledge this was the first work function study of the system including

real-space confirmation of the cleanliness of the surface, which clears up the existing disagreement in the literature surrounding the value of $\Delta\phi$. It was also a rare example of an SPM experiment where the mesoscopic tip structure plays almost no role in the measurement, while the active part of the tip has a very well-defined structure. Here it will be interesting to see what the surface structure size limit is for a $\Delta\phi$ value consistent with that of an extended structure. The focusing effect present in SQDM is however likely to reduce this limit, making the quantitative measurement of very small surface islands possible.

Bibliography

[1] G. E. Moore, *Electron. Mag.* **1965**, *38*.

[2] M. M. Waldrop, *Nature* **2016**, *530*, 144.

[3] S. Z. Butler et al., *ACS Nano* **2013**, *7*, 2898.

[4] X. Duan, C. Wang, A. Pan, R. Yu, X. Duan, *Chem. Soc. Rev.* **2015**, *44*, 8859.

[5] K. F. Wang, J.-M. Liu, Z. F. Ren, *Adv. Phys.* **2009**, *58*, 321.

[6] I. Žutić, J. Fabian, S. D. Sarma, *Rev. Mod. Phys.* **2004**, *76*, 323.

[7] M. Ratner, *Nat. Nanotechnol.* **2013**, *8*, 378.

[8] D. Xiang, X. Wang, C. Jia, T. Lee, X. Guo, *Chem. Rev.* **2016**, *116*, 4318.

[9] A. Aviram, M. A. Ratner, *Chem. Phys. Lett.* **1974**, *29*, 277.

[10] G. Binnig, H. Rohrer, C. Gerber, E. Weibel, *Phys. Rev. Lett.* **1982**, *49*, 57.

[11] C. Joachim, J. K. Gimzewski, R. R. Schlittler, C. Chavy, *Phys. Rev. Lett.* **1995**, *74*, 2102.

[12] M. A. Reed, C. Zhou, C. J. Muller, T. P. Burgin, J. M. Tour, *Science* **1997**, *278*, 252.

[13] H. Park, J. Park, A. K. L. Lim, E. H. Anderson, A. P. Alivisatos, P. L. McEuen, *Nature* **2000**, *407*, 57.

[14] S. Kubatkin, A. Danilov, M. Hjort, J. Cornil, J.-L. Brédas, N. Stuhr-Hansen, P. Hedegård, T. Bjørnholm, *Nature* **2003**, *425*, 698.

[15] H. Song, Y. Kim, Y. H. Jang, H. Jeong, M. A. Reed, T. Lee, *Nature* **2009**, *462*, 1039.

[16] R. M. Metzger et al., *J. Am. Chem. Soc.* **1997**, *119*, 10455.

[17] M. Elbing, R. Ochs, M. Koentopp, M. Fischer, C. von Hänisch, F. Weigend, F. Evers, H. B. Weber, M. Mayor, *Proc. Natl. Acad. Sci. U.S.A.* **2005**, *102*, 8815.

[18] C. Joachim, J. K. Gimzewski, *Chem. Phys. Lett.* **1997**, *265*, 353.

[19] A. S. Blum, J. G. Kushmerick, D. P. Long, C. H. Patterson, J. C. Yang, J. C. Henderson, Y. Yao, J. M. Tour, R. Shashidhar, B. R. Ratna, *Nat. Mater.* **2005**, *4*, 167.

[20] B.-Y. Choi, S.-J. Kahng, S. Kim, H. Kim, H. W. Kim, Y. J. Song, J. Ihm, Y. Kuk, *Phys. Rev. Lett.* **2006**, *96*, 156106.

[21] T. Miyamachi et al., *Nat. Commun.* **2012**, *3*, 936.

[22] T. Kudernac, N. Ruangsupapichat, M. Parschau, B. Maciá, N. Katsonis, S. R. Harutyunyan, K.-H. Ernst, B. L. Feringa, *Nature* **2011**, *479*, 208.

[23] N. A. Zimbovskaya, M. R. Pederson, *Phys. Rep.* **2011**, *509*, 1.

[24] P. H. Beton, A. W. Dunn, P. Moriarty, *Appl. Phys. Lett.* **1995**, *67*, 1075.

[25] L. Bartels, G. Meyer, K.-H. Rieder, *Appl. Phys. Lett.* **1997**, *71*, 213.

[26] D. V. Averin, K. K. Likharev in *Mesoscopic Phenomena in Solids*, *Vol. 30*, (Eds.: B. L. Altshuler, P. A. Lee, R. A. Webb), Elsevier, Amsterdam, **1991**, Chapter 6, pp. 173–271.

[27] J. Bardeen, *Phys. Rev. Lett.* **1961**, *6*, 57.

[28] J. Tersoff, D. R. Hamann, *Phys. Rev. B* **1985**, *31*, 805.

[29] C. J. Chen, *Phys. Rev. B* **1990**, *42*, 8841.

[30] V. M. Hallmark, S. Chiang, J. F. Rabolt, J. D. Swalen, R. J. Wilson, *Phys. Rev. Lett.* **1987**, *59*, 2879.

[31] J. Wintterlin, J. Wiechers, H. Brune, T. Gritsch, H. Höfer, R. J. Behm, *Phys. Rev. Lett.* **1989**, *62*, 59.

[32] G. Binnig, C. F. Quate, C. Gerber, *Phys. Rev. Lett.* **1986**, *56*, 930.

[33] H. Hamaker, *Physica* **1937**, *4*, 1058.

[34] F. J. Giessibl, *Rev. Mod. Phys.* **2003**, *75*, 949.

[35] Q. Zhong, D. Inniss, K. Kjoller, V. B. Elings, *Surf. Sci. Lett.* **1993**, *290*, L688.

[36] Y. Martin, C. C. Williams, H. K. Wickramasinghe, *J. Appl. Phys.* **1987**, *61*, 4723.

[37] T. R. Albrecht, P Grütter, D Horne, D Rugar, *J. Appl. Phys.* **1991**, *69*, 668.

[38] U. Dürig, O. Züger, A. Stalder, *J. Appl. Phys.* **1992**, *72*, 1778.

[39] F. J. Giessibl, *Science* **1995**, *267*, 68.

[40] K. Besocke, *Surf. Sci.* **1987**, *181*, 145.

[41] F. J. Giessibl, *Appl. Phys. Lett.* **2000**, *76*, 1470.

[42] F. J. Giessibl, *Appl. Phys. Lett.* **2001**, *78*, 123.

[43] L. Nony, A. Baratoff, D. Schär, O. Pfeiffer, A. Wetzel, E. Meyer, *Phys. Rev. B* **2006**, *74*, 235439.

[44] D. M. Eigler, E. K. Schweizer, *Nature* **1990**, *344*, 524.

[45] J. A. Stroscio, D. M. Eigler, *Science* **1991**, *254*, 1319.

[46] M. F. Crommie, C. P. Lutz, D. M. Eigler, *Science* **1993**, *262*, 218.

[47] A. J. Heinrich, C. P. Lutz, J. A. Gupta, D. M. Eigler, *Science* **2002**, *298*, 1381.

[48] Y. Sugimoto, M. Abe, S. Hirayama, N. Oyabu, Ó. Custance, S. Morita, *Nat. Mater.* **2005**, *4*, 156.

[49] K. K. Gomes, W. Mar, W. Ko, F. Guinea, H. C. Manoharan, *Nature* **2012**, *483*, 306.

[50] S. Kawai, A. S. Foster, F. F. Canova, H. Onodera, S.-I. Kitamura, E. Meyer, *Nat. Commun.* **2014**, *5*, 4403.

[51] F. E. Kalff, M. P. Rebergen, E. Fahrenfort, J. Girovsky, R. Toskovic, J. L. Lado, J. Fernández-Rossier, A. F. Otte, *Nat. Nanotechnol.* **2016**, 1.

[52] M. F. B. Green, T. Esat, C. Wagner, P. Leinen, A. Grötsch, F. S. Tautz, R. Temirov, *Beilstein J. Nanotechnol.* **2014**, *5*, 1926.

[53] R. Temirov, S. Soubatch, O. Neucheva, A. C. Lassise, F. S. Tautz, *New J. Phys.* **2008**, *10*, 053012.

[54] L. Gross, F. Mohn, N. Moll, P. Liljeroth, G. Meyer, *Science* **2009**, *325*, 1110.

[55] C. Weiss, C. Wagner, C. Kleimann, M. Rohlfing, F. S. Tautz, R. Temirov, *Phys. Rev. Lett.* **2010**, *105*, 086103.

[56] G. Kichin, C. Weiss, C. Wagner, F. S. Tautz, R. Temirov, *J. Am. Chem. Soc.* **2011**, *133*, 16847.

[57] F. Mohn, L. Gross, N. Moll, G. Meyer, *Nat. Nanotechnol.* **2012**, *7*, 227.

[58] L. Gross, B. Schuler, F. Mohn, N. Moll, N. Pavliček, W. Steurer, I. Scivetti, K. Kotsis, M. Persson, G. Meyer, *Phys. Rev. B* **2014**, *90*, 155455.

[59] N. Pavliček, B. Schuler, S. Collazos, N. Moll, D. Pérez, E. Guitián, G. Meyer, D. Peña, L. Gross, *Nat. Chem.* **2015**, *7*, 623.

[60] H. Mönig, D. R. Hermoso, O. Díaz Arado, M. Todorović, A. Timmer, S. Schüer, G. Langewisch, R. Pérez, H. Fuchs, *ACS Nano* **2015**, *10*, 1201.

[61] C. Wagner, R. Temirov, *Prog. Surf. Sci.* **2015**, *90*, 194.

[62] P. Hapala, G. Kichin, C. Wagner, F. S. Tautz, R. Temirov, P. Jelínek, *Phys. Rev. B* **2014**, *90*, 085421.

[63] P. Hapala, R. Temirov, F. S. Tautz, P. Jelínek, *Phys. Rev. Lett.* **2014**, *113*, 226101.

[64] S. K. Hämäläinen, N. van der Heijden, J. van der Lit, S. den Hartog, P. Liljeroth, I. Swart, *Phys. Rev. Lett.* **2014**, *113*, 186102.

[65] R. Wiesendanger, H.-J. Güntherodt, G. Güntherodt, R. J. Gambino, R. Ruf, *Phys. Rev. Lett.* **1990**, *65*, 247.

[66] C. Wagner, M. F. B. Green, P. Leinen, T. Deilmann, P. Krüger, M. Rohlfing, R. Temirov, F. S. Tautz, *Phys. Rev. Lett.* **2015**, *115*, 026101.

[67] M. F. B. Green, C. Wagner, P. Leinen, T. Deilmann, P. Krüger, M. Rohlfing, F. S. Tautz, R. Temirov, *Jpn. J. Appl. Phys.* **2016**, *55*, 08NA04.

[68] R. C. Ashoori, *Nature* **1996**, *379*, 413.

[69] S. M. Reimann, M. Manninen, *Rev. Mod. Phys.* **2002**, *74*, 1283.

[70] L. P. Kouwenhoven, D. G. Austing, S. Tarucha, *Rep. Prog. Phys.* **2001**, *64*, 701.

[71] J. Martínez-Blanco, C. Nacci, S. C. Erwin, K. Kanisawa, E. Locane, M. Thomas, F. von Oppen, P. W. Brouwer, S. Fölsch, *Nat. Phys.* **2015**, *11*, 640.

[72] W. Liang, M. P. Shores, M. Bockrath, J. R. Long, H. Park, *Nature* **2002**, *417*, 725.

[73] J. Park et al., *Nature* **2002**, *417*, 722.

[74] J. Repp, G. Meyer, F. E. Olsson, M. Persson, *Science* **2004**, *305*, 493.

[75] F. E. Olsson, S. Paavilainen, M. Persson, J. Repp, G. Meyer, *Phys. Rev. Lett.* **2007**, *98*, 176803.

[76] L. Gross, F. Mohn, P. Liljeroth, J. Repp, F. J. Giessibl, G. Meyer, *Science* **2009**, *324*, 1428.

[77] A. Bellec, L. Chaput, G. Dujardin, D. Riedel, L. Stauffer, P. Sonnet, *Phys. Rev. B* **2013**, *88*, 241406.

[78] M. T. Woodside, P. L. McEuen, *Science* **2002**, *296*, 1098.

[79] R. Stomp, Y. Miyahara, S. Schaer, Q. Sun, H. Guo, P. Grutter, S. Studenikin, P. Poole, A. Sachrajda, *Phys. Rev. Lett.* **2005**, *94*, 056802.

[80] L. Cockins, Y. Miyahara, S. D. Bennett, A. A. Clerk, S. Studenikin, P. Poole, A. Sachrajda, P. Grutter, *Proc. Natl. Acad. Sci. U.S.A.* **2010**, *107*, 9496.

[81] L. Cockins, Y. Miyahara, S. D. Bennett, A. A. Clerk, P. Grutter, *Nano Lett.* **2012**, *12*, 709.

[82] N. Kocić, P. Weiderer, S. Keller, S. Decurtins, S.-X. Liu, J. Repp, *Nano Lett.* **2015**, *15*, 4406.

[83] D. V. Averin, K. K. Likharev, *J. Low Temp. Phys.* **1986**, *62*, 345.

[84] C. W. J. Beenakker, *Phys. Rev. B* **1991**, *44*, 1646.

[85] P. L. McEuen, E. B. Foxman, U. Meirav, M. A. Kastner, Y. Meir, N. S. Wingreen, S. J. Wind, *Phys. Rev. Lett.* **1991**, *66*, 1926.

[86] *Single Charge Tunneling: Coulomb Blockade Phenomena in Nanostructures*, (Eds.: H. Grabert, M. H. Devoret), Plenum, New York, **1992**.

[87] *Nanoelectronics and Information Technology: Advanced Electronic Materials and Novel Devices*, (Ed.: R. Waser), Wiley, **2003**, Chapter 16.

[88] M. Brink, PhD thesis, Cornell University, **2007**.

[89] A. Tekiel, Y. Miyahara, J. M. Topple, P. Grutter, *ACS Nano* **2013**, *7*, 4683.

[90] S. Kitamura, K. Suzuki, M. Iwatsuki, *Appl. Surf. Sci.* **1999**, *140*, 265.

[91] M. Guggisberg, M. Bammerlin, C. Loppacher, O. Pfeiffer, A. Abdurixit, V. Barwich, R. Bennewitz, A. Baratoff, E. Meyer, H.-J. Güntherodt, *Phys. Rev. B* **2000**, *61*, 11151.

[92] C. Sommerhalter, T. Glatzel, T. W. Matthes, A. Jäger-Waldau, M. C. Lux-Steiner, *Appl. Surf. Sci.* **2000**, *157*, 263.

[93] U. Zerweck, C. Loppacher, T. Otto, S. Grafström, L. M. Eng, *Phys. Rev. B* **2005**, *71*, 125424.

[94] R. Baier, C. Leendertz, M. C. Lux-Steiner, S. Sadewasser, *Phys. Rev. B* **2012**, *85*, 165436.

[95] N. Sasaki, M. Tsukada, *Jpn. J. Appl. Phys.* **2000**, *39*, L1334.

[96] F. J. Giessibl, *Phys. Rev. B* **1997**, *56*, 16010.

[97] T. Ohgi, D. Fujita, *Phys. Rev. B* **2002**, *66*, 115410.

[98] A. Greuling, M. Rohlfing, R. Temirov, F. S. Tautz, F. B. Anders, *Phys. Rev. B* **2011**, *84*, 125413.

[99] A Greuling, R Temirov, B Lechtenberg, F. B. Anders, M Rohlfing, F. S. Tautz, *Phys. Status Solidi* **2013**, *250*, 2386.

[100] T. Esat, T. Deilmann, B. Lechtenberg, C. Wagner, P. Krüger, R. Temirov, F. B. Anders, M. Rohlfing, F. S. Tautz, P. Gr, *Phys. Rev. B* **2015**, *91*, 144415.

[101] T. Esat, B. Lechtenberg, T. Deilmann, C. Wagner, P. Krüger, R. Temirov, M. Rohlfing, F. B. Anders, F. S. Tautz, *Nat. Phys.* **2016**, *12*, 867.

[102] M. Macucci, K. Hess, G. J. Iafrate, *Phys. Rev. B* **1993**, *48*, 17354.

[103] G. J. Iafrate, K. Hess, J. B. Krieger, M. Macucci, *Phys. Rev. B* **1995**, *52*, 10737.

[104] J. R. Sabin, S. B. Trickey, S. P. Apell, J. Oddershede, *Int. J. Quantum Chem.* **2000**, *77*, 358.

[105] T. P. LaFave Jr., PhD thesis, Southern Methodist University, **2006**.

[106] R Temirov, A Lassise, F. B. Anders, F. S. Tautz, *Nanotechnology* **2008**, *19*, 065401.

[107] C. Toher, R. Temirov, A. Greuling, F. Pump, M. Kaczmarski, G. Cuniberti, M. Rohlfing, F. S. Tautz, *Phys. Rev. B* **2011**, *83*, 155402.

[108] T. Koopmans, *Physica* **1934**, *1*, 104.

[109] M Stopa, N Heretofore, **1993**, *48*, 340.

[110] H. W. C. Postma, Z. Yao, C. Dekker, *J. Low Temp. Phys.* **2000**, *118*, 495.

[111] J. K. Norsko, *Rep. Prog. Phys.* **1990**, *53*, 1253.

[112] D. V. Averin, A. N. Korotkov, K. K. Likharev, *Phys. Rev. B* **1991**, *44*, 6199.

[113] J. Zhu, M. Brink, P. L. McEuen, *Appl. Phys. Lett.* **2005**, *87*, 242102.

[114] M. Ondráček, P. Hapala, P. Jelínek, *Nanotechnology* **2016**, *27*, 274005.

[115] A. Einstein, *Ann. Phys.* **1905**, *322*, 132.

[116] M. Planck, *Ann. Phys.* **1900**, *306*, 719.

[117] P. Lenard, *Ann. Phys.* **1902**, *313*, 149.

[118] C. G. Vayenas, S. Bebelis, S. Ladas, *Nature* **1990**, *343*, 625.

[119] M. T. Greiner, M. G. Helander, W.-M. Tang, Z.-B. Wang, J. Qiu, Z.-H. Lu, *Nat. Mater.* **2012**, *11*, 76.

[120] R. H. Friend et al., *Nature* **1999**, *397*, 121.

[121] H. E. Farnsworth, R. P. Winch, *Phys. Rev.* **1940**, *58*, 812.

[122] M. Chelvayohan, C. H. B. Mee, *J. Phys. C: Solid State Phys.* **1982**, *15*, 2305.

[123] P. C. Rusu, G. Giovannetti, C. Weijtens, R. Coehoorn, G. Brocks, *Phys. Rev. B* **2010**, *81*, 125403.

[124] M. Nonnenmacher, M. P. O'Boyle, H. K. Wickramasinghe, *Appl. Phys. Lett.* **1991**, *58*, 2921.

[125] F. Krok, K. Sajewicz, J. Konior, M. Goryl, P. Piatkowski, M. Szymonski, *Phys. Rev. B* **2008**, *77*, 235427.

[126] J. Colchero, A. Gil, A. M. Baró, *Phys. Rev. B* **2001**, *64*, 245403.

[127] T. Hochwitz, A. K. Henning, C. Levey, C. Daghlian, J. Slinkman, *J. Vac. Sci. Technol. B* **1996**, *14*, 457.

[128] K. Wandelt in *Thin Metal Films and Gas Chemisorption*, *Vol. 32*, (Ed.: P. Wissmann), Elsevier, **1987**, Chapter 7, pp. 280–368.

[129] T. Jung, Y. W. Mo, F. J. Himpsel, *Phys. Rev. Lett.* **1995**, *74*, 1641.

[130] E. D. L. Rienks, N. Nilius, H.-P. Rust, H.-J. Freund, *Phys. Rev. B* **2005**, *71*, 241404.

[131] H. C. Ploigt, C. Brun, M. Pivetta, F. Patthey, W. D. Schneider, *Phys. Rev. B* **2007**, *76*, 195404.

[132] C. R. Henry, *Surf. Sci. Rep.* **1998**, *31*, 231.

[133] M. Bäumer, H.-J. Freund, *Prog. Surf. Sci.* **1999**, *61*, 127.

[134] B. H. Ishii, K. Sugiyama, E. Ito, K. Seki, *Adv. Mater.* **1999**, *11*, 605.

[135] D. V. Talapin, J.-S. Lee, M. V. Kovalenko, E. V. Shevchenko, *Chem. Rev.* **2010**, *110*, 389.

[136] Y. Zhou et al., *Science* **2012**, *336*, 327.

[137] M. Rohlfing, R. Temirov, F. S. Tautz, *Phys. Rev. B* **2007**, *76*, 115421.

[138] F. S. Tautz, *Prog. Surf. Sci.* **2007**, *82*, 479.

[139] S. Duhm, A. Gerlach, I. Salzmann, B. Bröker, R. L. Johnson, F. Schreiber, N. Koch, *Org. Electron.* **2008**, *9*, 111.

[140] E. Kawabe, H. Yamane, R. Sumii, K. Koizumi, Y. Ouchi, K. Seki, K. Kanai, *Org. Electron.* **2008**, *9*, 783.

[141] Y. Zou, L. Kilian, A. Schöll, T. Schmidt, R. Fink, E. Umbach, *Surf. Sci.* **2006**, *600*, 1240.

[142] A. Hauschild, K. Karki, B. C. C. Cowie, M. Rohlfing, F. S. Tautz, M. Sokolowski, *Phys. Rev. Lett.* **2005**, *94*, 036106.

List of Figures

Band / Volume 167
Management of Electrophysiological Data & Metadata
Making complex experiments accessible to yourself and others
L. Zehl (2018), 182 pp
ISBN: 978-3-95806-311-2

Band / Volume 168
Investigation of GeSn as Novel Group IV Semiconductor for Electronic Applications
C. Schulte-Braucks, Christian (2018), xx, 165, XII pp
ISBN: 978-3-95806-312-9

Band / Volume 169
Tailoring the Electronic Properties of Epitaxial Oxide Films via Strain for SAW and Neuromorphic Applications
Y. Dai (2018), VI, 133 pp
ISBN: 978-3-95806-319-8

Band / Volume 170
The electronic structure of transition metal dichalcogenides investigated by angle-resolved photoemission spectroscopy
M. Gehlmann (2018), ii, 108, XVIII pp
ISBN: 978-3-95806-324-2

Band / Volume 171
Control of neuron adhesion by metal nanoparticles
A. Q. Tran (2018), viii, 108 pp
ISBN: 978-3-95806-332-7

Band / Volume 172
Neutron Scattering
Lectures of the JCNS Laboratory Course held at Forschungszentrum Jülich and at the Heinz-Maier-Leibnitz Zentrum Garching
edited by T. Brückel, S. Förster, G. Roth, and R. Zorn (Eds.) (2018), ca 300 pp
ISBN: 978-3-95806-334-1

Band / Volume 173
Spin scattering of topologically protected electrons at defects
P. Rüßmann (2018), vii, 230 pp
ISBN: 978-3-95806-336-5

Band / Volume 174
Interfacing EuO in confined oxide and metal heterostructures
P. Lömker (2018), vi, 140 pp
ISBN: 978-3-95806-337-2

Band / Volume 175
Operando Chemistry and Electronic Structure of Electrode / Ferroelectric Interfaces
S. Gonzalez (2018), 159 pp
ISBN: 978-3-95806-341-9

Band / Volume 176
Magnetic Properties of Self-assembled Manganese Oxide and Iron Oxide Nanoparticles
Spin Structure and Composition
X. Sun (2018), ii, 178 pp
ISBN: 978-3-95806-345-7

Band / Volume 177
Model-based reconstruction of magnetisation distributions in nanostructures from electron optical phase images
J. Caron (2018), XXI, 183 pp
ISBN: 978-3-95806-346-4

Band / Volume 178
Simultaneous dual-color imaging on single-molecule level on a Widefield microscope and applications
R. Ledesch (2018), ix, 119 pp
ISBN: 978-3-95806-348-8

Band / Volume 179
Methoden der Leitfähigkeitsuntersuchung mittels Rasterkraftmikroskop und deren Anwendung auf Barium Titanat Systeme
B. Reichenberg (2018), x, 144 pp
ISBN: 978-3-95806-350-1

Band / Volume 180
Manipulation of magnetism in iron oxide nanoparticle / $BaTiO_3$ composites and low-dimensional iron oxide nanoparticle arrays
L. Wang (2018), VI, 151 pp
ISBN: 978-3-95806-351-8

Band / Volume 181
Creating and characterizing a single molecule device for quantitative surface science
M. Green (2018), viii, 142 pp (untersch. Pag.)
ISBN: 978-3-95806-352-5

Weitere ***Schriften des Verlags im Forschungszentrum Jülich*** unter
http://wwwzb1.fz-juelich.de/verlagextern1/index.asp

Schlüsseltechnologien / Key Technologies
Band / Volume 181
ISBN 978-3-95806-352-5

Mitglied der Helmholtz-Gemeinschaft

JÜLICH
Forschungszentrum